Modern Approaches to the Development of Energetic Materials

by

Rosalyn V. Kent

A dissertation submitted in partial fulfillment
of the requirements for the degree of
Doctor of Philosophy
(Chemistry)
in the University of Michigan
2019

Doctoral Committee:

Professor Adam J. Matzger, Chair
Professor André L. Boehman
Professor Anne J. McNeil
Professor Pavel Nagorny

Rosalyn V. Kent

rvkent@umich.edu

ORCID iD: 0000-0002-2312-3527

Dedication

To the Kent, Nevills, and Young Family

To Charles

Acknowledgements

First, I thank God for the privilege to pursue graduate education, and for perseverance and motivation to push my research forward each day. I thank my parents, Pamela Kent and Larry Kent, for all of their love and encouragement. I also thank my sister, Gracie Kent, for always making me laugh and encouraging me to strive for greatness. I am very thankful for the unending support and love from my extended family, especially my grandfather Willie B. Nevills and favorite Auntie Gracie. I thank my amazing my fiancé, Charles Fobbs, for always loving me, encouraging me and for being a great life partner! I give a special thank you to my best friends Elizabeth Wallis, Kyle McDonald, and Kendra Souther for their genuine friendship and support. I thank my awesome research advisor Professor Adam J. Matzger for his guidance, genuine support, and patience throughout my graduate career. I also thank my dissertation committee for their time and thoughtful advice. I thank Dr. Antek Wong-Foy for his knowledgeable advice, hilarious conversations and diligent efforts to maintain critical instrumentation. I thank all of my colleagues in the Matzger lab both past and present for their advice, support and well-wishes. I am very thankful for the opportunity to work with Dr. Jon Bennion, whose mentorship and helpful discussions around energetic materials were greatly appreciated. I thank Ren Wiscons for being a great desk-mate and for all of her thoughtful advice on crystal structures and crystal engineering. I give a special thank you to Dr. Jake Boissonnault for his valuable advice around metal-organic framework synthesis. Finally, “Thank you!” to Dr. Austin C. Kizzie, whose dissertation was especially helpful in assembling my own!

Table of Contents

List of Figures

List of Tables

Abstract

Energetic materials (EMs) are compounds and compositions that respond rapidly to stimuli by releasing large amounts of gases and energy. These materials are typically central to a variety of commercial and military applications. However, some traditional and widely used energetic materials have toxic decomposition products and can be dangerous to handle due to impact sensitivity issues. One of the major goals for the energetics field is to develop more eco-friendly (non-polluting or readily degradable in the environment) materials that exhibit performance comparable to widely used energetic materials. An emerging class of energetics based on high-nitrogen materials promise to avoid the issues of traditional EMs.

Some of the key properties of energetic materials include: oxygen balance, decomposition temperature, detonation velocity and detonation pressure. The stringent requirements for cost, manufacturability and performance are constraints such that new chemical entities are rarely introduced to the market. Here, crystal engineering strategies are employed to design new materials with desired physical and chemical properties. Crystal engineering is unique in being able to leverage existing manufacturing infrastructure for energetic materials. However, one must first uncover the fundamental rules of how energetic molecules interact to develop a design strategy.

The work presented in this dissertation focuses on the advancement of modern strategies used to develop new energetic materials through supramolecular synthesis. Through the design of new energetic compounds and compositions, this investigation aims to improve undesired

properties of existing energetic materials like toxic decomposition products and oxygen deficiency. Chapter 2 covers work that examines methods of cocrystal engineering with a high-nitrogen energetic material known as BTATz. Cocrystals are not known for many energetic materials and within the class of high-nitrogen molecules the quantity is even more limited. This is because the types of coformers suitable for cocrystallization with high-nitrogen energetics have not yet been elucidated. In this chapter, it is shown that high-nitrogen energetics can in fact form cocrystals and classes of molecules capable of interrupting strong intermolecular interactions are identified. In addition, theoretical energetic performance calculations are discussed. Synthesis of energetic coordination polymers represents a straightforward development approach wherein energetic ligands are coordinated to non-toxic metal ions to produce new metal-organic species. In Chapter 3, an effort towards generating multi-dimensional energetic coordination polymers with the high-nitrogen ligand, BTATz, is detailed. This approach is discussed as an effective means to synthesize energetic coordination polymers that directly incorporate high-nitrogen energetic materials as ligands. The pores of non-energetic metal-organic frameworks can be accessed for the adsorption of over oxidized guests to yield energetic compositions with adjustable oxygen content and modulated properties. In Chapter 4, the development MOF-oxidant composites utilizing zeolitic imidazolate frameworks (ZIFs) as porous hosts are presented. ZIFs are robust and thermally stable structures and two frameworks, ZIF-8 and ZIF-70 were used to absorb volatile tetranitromethane guests. The resultant ZIF-TNM composites exhibit high-energy release and more neutral oxygen balances relative to the porous frameworks. Finally, Chapter 5 will offer a summary on future directions that could be pursued in the development of new high-nitrogen energetic materials.

Chapter One

Introduction

The work described in this thesis will detail modern approaches to the development of new energetic materials through supramolecular synthesis. This introductory chapter provides general background on energetic materials and discussion of two relatively new strategies for producing novel energetic materials: cocrystallization and synthesis of energetic coordination polymers.

1.1 Energetic Materials

Energetic materials (EMs) are a class of compounds and compositions that respond to initiation by thermal, impact or electrostatic stimuli by exhibiting a rapid exothermic transition. EMs typically contain fuel and oxidizer, and do not require atmospheric oxygen to sustain the exothermic reaction. Upon decomposition EMs rapidly release large quantities of gaseous products, heat and pressure.[1] There are three classes of energetic materials: pyrotechnics, propellants and explosives.[2] Pyrotechnics are energetic mixtures that contain reducing agents (i.e. metal powders) and oxidizers (i.e. nitrates or perchlorates) in a composition rather than on the chemical structure of one molecule. The energy released by the non-detonative exothermic transition of pyrotechnics is accompanied by light, sound, gas, smoke, or a combination of these effects. Typically, pyrotechnic reactions proceed more slowly than explosive detonations and produce larger quantities of solid residue than gaseous products.[3-4] Propellants are energetic materials that violently burn and do not explode. After initiation, propellants transition from solid to large volumes of gaseous products in millisecond or longer timeframes and exhibit a spark or flash. One of the earliest examples of a propellant is blackpowder (i.e. gunpowder) which is a composition of potassium nitrate (KNO_3), sulfur and charcoal.[1,3] Explosives are compounds that exhibit an extremely rapid transition known as a detonation wherein an

exothermic reaction proceeds at velocities greater than the local speed of sound to produce a detonation wave. Explosives are highly reactive compounds that respond to various stimuli by releasing large quantities of gas and pressure that causes considerable damage to surroundings.[1, 3] Explosives are further divided into two classes, primary and secondary explosives, based on the material sensitivity to stimuli. Primary explosives tend to exhibit high sensitivity to stimuli and can be initiated via a small stimulus, whereas secondary explosives are less sensitive to impact and are more powerful than a primary explosive.[5] Typically, primary explosives are used to initiate secondary explosives thorough propagation of a shockwave from the primary through the material.[6] Two examples of traditional primary and secondary explosives are lead styphnate and 2,4,6-trinitrotolue (TNT), respectively as shown in Figure 1.1.

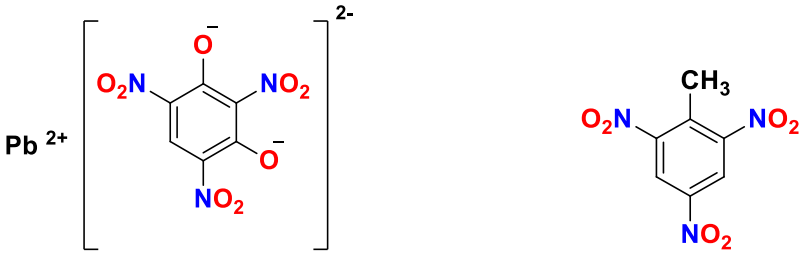

Figure 1.1 Chemical structures of primary explosive lead styphnate and secondary explosive 2,4,6-trinitrotoluene (TNT).

Traditional explosive materials are used in small arms ammunition for military and commercial applications such as mining, construction and demolition.[7] However, TNT and lead styphnate produce toxic decomposition products which constitute a health and safety problem for personnel. For example, detonating explosives like TNT leads to the formation of carbon monoxide, a toxic odorless gas that can migrate through the ground and collect in nearby basements and other confined spaces at toxic levels.[56] Since carbon monoxide is an odorless gas there is no indication that a hazard exists. Furthermore, firing bullets containing lead styphnate can generate considerable lead contamination on military training grounds and firing ranges. In

2012, the US geological survey calculated that 60,100 metric tons of lead was used in ammunition and bullets in the United States alone.[5, 8] Lead is not only used as a primer in bullets, but also within the bullet core material. Firing bullets in shooting ranges is not only a recreational activity for the public but this is also a required for training law enforcement and military personnel. When a bullet is fired the material disintegrates at high pressure releasing lead particles, dust and gas onto the shooter. Exposure to lead can cause adverse health effects like decreased kidney function, hypertension, and cardiovascular issues.[5, 8] One solution to the problem of toxic decomposition products including carbon monoxide and lead is the design energetic materials that are free of heavy metals and consists of sufficient oxygen content.

1.2 High-Nitrogen Energetic Materials

An ongoing focus in the energetics field is the development of new materials that release environmentally benign decomposition products. One common approach to design new energetic materials is to install numerous energetic nitro groups onto a carbon skeleton. A nitro substituent provides the oxygen needed to oxidize carbon and hydrogen fuel during reaction of the energetic materials.[9] In addition, the energy generated by decomposition of nitrated energetics is derived solely from combustion of the fuel because these molecules typically have heats of formation near zero.[10] Many nitrated energetics are also oxygen deficient which means that there is usually not enough oxygen present on the molecule to fully oxidize all of the fuel to neutral molecular products. As a result, the decomposition of nitrated energetic materials generates soot, residue and smoke. [11]

Compounds that contain a significant amount of nitrogen, also known as high nitrogen compounds, are attractive candidates to replace traditional energetic materials synthesized with a carbon backbone. This is because high-nitrogen energetic materials avoid toxic decomposition

products since mostly N_2 gas is generated upon decomposition.[11] In addition, high nitrogen compounds contain inherently energetic N-N, N=N and C-N bonds and the energy released during decomposition relies solely on high heats of formation, which is an intrinsic property of high-nitrogen compounds.[12,13] This is in contrast to the energy released as a result of the often-incomplete combustion of a carbon backbone in nitrated energetic materials. High-nitrogen energetic materials are typically insensitive to initiation by various stimuli as they tend to exhibit high thermal decomposition temperatures and are insensitive to impact. Often the performance and sensitivity of nitrated secondary energetic materials are directly proportional, wherein materials that exhibit high performance are typically more sensitive to stimuli.[11, 14] High-nitrogen energetic materials seemingly contradict this correlation as these materials tend to be high performing and insensitive to initiation by various stimuli.[14]

1.3 Cocrystallization

Covalent synthesis of new materials is the traditional method used to achieve desired properties in energetic molecules. However, due to the stringent requirements for fielding a new energetic material, new entities are rarely brought to the market. Cocrystallization is one alternative strategy that can be employed to design a new energetic material with desired solid-state properties.[15-19] Cocrystallization is the synthesis of two neutral components in a single crystalline lattice and defined stoichiometric ratio as illustrated in figure 1.2.[20, 21]

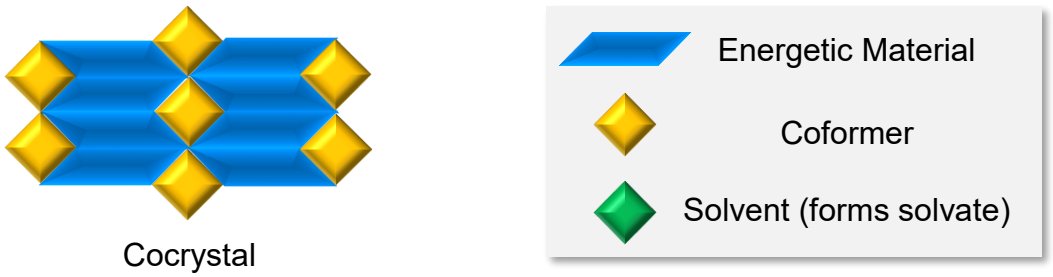

Figure 1.2 Diagram of an energetic cocrystal with example components: energetic material, coformer and solvent.

The formation of a cocrystal relies on non-covalent interactions between the two components. These non-covalent interactions include hydrogen bonds and complementary π–π stacking.[22-24] Cocrystallization is a strategy that leverages existing materials and achieves the modulation of properties through new interactions between coformers. Cocrystallization has been previously utilized in the pharmaceutical industry to improve physicochemical properties of active pharmaceutical ingredients (APIs). The physicochemical properties that can be influenced by cocrystallization include the bioavailability and stability of an API.[25] One example of this strategy was demonstrated with a diabetes drug candidate known as ertugliflozin. This API promotes the excretion of glucose through urine as a mechanism to treat Type 2 diabetes. Previously, ertugliflozin did not exist in a stable crystal form; however, through cocrystallization with pyroglutamic acid the stability of the API was improved allowing further development.

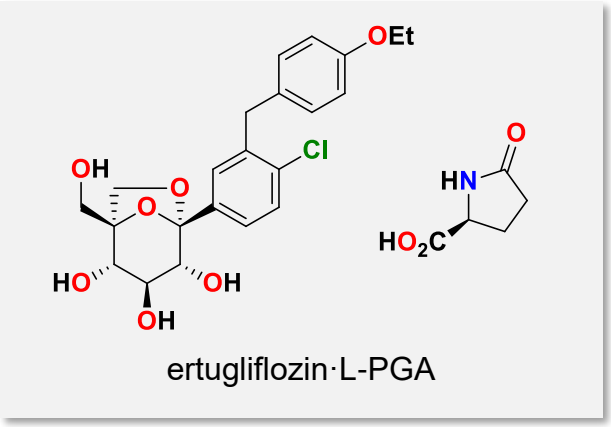

Figure 1.3 Cocrystallization was employed to improve physicochemical properties of ertugliflozin. Ertugliflozin pyroglutamic acid (L-PGA) is a pharmaceutical cocrystal in late stage clinical development.[26]

Currently, the ertugliflozin-pyroglutamic acid cocrystal is in late stage clinical trials.[26] Cocrystallization favors robust hydrogen bond donating and accepting groups, and active pharmaceutical ingredients like ertugliflozin often possess these functionalities on the chemical structure. Energetic materials, on the other hand, lack these types of reliable synthons and as a result cocrystals are not known for many energetic materials and even for those that can form cocrystals, the types of coformers suitable for cocrystallization must be developed through a design strategy. One design approach that can predict the complementarity of two coformers in a cocrystal is a calculation of the theoretical electrostatic potential of each molecule.[18, 27] Electrostatic potential is mapped onto an isodensity surface of a molecule which depicts overall size and charge distribution with respect to regions of negative (red), neutral (green) and positive (blue) potential. [28]

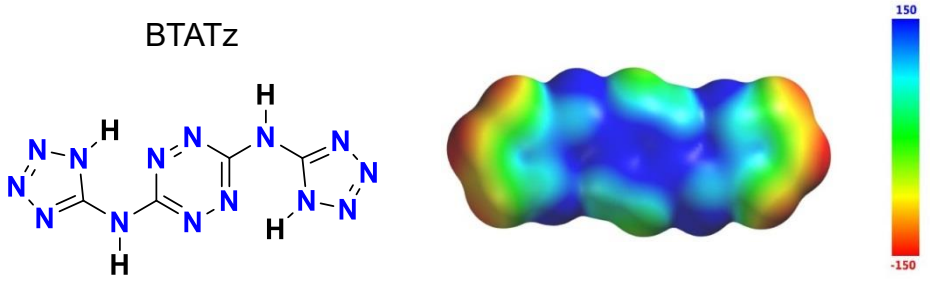

Figure 1.4 Chemical structure and electrostatic potential surface of a high nitrogen energetic material, BTATz, which were calculated using density functional method B3LYP/6-31+G**.

This design approach was demonstrated in a study by Landenberger et. al. wherein a benchmark energetic material 2,4,6-trinitrotoluene, TNT, was cocrystallized with 17 non-energetic coformers.[29] The electrostatic potential map of TNT exhibits a significant region of positive electrostatic potential because the polar nitro substituents on TNT withdraw electron density from the aromatic ring onto the electronegative oxygen atoms. Overall this map reveals that TNT has an electron poor aromatic ring and therefore suitable coformers would ideally have substantial negative electrostatic potential within the core of an aromatic π system to complement the positive potential of TNT. Some successful coformers with TNT include naphthalene, anthracene, and tetrathiafulvalene, all containing electron rich π systems. The primary stabilizing forces in the TNT cocrystals were complementary π–π interactions revealing that this design strategy was successful in probing coformer compatibility and can be further applied to other classes of energetic materials.

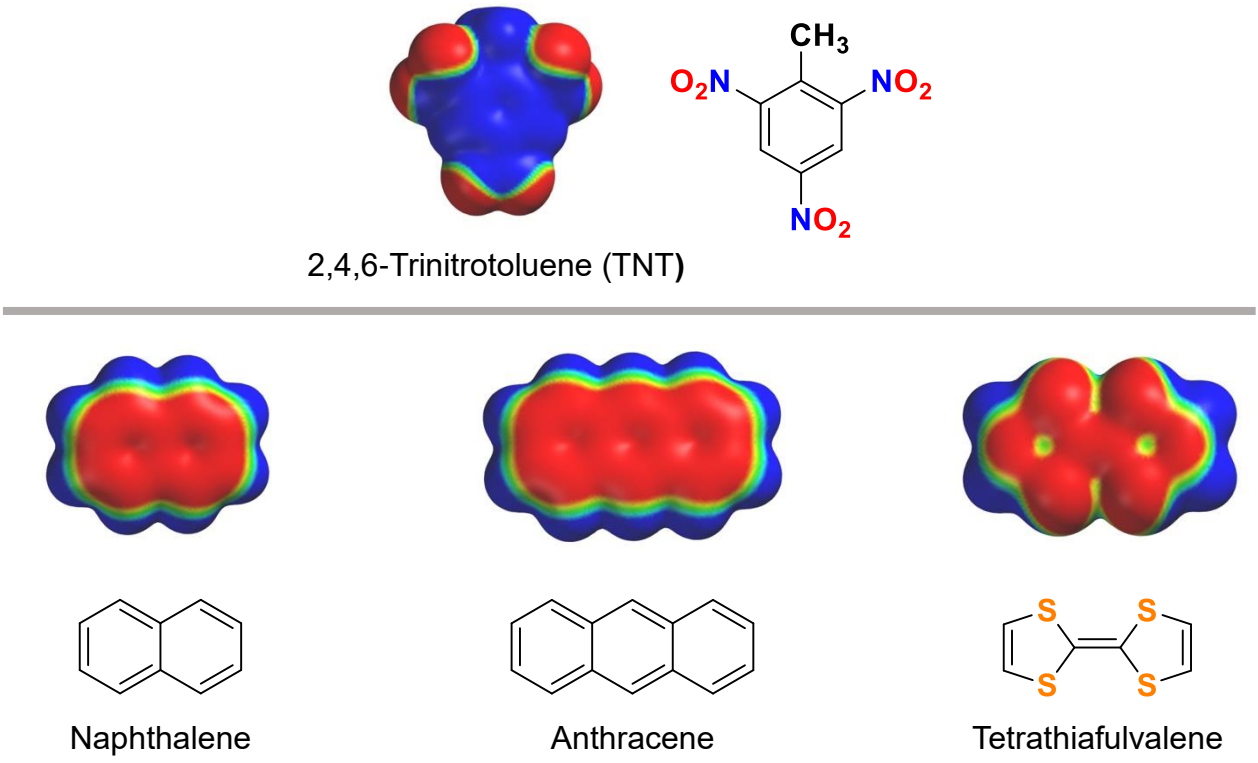

Figure 1.5 Chemical structures and electrostatic potential surface of TNT and successful coformers, naphthalene, anthracene and tetrathiafulvalene which were calculated using density functional method B3LYP/6-31+G**.

1.4 Energetic Coordination Polymers

Coordination polymers (CPs) are 1D, 2D or 3D frameworks constructed from the self-assembly of metal ions bridging ligands in a periodic assembly to form an ordered crystalline material.[30] Traditionally CPs, specifically the subclass known as microporous coordination polymers, target applications requiring porosity such as gas storage, separations and catalysis.[31-34] Recently, several research groups have investigated the potential of CPs as energetic materials. The synthesis of CPs is a useful design tool for new energetic materials because this strategy can leverage existing explosives as organic ligand avoiding covalent modification. This approach provides a strategy to construct multi-dimensional frameworks using well-studied, scalable

energetic materials, to improve properties like density, oxygen balance, and stability. The resulting energetic CPs are tailored, high-energy materials with desirable properties.[35-37]

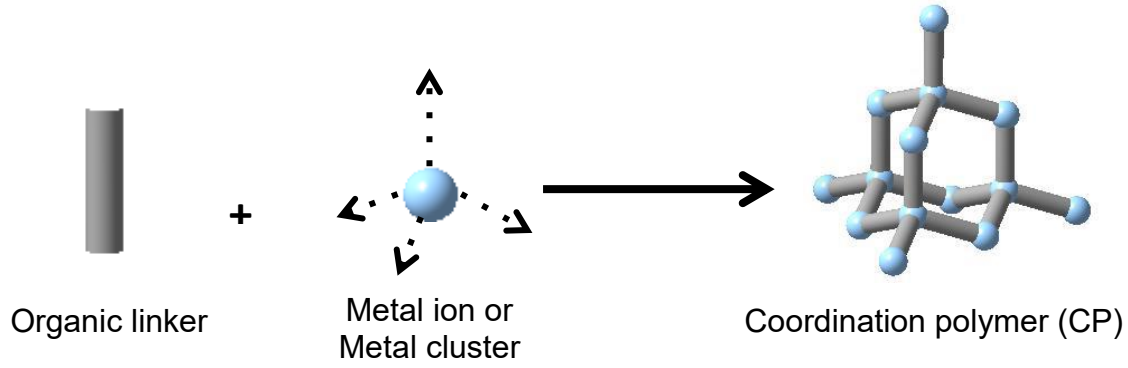

Figure 1.6 General scheme of coordination polymer synthesis.

There are limited examples in the literature that directly incorporate energetic materials as ligands in CPs. Historically, CPs are assembled with organic ligands containing carboxylate functionality; however, these kinds of ligands are inadequate for energetic applications because minimal heat is released as result of complete oxidation of the carbonyl carbon.[36] In contrast, construction of CPs with nitrogen rich heterocyclic compounds is an attractive strategy to produce energetic frameworks with intrinsically favorable properties. Nitrogen rich heterocycles are favored ligands due to their variety of coordination modes and inherently energetic N-N and N=N bonds.[38] Recently, development of energetic CPs has proven successful with triazoles and tetrazoles.[39-43] For example, Pang and coworkers recently developed energetic coordination polymers using the nitrogen rich heterocyclic linker 4,4'-azo-1,2,4-triazole (ATRZ) in the presence of Ag and Cu salts. The ATRZ linker has 6 potential coordination sites which can promote the formation of 3D coordination polymers.[44]

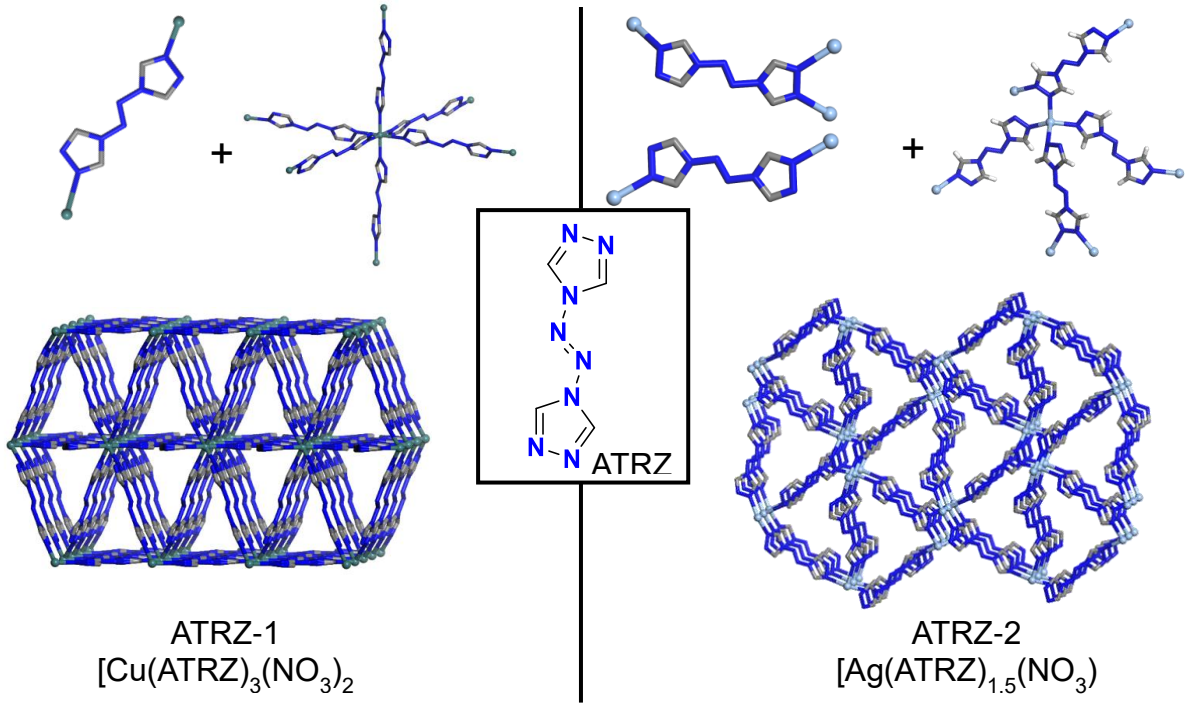

Figure 1.7 Nitrogen rich heterocyclic linker 4,4'-azo-1,2,4-triazole (ATRZ) has six potential coordination sites which can lead to a variety of 3D coordination modes. In the presence of Cu the linker acts as a 2-connecting module with Cu (II) and produces the 3D CP ATRZ-1, however in the presence of Ag the linker acts as a 2- and 3- connecting units and produces the 3D CP ATRZ-2.

The following coordination polymers were isolated and characterized: $[Cu(ATRZ)_3(NO_3)_2]_n$ (ATRZ-1) and $[Ag(ATRZ)_{1.5}(NO_3)]_n$ (ATRZ-2). In the presence of Cu, ATRZ exhibits linear bidentate coordination and ATRZ-1 assembles as a doubly interpenetrated network. However, in the presence of Ag, ATRZ-2 is produced and exhibits a mixture of coordination modes, 2- and 3-connectivity within the same framework. At room temperature ATRZ has a crystallographic density of 1.61 g/cm^3. ATRZ-1 exhibits a crystal density of 1.68 g/cm^3 and ARTZ-2 exhibits a much higher crystal density of 2.16 g/cm^3. This example shows that as a result of metal-organic coordination, the density of an energetic material can be significantly improved by replacing weak intermolecular interactions with shorter coordination bonds. Other advantages of high-

nitrogen energetic CPs include: low impact sensitivity and promising detonation performance.[45, 46]

1.5 MOF-Oxidant Composites

A class of coordination polymers known as metal-organic frameworks (MOFs) are robust structures prepared by the coordination of metal ions to bridging organic ligands, to form exclusively 2-D and 3-D ordered, crystalline materials.[30] MOFs typically exhibit permanent porosity, high thermal stability and structural stability which leads to a variety of applications.[31, 32, 47-52] MOFs contain a significant amount of carbon, hydrogen and nitrogen which can be utilized as fuel for energetic purposed. This fuel can be intimately mixed with over-oxidized guests to form explosive compositions. A recent study showed that a non-energetic fuel rich framework known as MOF-5, which is composed of terephthalate ligands coordinated to tetrahedral Zn ions can be loaded with energetic oxidizers (hexanitroethane and tetranitromethane) to form highly explosive materials that exhibit high sensitivity to impact. The compositions MOF-5-TNM and MOF-5-HNE were classified as primary explosives because each composition could be initiated via a small stimulus.[53] Unfortunately, the MOF-5 framework is composed of carboxylate functionalized ligands, so the overall heat release of the compositions could be improved. One solution to this problem is nitrogen-metal coordination.

1.6 Sensitivity Measurements

The parameters of importance for designing a new energetic material include sensitivity to stimuli, toxicity of decomposition products, performance in comparison to known materials and overall cost. Sensitivity tests are typically performed to determine safe handling procedures for personnel and transport of the energetic material.[37, 54, 55] These tests examine how the material responds to stimuli including thermal and impact stimuli. Thermal sensitivity measurements are

performed using differential scanning calorimetry (DSC) and thermogravimetric calorimetry to determine the thermal sensitivity under a given set of conditions. Impact sensitivity testing on the other hand is used to determine the probability of explosion for propellant and explosive materials. The most simple impact sensitivity test is a drop weight impact test which can be performed with an in-house apparatus on small quantities of sample.[18] Generally, the drop weight impact test is used to determine the drop height at which explosive and propellant samples react with a 50% probability. A successful explosion is one that produces with a spark/flash and or a loud sound.

1.7 References:

1. M. Klapötke Thomas, *Chemistry of High-Energy Materials*, 2015.
2. A. K. Sikder and N. Sikder, *Journal of Hazardous Materials*, 2004, **112**, 1-15.
3. J. Akhavan and C. Royal Society of, *The chemistry of explosives / Jacqueline Akhavan*, Royal Society of Chemistry, 2004.
4. G. Steinhauser and T. M. Klapötke, *Angewandte Chemie International Edition*, 2008, **47**, 3330-3347.
5. M. H. V. Huynh, M. A. Hiskey, T. J. Meyer and M. Wetzler, *Proceedings of the National Academy of Sciences*, 2006, **103**, 5409-5412.
6. T. M. Klapötke and N. Mehta, *Propellants, Explosives, Pyrotechnics*, 2014, **39**, 7-8.
7. M. Brinsden, A. Boock and D. Baum, *Propellants, Explosives, Pyrotechnics*, 2015, **40**, 453-454.
8. M. A. S. Laidlaw, G. Filippelli, H. Mielke, B. Gulson and A. S. Ball, *Environmental Health*, 2017, **16**, 34.
9. D. Chavez, M. Hiskey, M. H. Huynh, D. L. Naud, S. Son and B. C. Tappan, *The combustion properties of novel high-nitrogen energetic materials*, 2006.
10. M. A. Hiskey, N. Goldman and J. R. Stine, *Journal of Energetic Materials*, 1998, **16**, 119-127.

11. A. Saikia, R. Sivabalan, B. G. Polke, G. M. Gore, A. Singh, A. Subhananda Rao and A. K. Sikder, *Journal of Hazardous Materials*, 2009, **170**, 306-313.
12. D. E. Chavez and M. A. Hiskey, *Journal of Energetic Materials*, 1999, **17**, 357-377.
13. D. Chavez, M. Hiskey and D. L. Naud, *Tetrazine Explosives*, 2004.
14. M. A. C. Hiskey, D.E.; Naud, D.L. , *Insensitive High-Nitrogen Compounds* LA-UR-01-1493, Los Alamos National Laboratory, 2001.
15. J. C. Bennion, N. Chowdhury, J. W. Kampf and A. J. Matzger, *Angewandte Chemie International Edition*, 2016, **55**, 13118-13121.
16. J. C. Bennion, A. McBain, S. F. Son and A. J. Matzger, *Crystal Growth & Design*, 2015, **15**, 2545-2549.
17. O. Bolton, L. R. Simke, P. F. Pagoria and A. J. Matzger, *Crystal Growth & Design*, 2012, **12**, 4311-4314.
18. K. B. Landenberger, O. Bolton and A. J. Matzger, *Journal of the American Chemical Society*, 2015, **137**, 5074-5079.
19. K. B. Landenberger and A. J. Matzger, *Crystal Growth & Design*, 2012, **12**, 3603-3609.
20. A. D. Bond, *CrystEngComm*, 2007, **9**, 833-834.
21. G. R. Desiraju, J. J. Vittal and A. Ramanan, *Crystal Engineering: A Textbook*, World Scientific, 2011.
22. M. C. Etter, *The Journal of Physical Chemistry*, 1991, **95**, 4601-4610.
23. C. A. Hunter and J. K. M. Sanders, *Journal of the American Chemical Society*, 1990, **112**, 5525-5534.
24. C. R. Martinez and B. L. Iverson, *Chemical Science*, 2012, **3**, 2191-2201.
25. N. K. Duggirala, M. L. Perry, Ö. Almarsson and M. J. Zaworotko, *Chemical Communications*, 2016, **52**, 640-655.
26. P. Bowles, S. J. Brenek, S. Caron, N. M. Do, M. T. Drexler, S. Duan, P. Dubé, E. C. Hansen, B. P. Jones, K. N. Jones, T. A. Ljubicic, T. W. Makowski, J. Mustakis, J. D. Nelson, M. Olivier, Z. Peng, H. H. Perfect, D. W. Place, J. A. Ragan, J. J. Salisbury, C. L. Stanchina, B. C. Vanderplas, M. E. Webster and R. M. Weekly, *Organic Process Research & Development*, 2014, **18**, 66-81.
27. N. R. Goud, O. Bolton, E. C. Burgess and A. J. Matzger, *Crystal Growth & Design*, 2016, **16**, 1765-1771.

28. J. S. Murray and P. Politzer, *Wiley Interdisciplinary Reviews: Computational Molecular Science*, 2011, **1**, 153-163.
29. K. B. Landenberger and A. J. Matzger, *Crystal Growth & Design*, 2010, **10**, 5341-5347.
30. S. Seth and A. J. Matzger, *Crystal Growth & Design*, 2017, **17**, 4043-4048.
31. Y.-S. Bae and R. Q. Snurr, *Angewandte Chemie International Edition*, 2011, **50**, 11586-11596.
32. L. E. Kreno, K. Leong, O. K. Farha, M. Allendorf, R. P. Van Duyne and J. T. Hupp, *Chemical Reviews*, 2012, **112**, 1105-1125.
33. U. P. N. Tran, K. K. A. Le and N. T. S. Phan, *ACS Catalysis*, 2011, **1**, 120-127.
34. C. Wang, D. Liu and W. Lin, *Journal of the American Chemical Society*, 2013, **135**, 13222-13234.
35. O. S. Bushuyev, G. R. Peterson, P. Brown, A. Maiti, R. H. Gee, B. L. Weeks and L. J. Hope-Weeks, *Chemistry – A European Journal*, 2012, **19**, 1706-1711.
36. K. A. McDonald, S. Seth and A. J. Matzger, *Crystal Growth & Design*, 2015, **15**, 5963-5972.
37. S. Zhang, Q. Yang, X. Liu, X. Qu, Q. Wei, G. Xie, S. Chen and S. Gao, *Coordination Chemistry Reviews*, 2016, **307**, 292-312.
38. X. Qu, S. Zhang, Q. Yang, Z. Su, Q. Wei, G. Xie and S. Chen, *New Journal of Chemistry*, 2015, **39**, 7849-7857.
39. D. Chen, S. Huang, Q. Zhang, Q. Yu, X. Zhou, H. Li and J. Li, *RSC Advances*, 2015, **5**, 32872-32879.
40. D. Chen, D. Jing, Q. Zhang, X. Xue, S. Gou, H. Li and F. Nie, *Chemistry – An Asian Journal*, 2017, **12**, 3141-3149.
41. S. Chen, B. Zhang, L. Yang, L. Wang and T. Zhang, *Dalton Transactions*, 2016, **45**, 16779-16783.
42. W. Gao, X. Liu, Z. Su, S. Zhang, Q. Yang, Q. Wei, S. Chen, G. Xie, X. Yang and S. Gao, *Journal of Materials Chemistry A*, 2014, **2**, 11958-11965.
43. N. Szimhardt, M. H. H. Wurzenberger, L. Zeisel, M. S. Gruhne, M. Lommel and J. Stierstorfer, *Journal of Materials Chemistry A*, 2018, **6**, 16257-16272.
44. S. Li, Y. Wang, C. Qi, X. Zhao, J. Zhang, S. Zhang and S. Pang, *Angewandte Chemie International Edition*, 2013, **52**, 14031-14035.

45. S. Seth and A. J. Matzger, *Inorganic Chemistry*, 2017, **56**, 561-565.
46. S. Seth, K. A. McDonald and A. J. Matzger, *Inorganic Chemistry*, 2017, **56**, 10151-10154.
47. S. S. Nagarkar, B. Joarder, A. K. Chaudhari, S. Mukherjee and S. K. Ghosh, *Angewandte Chemie International Edition*, 2013, **52**, 2881-2885.
48. R. Banerjee, H. Furukawa, D. Britt, C. Knobler, M. O'Keeffe and O. M. Yaghi, *Journal of the American Chemical Society*, 2009, **131**, 3875-3877.
49. R. Banerjee, A. Phan, B. Wang, C. Knobler, H. Furukawa, M. O'Keeffe and O. M. Yaghi, *Science*, 2008, **319**, 939-943.
50. A. Phan, C. J. Doonan, F. J. Uribe-Romo, C. B. Knobler, M. O'Keeffe and O. M. Yaghi, *Accounts of Chemical Research*, 2010, **43**, 58-67.
51. B. R. Pimentel, A. Parulkar, E. k. Zhou, N. A. Brunelli and R. P. Lively, *ChemSusChem*, 2014, **7**, 3202-3240.
52. K. Shen, X. Chen, J. Chen and Y. Li, *ACS Catalysis*, 2016, **6**, 5887-5903.
53. K. A. McDonald, J. C. Bennion, A. K. Leone and A. J. Matzger, *Chemical Communications*, 2016, **52**, 10862-10865.
54. M. B. Talawar, R. Sivabalan, T. Mukundan, H. Muthurajan, A. K. Sikder, B. R. Gandhe and A. S. Rao, *Journal of Hazardous Materials*, 2009, **161**, 589-607.
55. P. Politzer and J. S. Murray, *Propellants, Explosives, Pyrotechnics*, 2016, **41**, 414-425.
56. Decker, J. A.; Lon Santis; Scott Deitchman; Flesch, J. P.; Hagedorn, R. T. Carbon Monoxide Poisoning and Death After the Use of Explosives in a Sewer Construction Project (98-122)-CDC - National Institute of Occupational Safety and Health Publications and Products . https://www.cdc.gov/niosh/docs/98-122/default.html

Chapter 2

Cocrystal Engineering with a High-Nitrogen Energetic Material

Published in *Cryst. Growth Des.* **2018**, *18*, 219-224

2.1 Introduction

Compounds containing a large percentage of nitrogen offer a unique approach to the development of energetic materials (explosives, propellants, and pyrotechnics). In such materials, the major decomposition product is N_2, resulting in the release of a significant amount of chemical energy during decomposition derived from large, positive heats of formation. High nitrogen energetics contrast with traditional energetic materials, in which the major source of energy is provided by oxidation of a carbon rich backbone during decomposition.[1] Attractive features of high nitrogen explosives generally include: 1) high crystal density, 2) insensitivity to initiation by impact, friction and electrical discharge, 3) environmentally benign decomposition products, and 4) minimal generation of smoke.[2-5]

Efforts to improve energetic materials have traditionally relied on covalent synthesis of new molecules, a process that is both labor intensive and failure prone. Recently, cocrystallization has emerged as an alternative approach to synthetic modification. This method has proven valuable to the modification of existing materials properties and we therefore sought to apply the approach to high nitrogen compounds. Conventionally, cocrystallization is employed to modify the stability and bioavailability of active pharmaceutical ingredients (APIs), which often contain strong hydrogen bond donating and accepting groups.[6-7] In contrast, many energetic materials lack reliable and extensive synthons that are useful for the formation of cocrystals. As a result, cocrystals are not known for the vast majority of energetic materials and even for those that can form cocrystals,[8-15] an understanding of the types of coformers that are suitable must be developed, at least in part, through empirical screening. Herein, the single and

multicomponent crystallization of the energetic material is investigated with 3,6-bis(1H-1,2,3,4-tetrazol-5-yl-amino)-1,2,4,5-tetrazine, abbreviated BTATz, as an example from the emerging class of high nitrogen energetic materials.

BTATz contains 79 wt% nitrogen and burns with minimal smoke due to its low carbon content. As a result of these features, BTATz has been applied as a fire suppressant, a gas generating ingredient in automobile airbags, and a solid rocket motor propellant.[1,3-5,16-19] Like many other tetrazine derived energetics, BTATz suffers from poor solubility in most organic solvents and, perhaps as a result, only the dimethyl sulfoxide (DMSO) solvate crystal structure has been previously reported.[1] In this chapter, the crystal structure of single component BTATz is presented as well as new solvates and cocrystals that highlight the synthons and extended motifs that are successful in producing multicomponent BTATz crystals. Energetic performance predictions calculated with Cheetah 7.0 thermochemical software are also discussed.

2.2 Results and Discussion

Cocrystallization is challenging and in cases where predictable intermolecular interactions are absent, the problem is even more acute. One approach that can suggest the complementarity of two potential cocrystallization partners is calculation of electrostatic potential maps. Typically represented as an isodensity surface, these maps depict the dimensions and overall charge distribution of a molecule with respect to regions of positive, negative, and neutral electrostatic potential. This type of map provides a convenient way to visualize the potential donor and acceptor sites that can prove beneficial in the formation of a cocrystal. The corresponding maps for BTATz and several coformers are shown in Figure 2.1, wherein blue denotes regions of positive potential and red denotes regions of negative potential. Each map has points where the surface potential is at a maximum ($V_{s,max}$) and minimum ($V_{s,min}$). These points

were calculated to explain why some coformers are successful cocrystallization partners with BTATz, while others are not. Strong and complementary intermolecular interactions favor cocrystallization, although other factors, such as shape and lattice energy of each component, also contribute to success in producing a given cocrystal. From these maps, the known DMSO solvate structure is understood to form due to the $V_{s,min}$ calculated at -233.2 kJ/mol for DMSO, a value consistent with a strong H-bond acceptor complementary to the $V_{s,max}$ of BTATz (Figure 2.1). Using the calculated $V_{s,min}$ for DMSO as a benchmark, we undertook the synthesis of cocrystals that would probe synthon reliability in high nitrogen energetic materials. The coformers selected for this study (DMF, pyridine, pyridine *N*-oxide, 2-pyridone, and pyrazine) have $V_{s,min}$ smaller in magnitude than that of DMSO to test the limits of hydrogen bond acceptor potential.

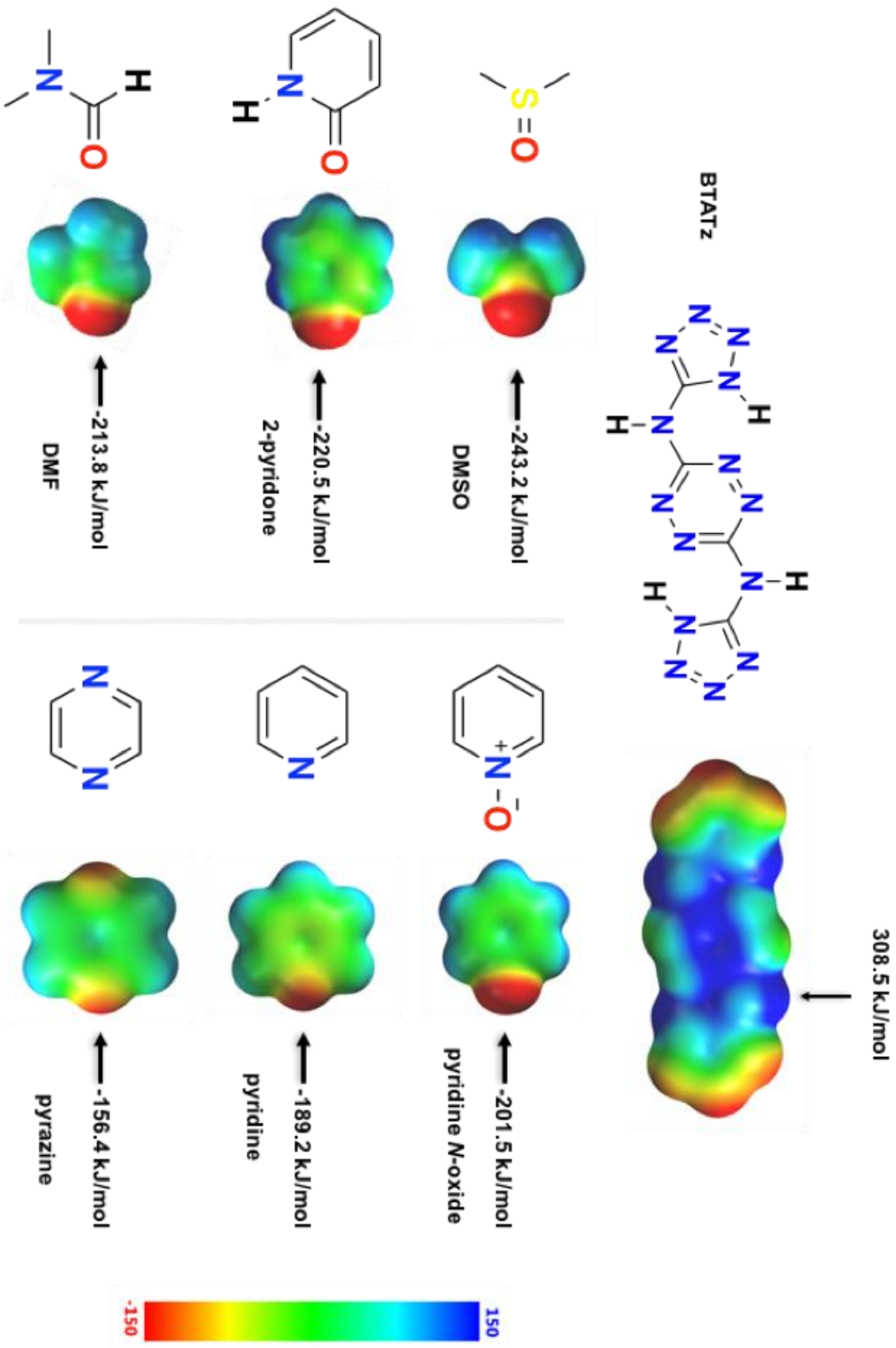

Figure 2.1 Chemical structures and electrostatic potential surfaces of BTATz and coformers calculated using the density functional method B3LYP/6-31+G**

Despite numerous studies on BTATz synthesis and properties[4, 16, 17,18,24,25], the solvent-free crystal structure had not previously been reported. The pursuit of cocrystals with BTATz in this study led to the discovery of the single component structure for the first time. Crystals of pure BTATz were grown from hot water by layering acetonitrile anti-solvent containing pH adjusting additives. Crystallization of BTATz is pH sensitive and single component crystals grow best in solutions that are weakly acidic; small amounts of 5-nitro-1,2,4-triazol-3-one or acetic acid work well as additives to facilitate growth of single component BTATz. It is important to note that the additives used here are not incorporated into the crystal structure. BTATz crystallizes in the monoclinic crystal system and solves in the $P2_1/n$ space group. The asymmetric unit consists of half of a BTATz molecule located on an inversion center. In this structure, hydrogen bonding plays a dominant role in the packing arrangement of BTATz, with NH···N interactions from bridging amines to terminal tetrazoles. 1-D chains are formed by dimerization of the terminal tetrazole rings with secondary amines (Figure 2.2a). In the 2-D structure these chains are interdigitated with respect to adjacent chains wherein a tetrazole ring is inserted between neighboring tetrazole rings to build up corrugated sheets through a hydrogen bonded network (Figure 2.2b). This 2-D motif also displays a close edge-to-face π–π interaction where the tetrazine ring interacts with a tetrazole ring on another molecule. The corrugated sheets are held together by slipped stacking interactions to form a 3-D packing arrangement through π–π stacking interactions (closest short contact interaction is 3.02 Å) with tetrazole rings and bridging amines (Figure 2.2c). The density of pure BTATz is 1.90 g/cm^3 at 85 K and 1.78 g/cm^3 at 298 K (vide infra).

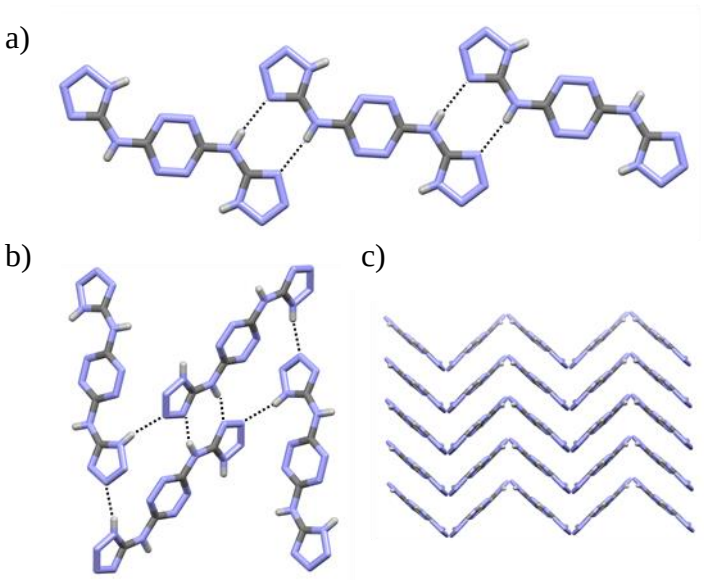

Figure 2.2 a) 1-D hydrogen bonding pattern of BTATz, b) 2-D sheets formed by interdigitated BTATz chains, c) 3-D wave-like packing motif

Previous reports suggest that explosives with conjugated molecular structures tend to be more insensitive to mechanical stimuli when compared to structures that lack π interactions. The π-stacked layers are proposed to respond to stimuli by converting mechanical energy into intermolecular interaction energy that disperses throughout π-stacked layers.[20-21] This redistribution minimizes local molecular vibrations, decreasing the mechanical and impact sensitivity of energetic materials. The crystal structure of BTATz features edge-to-face geometries and π-stacked sheets that arrange in a wave-like structure. Zhang and coworkers investigation of crystal packing of low-sensitivity explosives suggests that wave-like packing arrangements permit molecules to slide, restricted to one direction, without molecular decomposition.[21] BTATz is insensitive to thermal and mechanical stimuli, and it is likely that the insensitivity of this energetic material is influenced by this structural feature.

Five new multicomponent crystals were discovered and they form in 4:1, 2:1 and 1:1 molar ratios with BTATz. 2-Pyridone, the amide tautomer of 2-hydroxypyridine, contains one

amine donor and one oxygen acceptor. 2-Pyridone has a $V_{s,\,min}$ value of -223.2 kJ/mol, making it 22.7 kJ/mol more positive than DMSO, suggesting that it exhibits weaker hydrogen bond acceptance potential. In order to grow cocrystals of BTATz/2-pyridone, the pure solid components were gradually heated to 120 °C. At this temperature, 2-pyridone melts and dissolves BTATz. The liquid phase is held at this temperature for one hour and then slowly cooled to room temperature. As the solution begins to solidify, cocrystals form. BTATz/2-pyridone cocrystals have a 1:4 stoichiometry, are orange, and grow in a plate habit. The asymmetric unit consists of two 2-pyridone molecules and one half of a BTATz molecule, which sits on an inversion center. The hydrogen bonding network features NH···O hydrogen bonds (Figure 2.3), which form an extended zig-zag packing motif. The presence of hydrogen bond donor and accepter moieties on the coformer allows for the dimerization of 2-pyridone, which influences the high ratio of coformer molecules relative to BTATz.

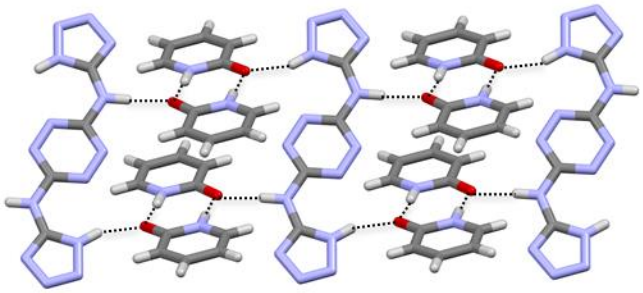

Figure 2.3 Crystal structure of 1:4 BTATz/2-pyridone cocrystal

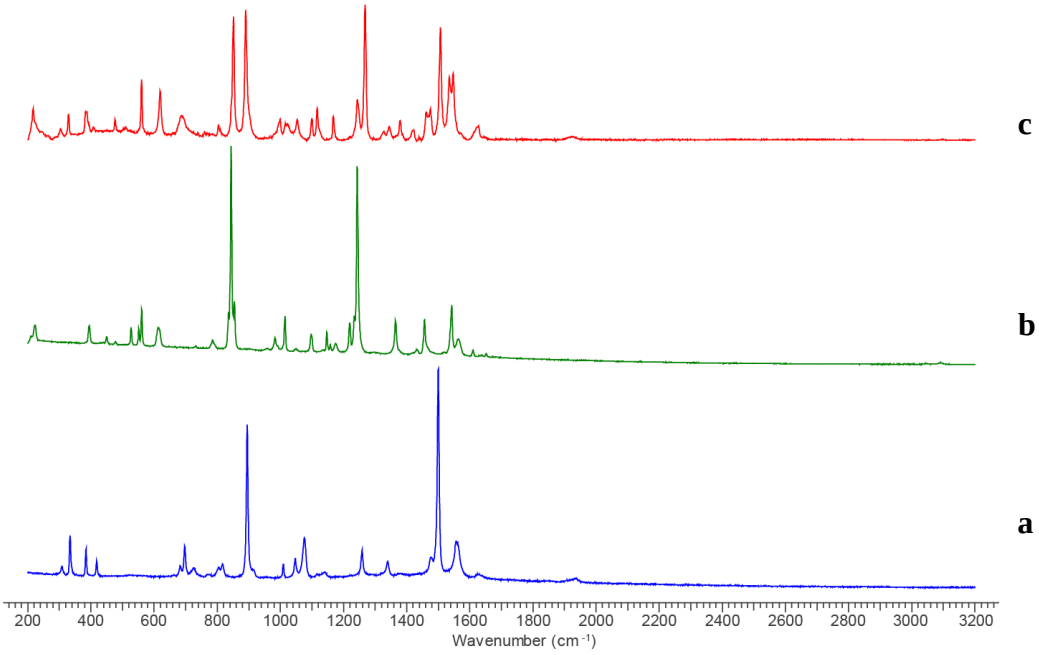

Figure 2.4 Raman spectra comparison of a) BTATz b) 2-hydroxypyridine and c) 1:4 BTATz/2-hydroxypyridone

N,*N*-Dimethylformamide (DMF) forms large solvate crystals with BTATz in a 1:2 ratio (1 BTATz: 2 DMF) by slow evaporation. The $V_{s,min}$ at the oxygen acceptor site on DMF is -213.8 kJ/mol, suggesting it is an even weaker acceptor than 2-pyridone. The crystal structure features N-H···O synthons that are identical to those present in the previously reported DMSO di-solvate structure. More specifically, the crystal structure features a hydrogen bonding network between BTATz secondary amine donors and oxygen acceptors on DMF. Although DMF functions as a hydrogen bond acceptor in the presence of BTATz, it does not interrupt the amine homodimer synthon between neighboring BTATz molecules as shown in Figure 2.5, which is likely due to the aprotic nature of DMF. In this solvate structure, BTATz forms a tape motif identical to that observed in the solvent-free BTATz structure. The preservation of this motif is consistent with the lower stoichiometric ratio when compared to 2-pyridone.

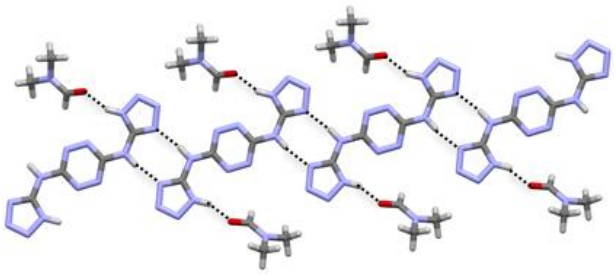

Figure 2.5 1:2 BTATz/ *N, N*-dimethylformamide

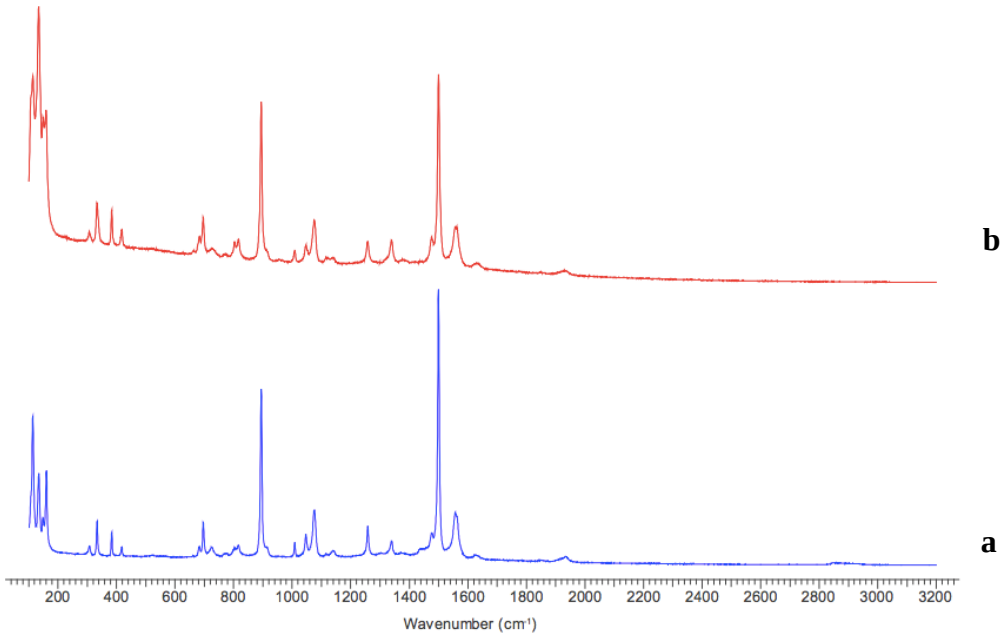

Figure 2.6 Raman spectra comparison of a) BTATz and b) 1:2 BTATz/ *N,N*-dimethylformamide

Pyridine *N*-oxide and pyridine each contain one hydrogen bond acceptor site. The local $V_{s,\ min}$ for the acceptor sites on pyridine *N*-oxide and pyridine are -204.6 and -190.6 kJ/mol, respectively. The two structures are similar; solving in the same space group ($P2_1/c$) and having comparable cell dimensions. Each structure features 1-D chains supported by parallel displaced π-π interactions between the coformer molecules. The asymmetric unit of the BTATz/pyridine *N*-oxide structure consists of two pyridine *N*-oxides and half BTATz. Pyridine *N*-oxide

molecules sit on a screw axis, while BTATz resides on an inversion center along each axis. A 2-D layered structure is established exclusively by NH···O hydrogen bonding. Primary interactions observed in the 2-D structure are tetrazole N-H to N-O on pyridine *N*-oxide, as well as bridging amine N-H on BTATz to N-O on pyridine *N*-oxide. Furthermore, the 3-D packing motif is formed through weak, short contacts including C-H···O contacts between two pyridine N-oxide molecules and C-H···N contacts which form heterodimers with pyridine N-oxide molecules and BTATz. Pyridine *N*-oxide and pyridine interrupt the intramolecular hydrogen bonding of BTATz by accepting protons from each amine on the backbone. The stoichiometric ratio of these multi-component crystals is 1:4 BTATz/coformer and this is likely due to the ability of pyridine and pyridine *N*-oxide to interrupt the formation of the BTATz homodimer. In the solvate structure with DMF which is 1:2 BTATz/coformer this motif is preserved. This trend suggests that the BTATz homodimer is crucial to the stoichiometry of BTATz multi-component crystals because it has some control over the ratio of donors and acceptors accessible to cocrystal formers.

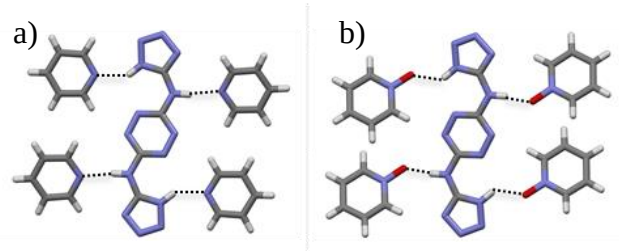

Figure 2.7 a) 1:4 BTATz: pyridine, b) 1:4 BTATz: pyridine *N*-oxide

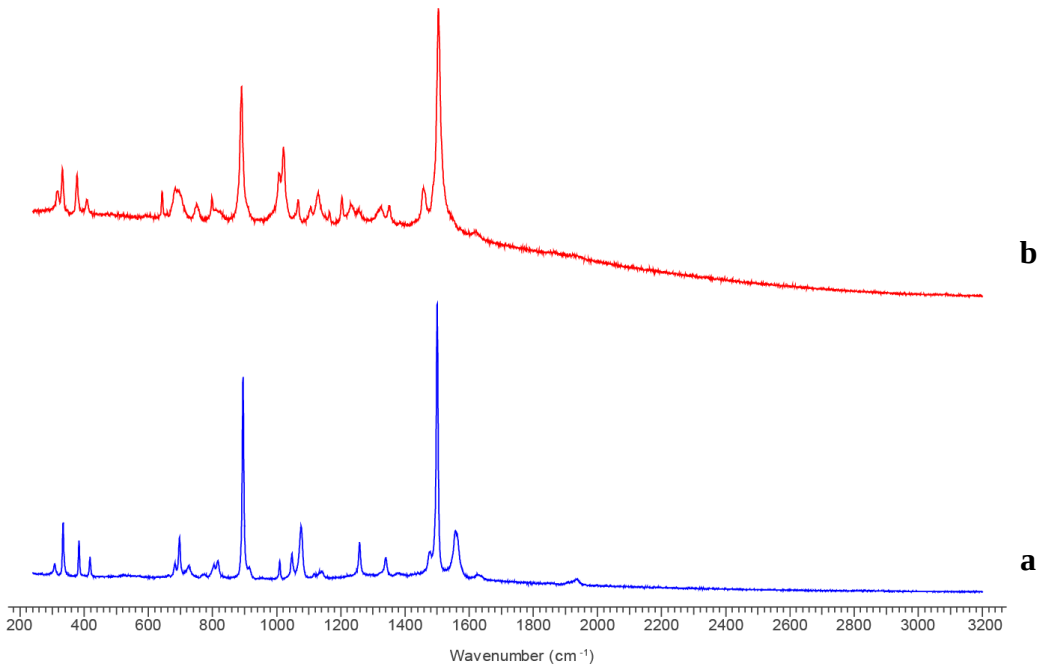

Figure 2.8 Raman spectra comparison of a) BTATz and b) 1:4 BTATz/pyridine

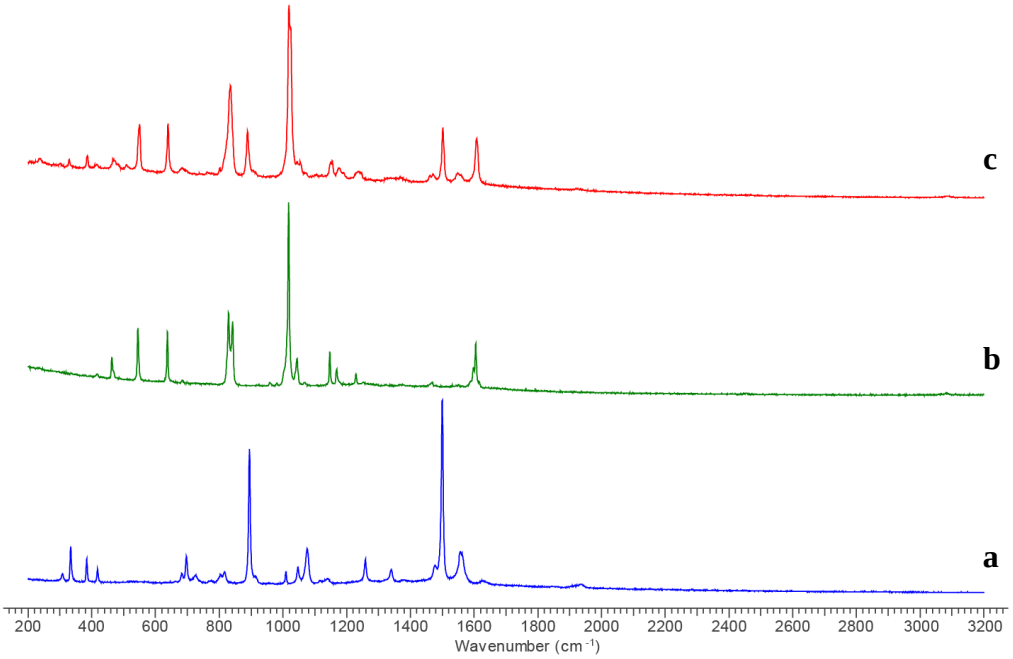

Figure 2.9 Raman spectra comparison of a) BTATz b) pyridine *N*-oxide and c) 1:4 BTATz/ pyridine *N*-oxide

The packing motif obtained between pyrazine and BTATz is unique relative to the previous crystal structures described in this study because it introduces the possibility of bridging BTATz molecules through the two hydrogen bond accepting sites on pyrazine (Figure 2.10). This di-acceptor interaction influences the stoichiometry of the cocrystal, which is the first example of a 1:1 cocrystal with BTATz. The 1:1 stoichiometry is influenced by two structural features: conservation of the BTATz homodimer and hydrogen bond donation from the tetrazole rings to each acceptor on pyrazine. In addition to exhibiting a unique packing motif, the BTATz/pyrazine cocrystal pushes the acceptor $V_{s,\ min}$ to its furthest limits as it has the most positive $V_{s,min}$ value of the coformers discussed (-156.4 kJ/mol).

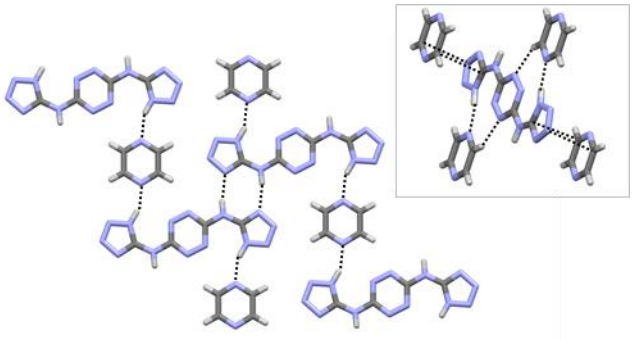

Figure 2.10 1:1 BTATz: pyrazine

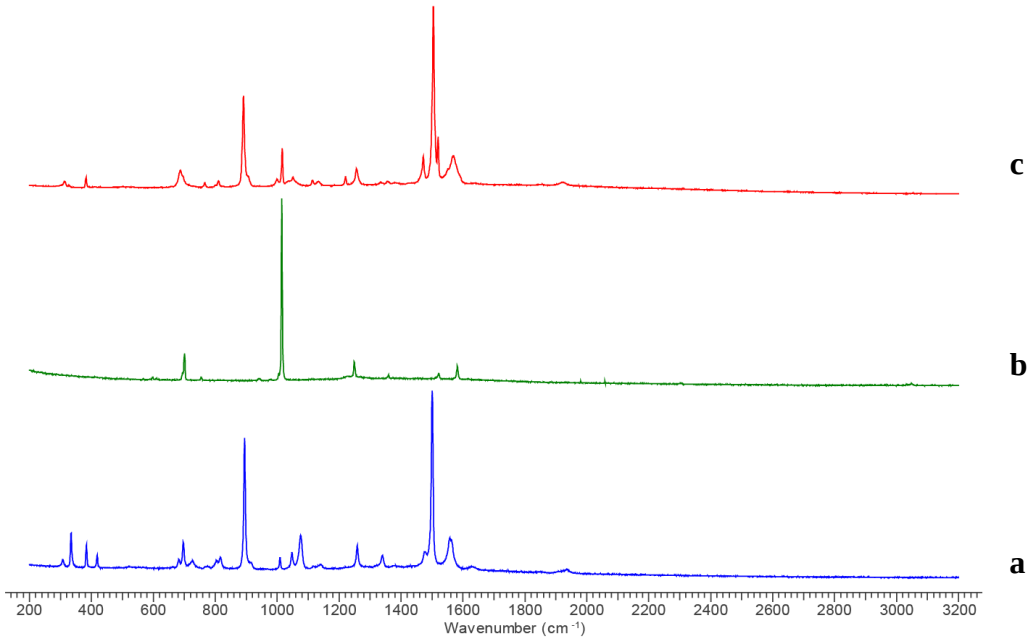

Figure 2.11 Raman spectra comparison of a) BTATz b) pyrazine and c) 1:1 BTATz/ pyrazine

Similar to the single component, the cocrystallization of BTATz/pyrazine is also pH sensitive and cocrystals were grown by layering acetonitrile/water solutions and using an acidic additive in the organic layer. The crystal structure features 2-D sheets formed by hydrogen bonding of tetrazole donors to pyrazine acceptors. The sheets are held together by close π-stacking interactions between tetrazole and pyrazine rings with interlayer distances from 3.25-3.27 Å, forming infinite 3-D layers. Face-to-face π-stacking plays a major role in the 3-D spatial arrangement and density of this cocrystal. The density of this cocrystal is 1.70 g/cm^3 at 85 K and 1.63 g/cm^3 at 295 K, which is the highest density among the multicomponent crystal structures reported here. The density of this structure can be attributed to short interlayer distances which allow the molecules to pack tightly.

Table 2.1 Crystallographic data for BTATz single and multi-component crystals (collected at 85 K)

BTATz & cocrystal formers	BTATz	BTATz: DMF	BTATz: Pyridine	BTATz: Pyridine N-Oxide	BTATz: 2-Pyridone	BTATz: Pyrazine
stoichiometry	-	1:2	1:4	1:4	1:4	1:1
space group	$P2_1/n$	P-1	$P2_1/c$	$P2_1/c$	P-1	P-1
a (Å)	4.8071(5)	9.1199(2)	6.13189(7)	6.50385(6)	7.6288(4)	6.3963(6)
b (Å)	11.8376 (12)	9.3988(2)	8.33230(7)	9.14767(10)	10.1896(4)	6.9500(8)
c (Å)	7.6113(8)	12.1476(9)	25.5961(2)	23.3299(3)	10.2679(5)	7.4999(5)
α (°)	90	88.347(6)	90	90	111.223(4)	76.297(8)
β (°)	91.639(9)	75.595(5)	92.4823(9)	92.2350(10)	102.736(4)	80.488(7)
γ (°)	90	61.572(4)	90	90	102.750(4)	84.745(8)
volume (Å^3)	432.94	881.981	1306.55	1386.96	684.949	318.98
Z	2	2	2	2	1	1
ρ $_{calc}$ (g/cm^3)	1.90	1.46	1.43	1.50	1.52	1.70

During cocrystallization experiments with BTATz, attempts were also made using a series of energetic coformers containing a carbonyl functionality, including K-6 (2-oxo-1,3,5-trinitro-1,3,5-triazacyclohexane), LLM-107 (1,4,5,7-tetranitro-1,4,5,7-tetraazabicyclo[4.3.0]nonan-6-one), and NTO (5-nitro-1,2,4-triazol-3one). Thus far these cocrystallizations have been unsuccessful likely because of these energetic materials lack good acceptors for BTATz. The energetic coformers K-6, LLM-107, and NTO have $V_{s,\ min}$ values ranging from -141 to -118 kJ/mol which are all more positive in magnitude than the $V_{s,\ min}$ of the successful coformers discussed above and is consistent with weaker hydrogen bond acceptor potential . This finding demonstrates how electrostatic potential plays a significant role in crystallization of BTATz with coformers, and therefore more polarized energetic materials may be required for successful cocrystallizations with this high-nitrogen energetic material.

Oxygen balance describes the theoretical ability of an energetic system to completely oxidize fuel into neutral, molecular components (CO_2, H_2O, N_2, etc.) during decomposition. An oxygen balance of 0% indicates a stoichiometric balance of oxygen to fuel within an energetic

system (conversion of carbon to CO_2, for example). A negative oxygen balance indicates an oxygen deficiency that results in unburned fuel (residue) or toxic byproduct (CO) due to incomplete combustion. By contrast, a positive oxygen balance indicates an excess of oxygen available after full conversion of fuel.[15, 22] Some examples of energetic materials with positive oxygen balances include with tetranitromethane (+49%), ammonium nitrate (+20%), and nitroglycerine (+3.5%). However, many energetic materials have a negative oxygen balance. For example, TNT, HMX and CL-20 have oxygen balances of -74%, -21% and -11% respectively. The oxygen balances of BTATz and its multicomponent crystals are negative, a result that is typical for organic molecules (Table 2.2). BTATz has an oxygen balance of -64% and this is influenced by the absence of oxygen and limited amount of carbon and hydrogen on the molecule. The oxygen balance of the cocrystals becomes more negative going from a 1:1 to 1:4 stoichiometric ratio of BTATz to coformer. Cocrystals with a 1:4 and 1:2 ratio of BTATz to coformer all exhibit oxygen balances <-100%. The most neutral oxygen balance for a BTATz cocrystal was achieved with the 1:1 BTATz:pyrazine cocrystal at -97%. These results show that a low stoichiometric ratio of coformer to BTATz would yield more neutral oxygen balances.

Table 2.2 [a] Onset decomposition temperature. [b] Decomposition temperature measured by DSC at 10 °C/min. [c] Oxygen balance[23]. [d]Detonation parameters (velocity and pressure) predicted with Cheetah 7.0 using the room-temperature (295 K) crystallographic density of each material and modeling the performance as a physical mixture of components.

BTATz/BTATz cocrystal	T_{onset}[a] **(°C)**	T_{decomp}[b] **(°C)**	**Oxygen Balance[c] (%)**	**Detonation Velocity[d] (m/s)**	**Detonation Pressure[d] (GPa)**
BTATz	320.5	338.9	-64.47	8055	25.39
2-pyridone	275.5	284.3	-142.54	-	-
pyridine *N*-oxide	223.6	248.5	-142.54	6591	14.14
pyrazine	308.9	323.2	-97.48	7015	17.35
PETN	-	165 [26]	-10.10	8469	30.48
TNT	283 [9]	-	-73.96	7079	19.96

The thermal behavior of BTATz and its cocrystals was explored using thermogravimetric analysis (TGA) and differential scanning calorimetry (DSC). Pure BTATz begins thermal decomposition at 320.5 °C and the exothermic decomposition peaks at 338.9 °C (Table 2.2). The multicomponent BTATz crystals, however, display additional thermal signatures relative to the single component BTATz material associated with changes in the more volatile coformers. 1:4 BTATz/2-pyridone decomposes at 284.3 °C and 1:4 BTATz/pyridine *N*-oxide decomposes at 248.5 °C, temperatures much lower than BTATz. In both cases the coformer leaves the crystal prior to decomposition of BTATz, therefore the lower temperature of decomposition observed for BTATz in these cases is consistent with formation of a less thermally stable form of BTATz. This is a significant finding with implications for BTATz production and use as it suggests some pure forms of BTATz are much less thermally stable than the crystalline form described above. Similar to these findings, DSC and TGA of the pyrazine cocrystal show the coformer leaving the cocrystal prior to thermal decomposition, although the onset of BTATz decomposition does not take place until 308.9 °C. The pure phase of BTATz that results from the loss of pyrazine is the most thermally stable of all forms of BTATz following loss of coformer. These examples demonstrate that cocrystallization can be used as a strategy to modulate the thermal sensitivity of BTATz.

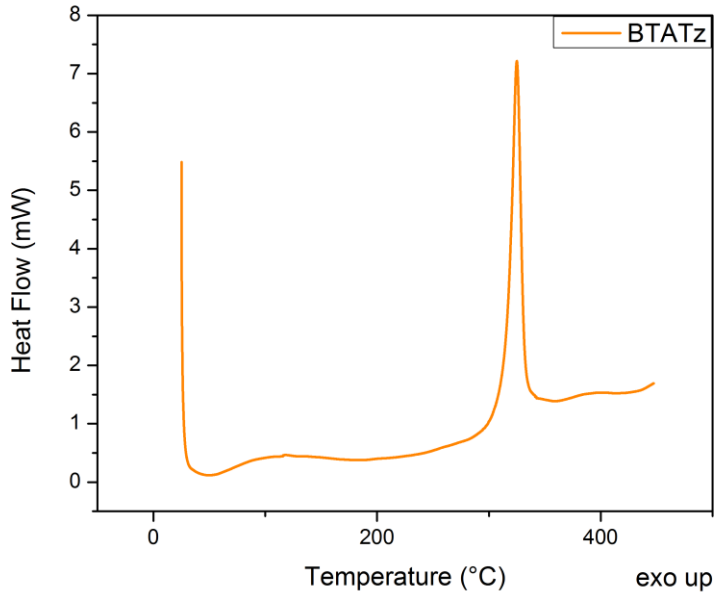

Figure 2.12 DSC trace of single component BTATz

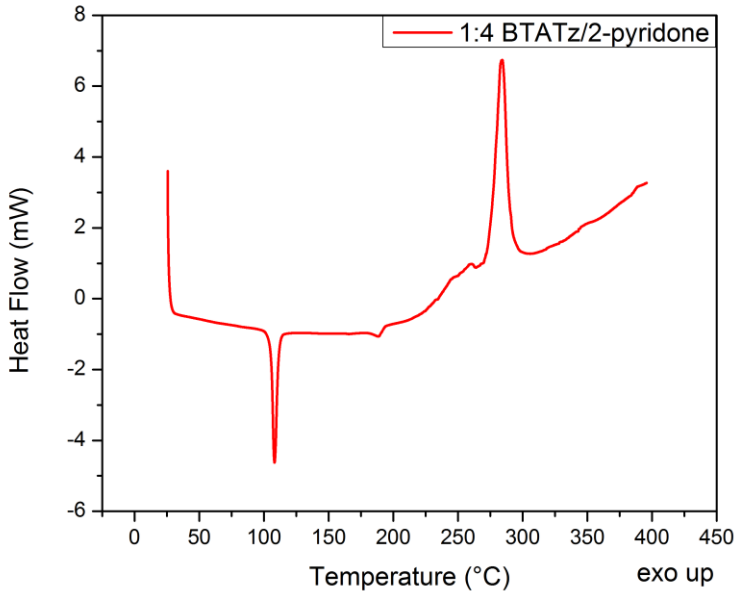

Figure 2.13 DSC trace of 1:4 BTATz/ 2-pyridone

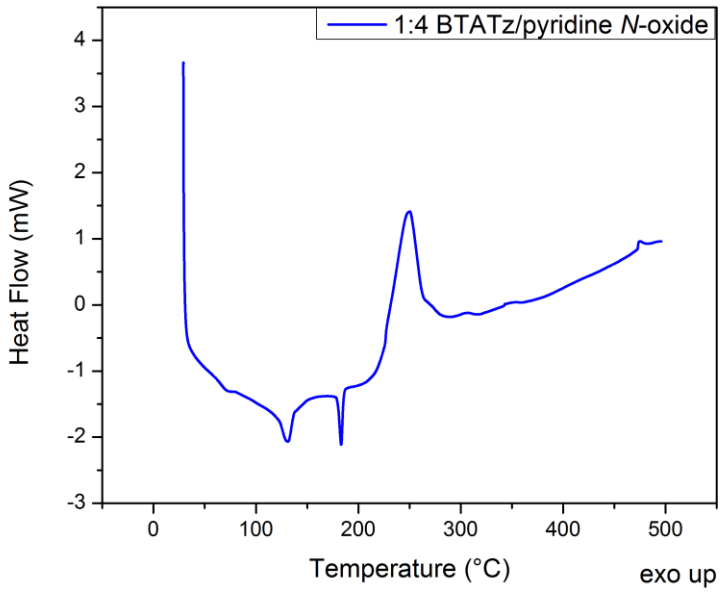

Figure 2.14 DSC trace of 1:4 BTATz/ pyridine *N*-oxide

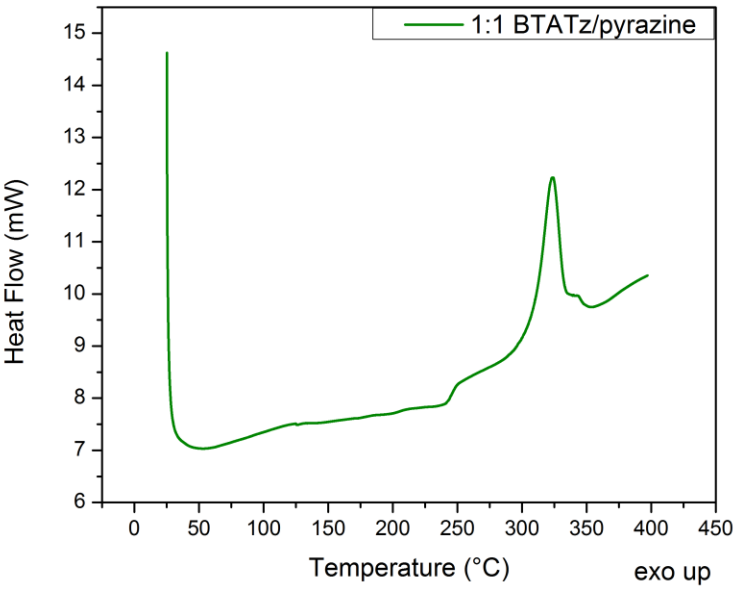

Figure 2.15 DSC trace of 1:1 BTATz/ pyrazine

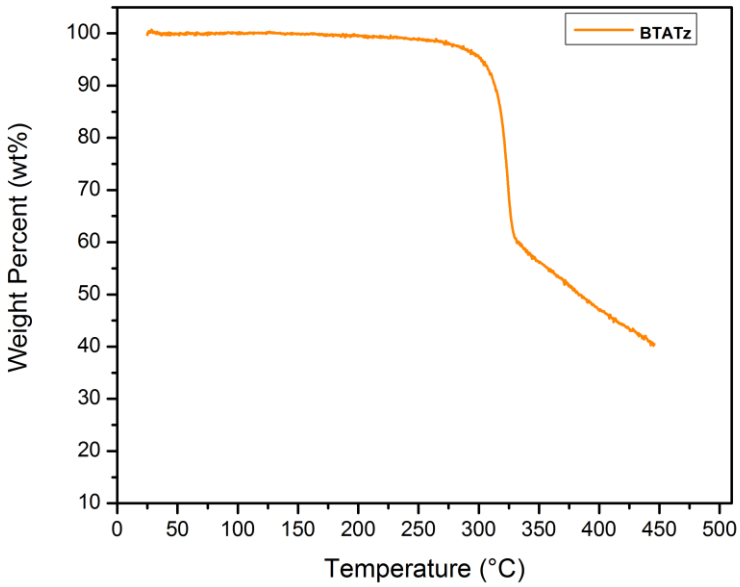

Figure 2.16 Thermogravimetric analysis of BTATz

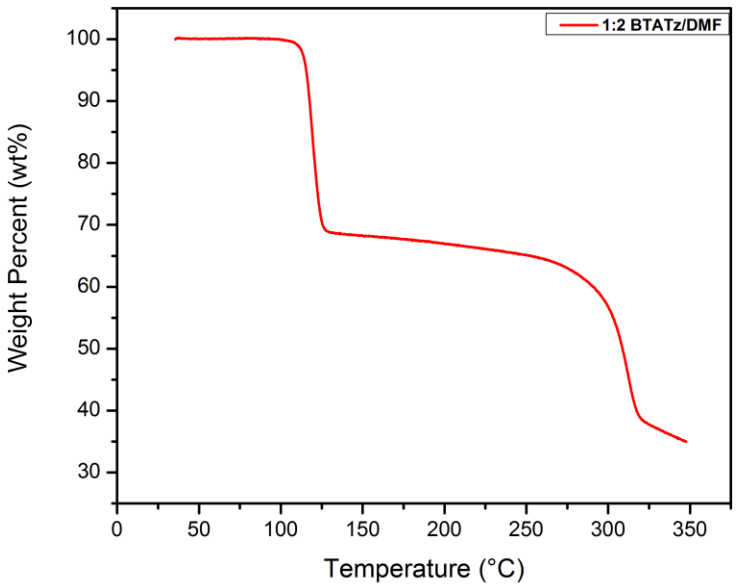

Figure 2.17 Thermogravimetric analysis of 1:2 BTATz/ *N*,*N*-dimethylformamide

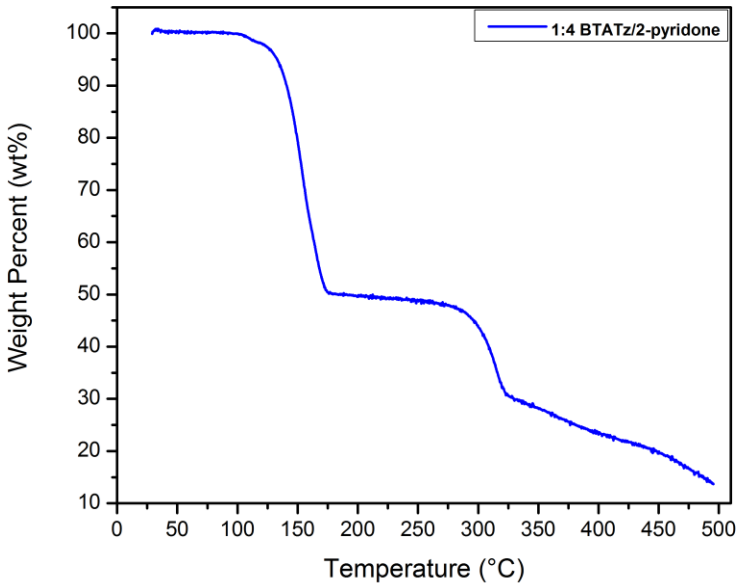

Figure 2.18 Thermogravimetric analysis of 1:4 BTATz/ 2-pyridone

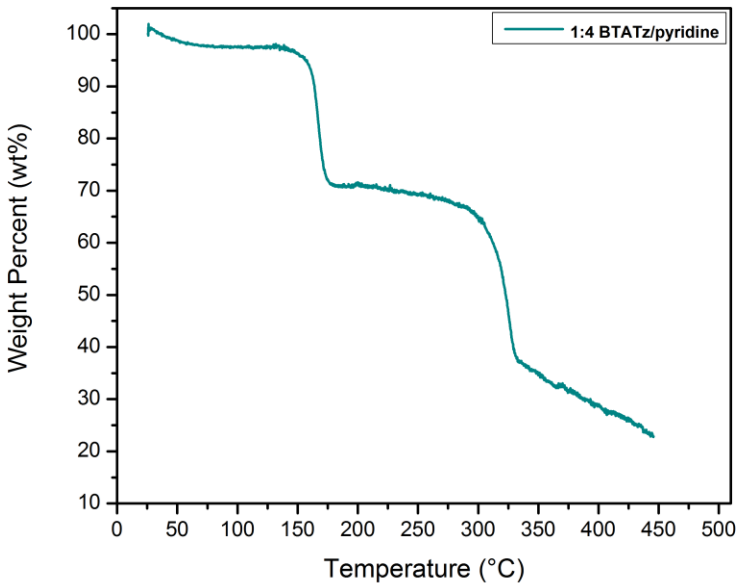

Figure 2.19 Thermogravimetric analysis of 1:4 BTATz/ pyridine

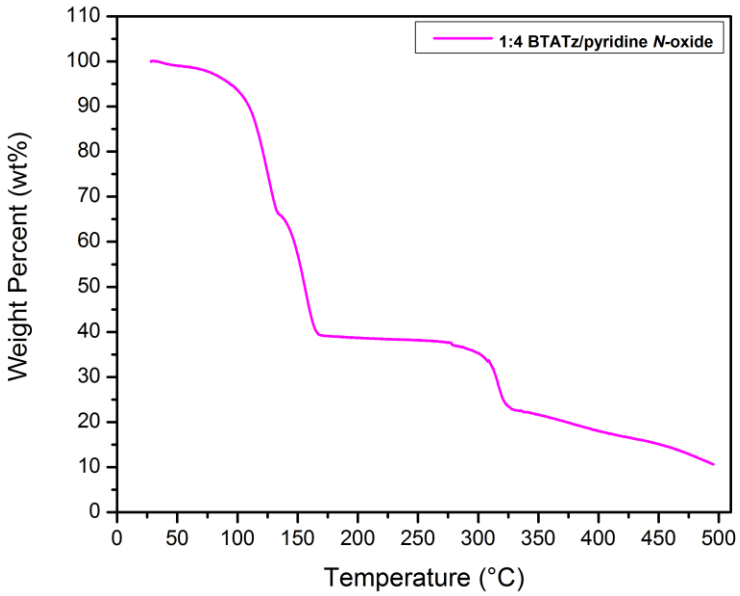

Figure 2.20 Thermogravimetric analysis of 1:4 BTATz/ pyridine *N*-oxide

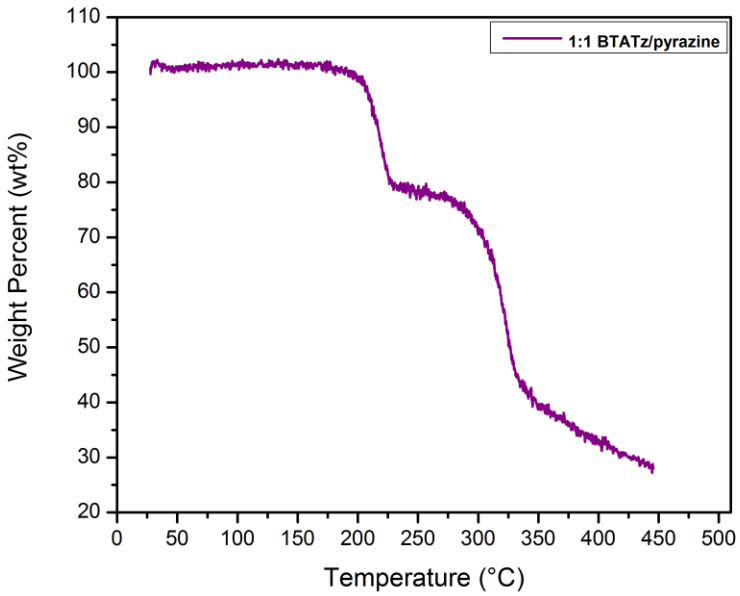

Figure 2.21 Thermogravimetric analysis of 1:1 BTATz/ pyrazine

Prior to this study, the energetic performance of BTATz was predicted using density values estimated with gas pycnometry.[1] This strategy gives insight into the potential performance

of the energetic, but has some limitations to understanding inherent material properties. With the density of the solvent-free structure discovered here, Cheetah 7.0 calculations were performed on BTATz and its cocrystals to explore their energetic performance. The main performance criteria extracted from Cheetah 7.0 calculations include detonation velocity (m/s) and detonation pressure (GPa). Impact sensitivity was also experimentally determined for the highest performing cocrystal.

Detonation velocity is the rate of propagation of the shock wave during detonation of an explosive and is strongly influenced by material density. BTATz has a detonation velocity calculated at 8055 m/s (Table 2.2), a value that falls between well-known secondary explosives PETN (pentaerythritol tetranitrate) and TNT (2,4,6-trinitrotoluene). The 1:1 BTATz/pyrazine cocrystal has a detonation velocity of 7015 m/s and the corresponding value for 1:4 BTATz/ pyridine *N*-oxide is 6591 m/s. These values are very close to TNT in spite of the presence of non-energetic coformers. Similar trends are also observed with the detonation pressure of these materials. Detonation pressure influences the brisance of an explosive and it increases proportionally to the density squared of an energetic material. BTATz has a detonation pressure of 25.4 GPa, which again falls between the values of PETN (30.5 GPa) and TNT (20.0 GPa). This data confirms BTATz as a high-performance secondary energetic material. Additionally, the 1:1 BTATz/pyrazine cocrystal also shows promise as an energetic material with detonation pressure comparable to TNT.

BTATz is a thermally stable energetic material; however, reliable impact sensitivity data is unknown. Impact sensitivity is reported as dH_{50} which represents the drop height at which the likelihood of detonation is at 50%. The impact sensitivity of BTATz and 1:1 BTATz/ pyrazine were investigated by small-scale drop testing with an in-house constructed apparatus. While

BTATz decomposed when impacted from 207 cm, detonation was not observed for BTATz/pyrazine when impacted from 217 cm, which is the limit of the apparatus. These findings show that a meaningful reduction in the impact sensitivity of BTATz can be achieved through cocrystallization with non-energetic materials. BTATz/pyrazine is very impact insensitive thus contributing to its safe to handling and transport.

2.3 Conclusion

BTATz is a particularly challenging target for cocrystallization due to its poor solubility and strong intermolecular interactions. Classes of molecules capable of disrupting these intermolecular interactions were identified and six new single and multicomponent materials were discovered with BTATz, demonstrating the diversity of crystallographic motifs that can be achieved by this compound. The utility of electrostatic potential maps as a tool to probe coformer potential with BTATz was demonstrated and this strategy can be extended to additional high nitrogen energetic compounds. The detonation velocities and pressures were calculated for each of the successful multicomponent crystals and the thermal decomposition investigated by TGA and DSC. From this data, the multicomponent crystal with the most desirable energetic performance, BTATz/pyrazine, was selected for impact sensitivity determination. The material was less impact sensitive than BTATz. Overall, this family of BTATz cocrystals demonstrate the capability for high nitrogen energetics to form multicomponent crystals and for coformers to modulate the thermal and impact sensitivities of high nitrogen energetic compounds.

2.4 Experimental Methods

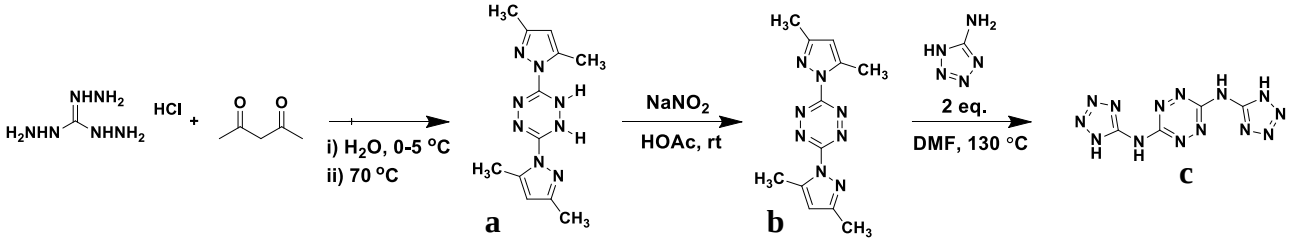

Reaction scheme for the synthesis of BTATz a) 3,6-bis(3,5-dimethylpyrazol-1-yl)-1,2-dihyrdo-1,2,4,5-tetrazine b) 3,6-(3,5-dimethylpyrazol-1-yl)-1,2,4,5-tetrazine c) 3,6-(1H-1,2,3,4-tetrazol-5-ylamino)-1,2,4,5-tetrazine (BTATz)

The synthesis of BTATz was completed following the synthesis published by Saikia et. al. with the following modifications. The first intermediate, **a**, was recrystallized from hot 2-propanol to afford yellow needles. The second intermediate, **b**, was recrystallized from hot ethanol to afford red needles. To synthesize the final product **c**, a 50 mL pressure tube was charged with **b** (0.501 g, 1.85 mmol) and anhydrous 5-aminotetrazole (0.377 g, 4.44 mmol). Dry DMF (6 mL) was added and the tube was capped and immersed in an oil bath. The reaction mixture was heated to 130 °C for 48 hours. A red solution was obtained and an orange solid precipitated. The reaction mixture was allowed to cool over 1 hour to room temperature, and the cap was removed. The orange solid was collected by vacuum filtration, washed with cold isopropanol and dried under high-vacuum. The obtained solid was identified by its spectral data which correspond to those previously reported.[27-29]

Single and Multi-Component Crystal Formation

BTATz. BTATz (9.26 μmol, 2.30 mg) was added to a vial and suspended into water (10 mL). The solution was heated to 100 °C and held for 2 hours. The solution was filtered and cooled slowly to room temperature overnight. The solution was heated to 70 °C. A separate solution of

acetonitrile (9 mL) and acetic acid (1 mL) was layered onto the aqueous BTATz solution while hot. The vial remained at 70 °C for an additional 2 hours and then slowly cooled to room temperature. Thin, light orange plates formed.

1:4 BTATz/ pyridine. BTATz (0.00411 mmol, 1.02 mg) was dissolved in pyridine (1 mL) and excess solvent slowly evaporated at room temperature to yield orange needles.

1:4 BTATz/ 2-pyridone. BTATz (0.00439 mmol, 1.09 mg) was added to a vial with 2-pyridone (0.320 mmol, 30.4 mg). The mixture was heated to 120 °C and held for 1 hour. The temperature was decreased by 10 °C/hour to 90 °C and held for 1 hour. The temperature was then decreased to 40 °C for 8 hours and then slowly cooled to room temperature. Red plates formed.

1:4 BTATz/ pyridine N-oxide. BTATz (0.00117 mmol, 0.29 mg) was added to a vial with pyridine *N*-oxide (0.362 mmol, 34.4 mg). The vial was heated to 80 °C and held for 1 hour. The temperature was slowly decreased by 10 °C/hour to 35 °C. The solution was held for 8 hours and then slowly cooled to room temperature. Dark orange prismatic crystals formed.

1:2 BTATz/ N,N'-dimethylformamide. BTATz (0.00399 mmol, 0.99 mg) was added to a vial and dissolved in *N,N'*-dimethylformamide (1 mL) at room temperature. The vial was added to a heat block set at 70 °C and uncapped. The vial remained on the heat block until excess solvent evaporated to yield orange prismatic crystals.

1:1 BTATz/ pyrazine. BTATz (0.0117 mmol, 2.91 mg) was added to a vial and suspended into 10 mL of water. The solution was heated to 100 °C and held for 2 hours. The solution was cooled slowly to room temperature overnight. The solution was heated to 70 °C. Pyrazine (0.791 mmol, 63.33 mg) was dissolved into a separate solution of acetonitrile (10 mL) and acetic acid (1 mL). The pyrazine/acetonitrile solution was layered onto the aqueous BTATz solution while hot. The vial remained at 70 °C for an additional 2 hours and then slowly cooled to room temperature. Orange plates formed.

Raman Spectroscopy

Raman spectra were collected using a Renishaw inVia Raman spectrometer equipped with a Leica microscope, 785 nm laser, and RenCam CCD detector. The system employed a 1200 lines/nm grating and a 65 μm slit width. The spectra were collected in extended scan mode with a range of 100-3200 cm^{-1} and analyzed using the WiRE 3.4 software package (Renishaw). Calibration was performed using a silicon standard in static mode.

Single Crystal Structure Determination

Single crystal X-ray diffraction data for single and multi-component crystals using a Rigaku AFC10K Saturn 944+ CCD based X-ray diffractometer equipped with a low temperature device and Micromax-007HF Cu-target micro-focus rotating anode (λ=1.54187 Å) operated at ½ kW power (40 kV, 30mA). The X-ray intensities were measured at 85 (1) K with the detector placed at a distance 42.00 mm from the crystal. Rigaku d*trek images were exported to CrysAlisPro for processing and corrected for absorption. The structure was solved and refined with the Bruker SHELXTL (version 2014/6) software package using direct methods. All non-hydrogen atoms were refined anisotropically with the hydrogen atoms placed in a combination of idealized and refined positions.

Computational Analysis[30]

Calculations on BTATz and other molecules were performed using SPARTAN '16. Geometries were optimized by DFT (B3LYP) calculations with the 6-31+G** basis set. The maxima and minima of each electrostatic potential is mapped on a surface with an isovalue of 0.002 au.

2.5 References

1. Chavez, D. E.; Hiskey, M. A. *J. Energ. Mat.* **1999**, *17*, 357-377.
2. Klapötke, T. M., High Energy Density Materials. *Springer Berlin Heidelberg.*, **2007**, *125*, 85.
3. Chavez, D.E.; Hiskey, M.A.; Gilardi, R. D. *Org. Lett.*, **2004**, *6*, 2889-2891.
4. Saikia, A.; Sivabalan, R.; Polke, B. G.; Gore, G. M.; Singh, A.; Rao, S.; Sikder, A.K. *J. Haz. Mat.*, **2009**, *170*, 306-313.
5. Hiskey, M.A.; Chavez, D.E.; Naud, D. L.; *Insensitive High Nitrogen Compounds, Los Alamos:* **2001**, LA-UR-01-1493.
6. Schultheiss, N.; Newman, A. *Cryst. Growth Des.* **2009**, *9*, 2950-2967.
7. Friščić, T.; Jones, W. *J Pharm. Pharmacol.* **2010**, *62*, 1547-1559.
8. Landenberger, K.B.; Matzger, A.J. *Cryst. Growth Des.* **2010**, *10*, 5341-5347.
9. Bolton, O.; Matzger, A. J. *Angew. Chem., Int. Ed.* **2011**, *50*, 8960-8963.
10. Landenberger, K.B.; Matzger, A.J. *Cryst. Growth Des.* **2012**, *12*, 3603-3609.
11. Bolton, O.; Simke, L.R.; Pagoria, P.F.; Matzger, A.J. *Cryst Growth Des.* **2012**, *12*, 4311-4314.
12. Landenberger, K.B.; Bolton, O.; Matzger, A.J. *Angew. Chem., Int. Ed.* **2013**, *52*, 6468-6471.
13. Landenberger, K.B.; Bolton, O.; Matzger, A.J *Cryst Growth Des.* **2015**, *137*, 5074-5079.
14. Bennion, J.C.; McBain, A.; Matzger, A.J. *Cryst Growth Des.* **2015**, *15*, 2545-2549.
15. Bennion, J.C.; Chowdhury, N.; Kampf, J.W.; Matzger, A.J. *Angew. Chem., Int. Ed.* **2016**, *128*, 13312-13315.
16. Wang, B.; Weipeng, L.; Liu, Q.; Lian, P.; Xue, Y. *Front. Chem. China.* **2009**, *4*, 69-74.

17. Chavez, D.E.; Hiskey, M.A.; Naud, D.L. *Propellants Expols., Pyrotech.* **2004**, *29*, 209-215.
18. Sinditskii, V.P.; Egorshev, V.Y.; Rudakov, G.F.; Burzhava, A.V.; Filatov, S.A.; Sang, L.D. *Thermochim. Acta* **2012**, *535*, 48-57.
19. Ali, A.N.; Son, S.F.; Hiskey, M.A.; Naud, D.L. *J Propul. Power* **2004**, *20*, 120-126.
20. Zhang, C.; Wang, X.; Huang, H. *J. Am.Chem.Soc.* **2008**, *130*, 8359-8365.
21. Ma, Y.; Zhang, A.; Zhang, C.; Jiang, D.; Zhu, Y.; Zhang, C. *Cryst. Growth Des.* **2014**, *14*, 4703-4713.
22. Steinhauser, G.; Klapötke, T.M. *Angew. Chem., Int. Ed.* **2008**, *47*, 3330-3347.
23. The oxygen balance for the organic energtic materials presented was calculated using the following equation: -1600(2a+(b/2)-c)/MW, wherein a, b, and c represent carbon, hydrogen and oxygen respectively, and MW represents the molecular weight of the material.
24. Chavez, D.E.; Tappan, B.C.; Hiskey, M.A.; Son, S.F.; Harry, H.; Montoya, D. *Propellants Expols., Pyrotech.* **2005**, *30*, 412-417.
25. Li, N.; Zhao, F.; Luo, Y.; Mao, H.; Xiao, L.; Gao, H.; An, T.; Hu, R. *J Solution Chem*, **2014**, *43*, 1250-1258.
26. Axthammer, O.J.; Krumm, B.; Klapötke, T.M. *Eur. J. Org. Chem.*, **2015**, *4*, 723-729.
27. Chavez, D. E.; Hiskey, M. A. *J. Energ. Mat.* 1999, *17*, 357-377.
28. Saikia, A.; Sivabalan, R.; Polke, B. G.; Gore, G. M.; Singh, A.; Rao, S.; Sikder, A.K. J. Haz. Mat., *2009*, *170*, 306-313.
29. Hiskey, M.A.; Chavez, D.E.; Naud, D. L.; *Insensitive High Nitrogen Compounds, Los Alamos:* **2001**, LA-UR-01-1493.
30. Sarwar, M.; Dragisic, B.; Salsberg, L.; Gouliaras, C.; Taylor, M. *J. Am. Chem. Soc.* 2010, *132*, 1646-1653

Chapter Three

Design of Energetic Coordination Polymers with BTATz

3.1 Introduction

Coordination polymers (CPs) represent a fascinating class of crystalline materials that can be solely inorganic/organic or metal-organic in composition. In the case of metal-organic CPs, polytypic organic ligands are coordinated to metal clusters or ions to produce 1D, 2D or 3D crystalline networks.[1, 2] In general, these polymeric structures are readily prepared under solvothermal synthesis conditions by the self-assembly of metal ions to organic ligands. The investigation of these highly ordered structures has led to a variety of potential applications including: gas storage, separations, and catalysis. [3, 4]

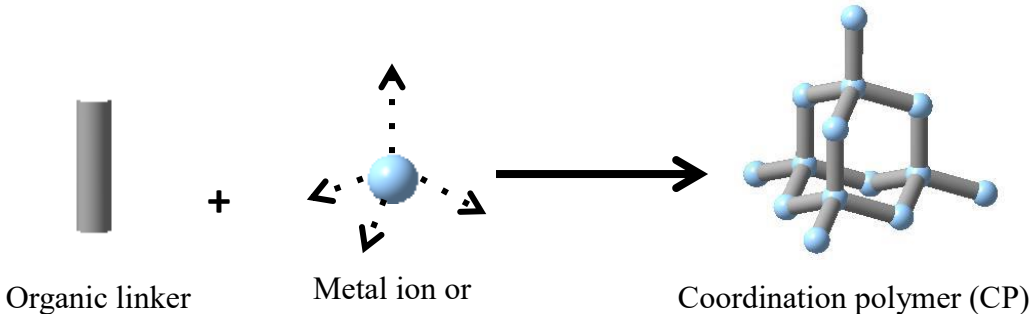

Figure 3.1 General reaction scheme of a coordination polymer synthesis

Recently, there has been a renewed interest in the development of CPs as energetic materials including explosives, propellants and pyrotechnics.[5, 6] Energetic materials (EMs) are compounds that typically contain fuel and oxidizer, and respond violently to stimuli (i.e. electrostatic, impact and thermal) by releasing large quantities of gases and energy.[7, 8] Explosives can be further subdivided into primary and secondary explosives based on the materials sensitivity to stimuli. Primary explosives are very sensitive to stimuli and they tend to exhibit low performance. As a result, primary explosives are used to generate a shockwave that will

propagate through the material and initiate a less sensitive, yet higher performing secondary explosive.[9-11]

Metal containing EMs date back to ~220 B.C. in ancient China with the discovery of black powder. The original composition of black powder is a physical mixture of 10% sulfur and 15% charcoal as fuel, and 75% potassium nitrate as the oxygen source.[7] Some modern EMs containing metal are synthesized such that the fuel and oxidizer exist within the same chemical structure, rather than in a physical mixture. Currently, there are EMs used in military and commercial applications that consist of toxic, heavy metals like mercury and lead.[9] Unfortunately, the decomposition of mercury and lead based EMs constitutes a major health and environment concern. This is because exposure to toxic metal contamination can cause adverse health effects in humans.[12] Recently, there has been a push in the field of EMs to develop new materials that avoid the use of heavy, toxic metals. Coordination polymers are a class of materials that could address this shift because new energetic CPs can be readily synthesized with non-toxic metal ions and high-energy ligands.[13] Additionally, CPs would make good energetic materials because the intermolecular interactions typically exhibited by solely organic molecules are replaced with shorter coordination bonds.[6] This replacement influences properties such as the density and stability of the CP. Properties that should be engineered into the design of new energetic CPs include high heat resistance, controllable sensitivity to external stimuli, production of environmentally benign reaction products, and large quantities of energy released upon decomposition.[5] The design of new energetic coordination polymers based on high-nitrogen content and non-toxic metals satisfies these requirements.

High nitrogen compounds have been increasingly investigated as ligands for energetic CPs because these compounds are inherently energetic and do not require oxidizing nitro groups

for large energy releases.[14-18] The purpose of the nitro group on the structure of energetic materials is to oxidize carbon and hydrogen fuel to generate gaseous products (i.e. CO_2 and H_2O). High nitrogen compounds contain limited amounts of carbon and hydrogen atoms so oxidizing substituents are not necessary.[19, 20] Instead, many high nitrogen compounds feature large positive heats of formation which promote substantial energy releases upon decomposition.[21, 22] The major decomposition product of high-nitrogen energetic materials is primarily N_2 which makes these compounds very attractive as environmentally friendly materials.[23] In the design of new high-nitrogen CPs, a variety of binding modes may be achieved through coordination of metal to nitrogen atoms in ligands. Depending on the metal ion, ligand geometry, and synthesis conditions, high-nitrogen compounds could be used to generate many new energetic CPs with 1D, 2D or 3D architectures. In particular, Zn (II) and Cu (II) metal ions are considered environmentally benign and both exhibit robust coordination capability with nitrogen containing ligands.[14, 24, 25] Successful high-nitrogen ligands include derivatives of triazoles, tetrazoles and tetrazines.

In 2013, Hope-Weeks and coworkers synthesized two energetic coordination polymers with bidendate hydrazine ligands and nickel/cobalt perchlorate salts (ClO_4^-). The two 1D polymeric energetic structures, NHP and CHP, exhibit a substantial energy release and high sensitivity to stimuli, which curtails their use in commercial applications.[26] In a continued effort by Hope-Weeks and coworkers to design lead-free coordination polymers with controllable sensitivity to stimuli, two additional polymeric structures were synthesized with a hydrazine derivative, hydrazinecarboxylate and cobalt/zinc perchlorate salts. The resulting structures, CHHP and ZnHHP, are 2D energetic coordination polymers.[27] A sensitivity assessment of the1D and 2D structures reveals that increased dimensionality results in structural stabilization from 1D

to 2D, and further motivates low sensitivity to stimuli and a reduction of the heat of detonation. This result highlights a general trend in energetic properties wherein as the heat of detonation of an explosive decreases, the impact sensitivity also decreases. Additionally, the heat of detonation has very little influence on the detonation velocity (D) and detonation pressure (P) of an explosive. D and P are energetic properties influenced by the material density and number of moles of gas (N_g) formed upon decomposition of the explosive.[28] CHHP and ZnHHP were predicted to perform similar to secondary organic explosives.

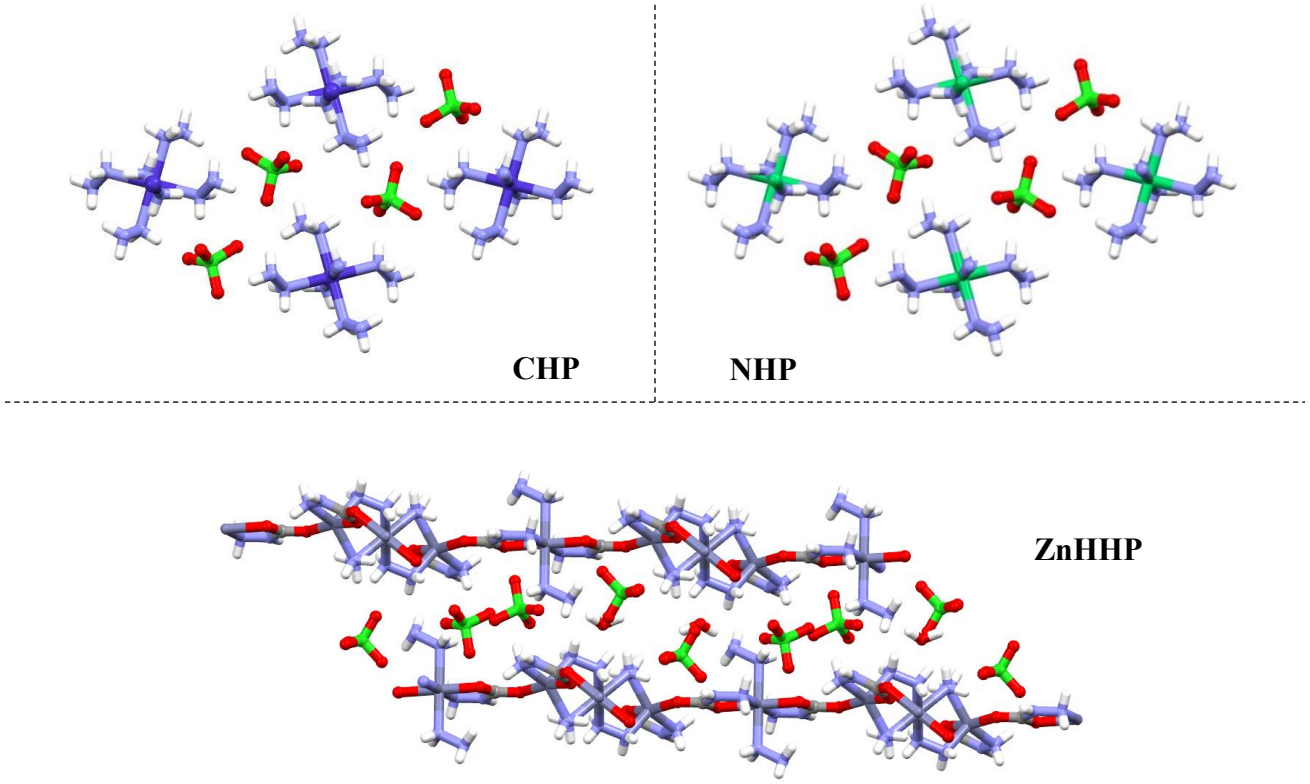

Figure 3.2 1D crystal structures of cobalt (II) hydrazine-perchlorate, CHP and nickel (II) hydrazine-perchlorate, NHP, and the 2D crystal structure of zinc (II) hydrazine hydrazinecarboxylate perchlorate, ZnHHP, which features perchlorate anions and water molecules between the ligand zinc dimers.

Despite the success of energetic coordination polymers with nitrogen rich ligands, there have been limited studies on energetic CPs that utilize known energetic materials as organic ligands. This method is perhaps the most straightforward strategy to synthesize energetic CPs.

An example of this concept was demonstrated by Matzger and coworkers, wherein two isostructural CPs were synthesized with 5-amino-3-nitro-1H-1,2,4,-triazole (ANTA) and Co/Zn ions. The resulting CPs Co-ANTA and Zn-ANTA are 2D and each framework exhibits improved solid state properties with respect to the organic ligand. ANTA is thermally stable up 225 °C, yet Co-ANTA and Zn-ANTA are thermally stable up to temperatures >300 °C.[29]

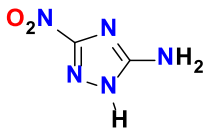

ANTA

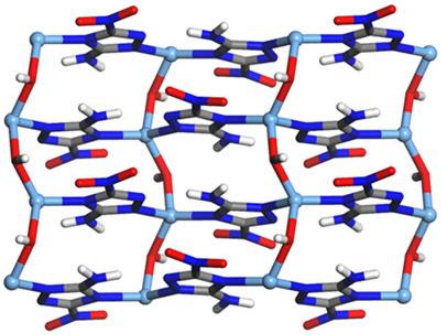

Zn-ANTA

(Co-ANTA structure is isostructural)

Figure 3.3 Chemical structure of the high nitrogen explosive material 5-amino-3-nitro-1H-1,2,4,-triazole (ANTA) and the 2D network showing nitrogen metal coordination from the triazole ring to cobalt anions. This structure also shows hydroxide anions bridging cobalt ions to form the 2D structure.

Further, Co-ANTA has a much higher impact sensitivity than ANTA, but Zn-ANTA is much less impact sensitive than both. This is likely due to the completely filled 3d subshell of Zn making it more stable to stimuli. In this chapter, the development of two new energetic CPs synthesized with a high-nitrogen energetic material, 3,6-bis(1H-1,2,3,4-tetrazol-5-ylamino)-s-tetrazine or BTATz, is discussed. BTATz was first synthesized at Los Alamos National Labs (LANL) and it is a 3-ring compound that contains two tetrazoles and one tetrazine ring with a total of 79 wt% of nitrogen.[21, 23, 30, 31]

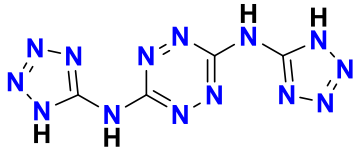

BTATz

Figure 3.4 Chemical structure of BTATz, a high-nitrogen energetic material containing three aromatic rings, two tetrazoles and one tetrazine.

This compound is an ideal energetic ligand because there are 10 potential sites of metal-nitrogen coordination and it exhibits excellent thermal stability >300 °C. This material is insensitive to impact wherein the drop height at which detonation is 50% likely (dH_{50}) is 207 cm. The energetic performance of BTATz is more superior than 2,4,6-trinitrotoluene (TNT) and 4-amino-3,5-dinitropyrazole (ADNP), and it is approaching 5-amino-3-nitro-1H-1,2,4,-triazole (ANTA). These attributes have led to a number of considerations for BTATz in air bags, fire suppressants, and solid rocket motor propellants. Additionally, BTATz contains very little carbon and therefore produces minimal smoke upon decomposition. These features make BTATz even more attractive from a energetics perspective because it exhibits low-signature upon decomposition.

Previous studies show that BTATz can form metal complexes with alkaline earth metals, strontium and calcium. However, accessing new solid forms with BTATz is challenging because it suffers from poor solubility in many organic solvents. To circumvent this problem, Song and coworkers report the synthesis of the BTATz potassium salt, $K_2(BTATz)\cdot 2H_2O$, prepared by stirring a solution of BTATz in *N,N*-dimethylformamide and adding a solution of aqueous potassium hydroxide dropwise at 60 °C. The solvent was evaporated and $K_2(BTATz)\cdot 2H_2O$ was collected by filtration. The strontium and calcium complexes were then synthesized by layering aqueous metal nitrate solutions either $Sr(NO_3)_2$ or $Ca(NO_3)_2$ onto a solution of $K_2(BTATz)\cdot 2H_2O$ in water. The layered solution was left to evaporate at room temperature for 1-2 weeks. The crystal structure of $[Ca_2(BTATz)_2(H_2O)\cdot 6H_2O]$ contains two Ca ions, two BTATz ligands, eight coordinated water molecules and three lattice water molecules. Similarly, the crystal structure of $[Sr_2(BTATz)_2(H_2O)_8\cdot 3H_2O]$ also contains two Sr ions, two BTATz ligands, eight coordinated water molecules and three lattice water molecules. The authors explored the thermal stability of

these new materials, but did not report the predicted nor experimental energetic performance of either metal complex. [32, 33]

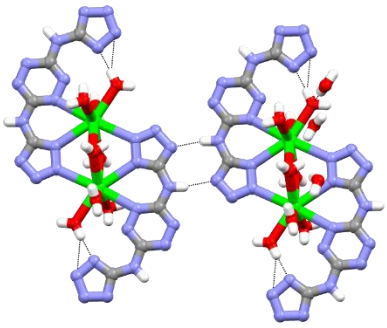

BTATz-Strontium Complex

Decomposition Temperature= 282 °C

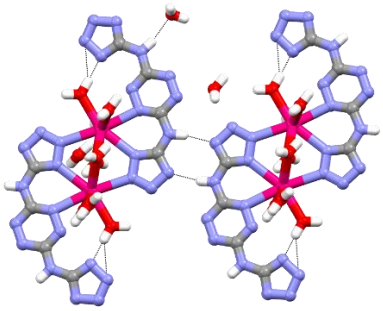

BTATz-Calcium Complex

Decomposition Temperature= 283 °C

Figure 3.5 Metal complexes with BTATz and alkaline earth metals calcium and strontium. Each crystal structure features binuclear units consisting of two metal ions coordinated to two deprotonated BTATz molecules and numerous water molecules.

However, it can be inferred that the inclusion of large quantities of water in each crystal structure will greatly dilute the energetic performance of BTATz. Therefore, the use of water in future CP synthesis with BTATz should be minimized or eliminated. BTATz is highly soluble in amide solvents which are often used in the solvothermal synthesis of coordination polymers.

3.2 Results and Discussion

Herein, two new high nitrogen energetic CPs were obtained by layering solutions of $Zn(NO_3)_2 \cdot 6H_2O$ in methanol onto a solution of BTATz in DMF. Depending on the concentration of $Zn(NO_3)_2 \cdot 6H_2O$ in methanol, either 1D or 2D ZnBTATz crystals will form. 1D ZnBTATz (**1**) structure forms in low concentrations of metal salt and grow best in a ratio of 1:2 BTATz:$Zn(NO_3)_2 \cdot 6H_2O$. The 2D-ZnBTATz (**2**) structure grows best at a ratio of 1:7 BTATz:$Zn(NO_3)_2 \cdot 6H_2O$ wherein the concentration of metal salt in methanol is much higher. A

key component in the synthesis of ZnBTATz CPs is the addition of small quantities of concentrated hydrochloric acid. This acid additive works to slow the rate of crystallization in solution because without the addition of HCl precipitate forms within 30 minutes of layering the DMF/MeOH solutions.

The crystal structures **1** and **2** were characterized by low-temperature single crystal X-ray diffraction. The structure of **1** crystallizes in the form of red cube shaped prisms in the hexagonal space group $R\bar{3}C$ with a calculated density of 1.451 g cm^{-3} at -20 °C. The asymmetric unit consists of one-half BTATz and one zinc ion. In this structure, three $BTATz^{2-}$ molecules participate in octahedral geometries around two zinc ions to form binuclear clusters. The nitrogen coordination to zinc ions is through each deprotonated terminal tetrazole on $BTATz^{2-}$ and through the nitrogen rich tetrazine ring where in two tetrazine atoms coordinate to each zinc ion. Additionally, the geometry of each $BTATz^{2-}$ molecule is different from the solvent-free parent structure revealing that BTATz is locked into a higher energy conformation because of potential steric hindrance by bridging amines. The structure of **2** crystallizes in the form of orange prisms in the hexagonal space group of R32 with a calculated density of 1.063 g cm^{-3} at -73 °C. The crystal structure of **2** also features the same binuclear zinc clusters observed in **1**. However, here nitrogen atoms on the terminal tetrazoles also coordinate to external zinc ions that bridge three neighboring binuclear clusters together to form 1D sheets. Further, one water molecule is also coordinated to the bridging zinc ion in each unit. The primary stabilizing interactions within the trimeric unit are N-H···N bonds between secondary amine proton donors and nitrogen acceptors on terminal tetrazoles with a bond distance of 1.85 Å. This H-bond interaction is shorter than the intermolecular hydrogen bonding between BTATz molecules (1.90 Å) in the single component crystal structure which is likely due to the presence of shorter

coordination bonds in CP structure. The 1D sheets are held together by N-H···N bonds between clusters to build up the 2D structure, and the hydrogen bond distance between the 1D sheets is 1.83 Å. Additionally, when the distance between the 1D sheets is measured from Zn···Zn it greatly increases to 9.41 Å. The density of **2** is very low compared to numerous other high-energy density CPs and given these structural features it is likely that the 2D structure is porous.

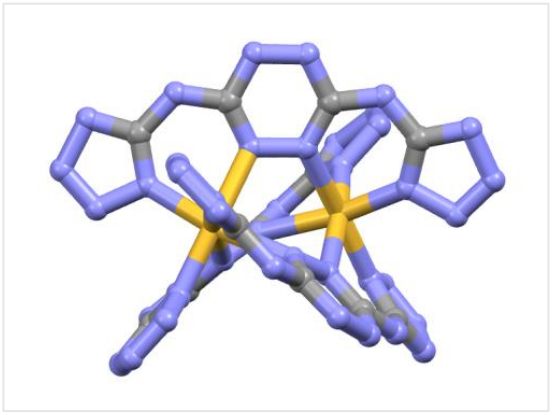

1D Zn-BTATz (**1**)

a (Å)	16.1
b (Å)	16.1
c (Å)	44.2
α (°)	90
β (°)	90
γ (°)	120
volume (Å^3)	10051.1
density (g/cm^3)	1.451
space group	R$\bar{3}$C

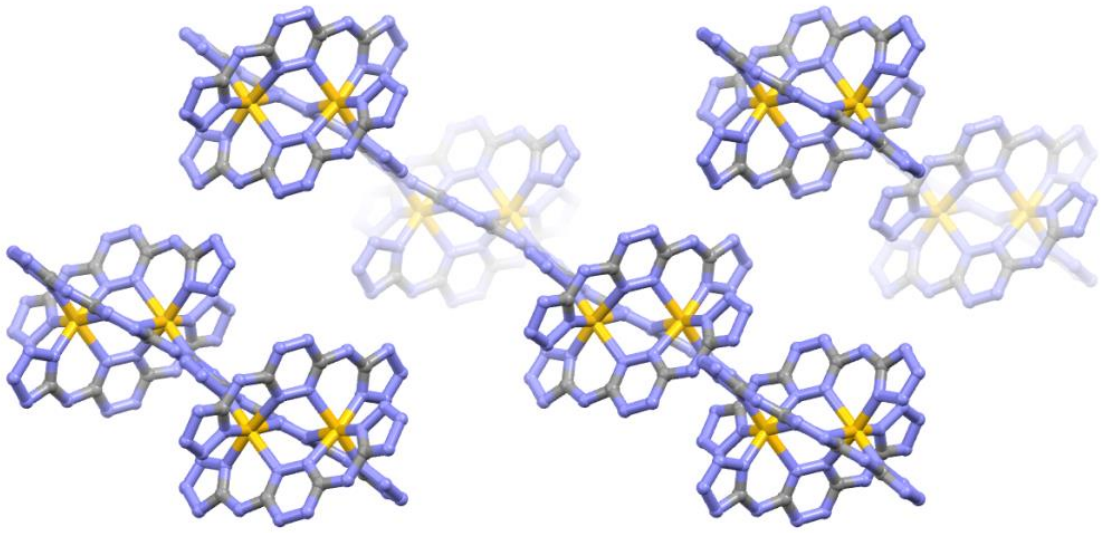

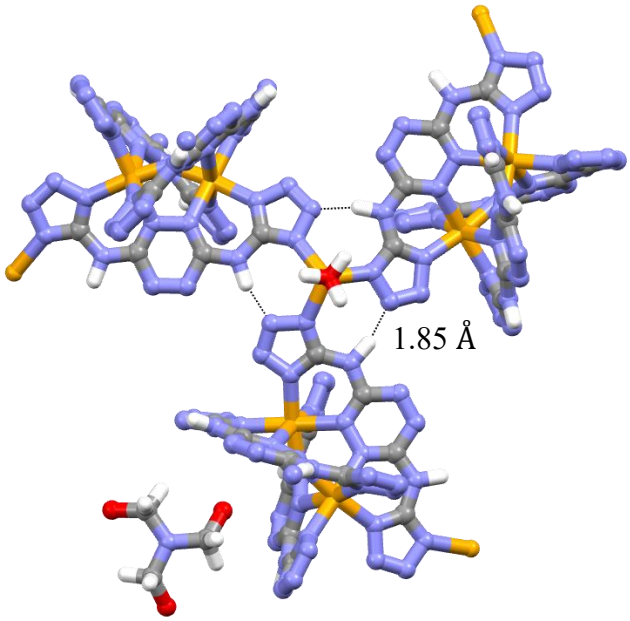

2D Zn-BTATz (**2**)

a (Å)	20.7
b (Å)	20.7
c (Å)	35.3
α (°)	90
β (°)	90
γ (°)	120
volume (Å^3)	13149.6
density (g/cm^3)	1.063
space group	R 3 2

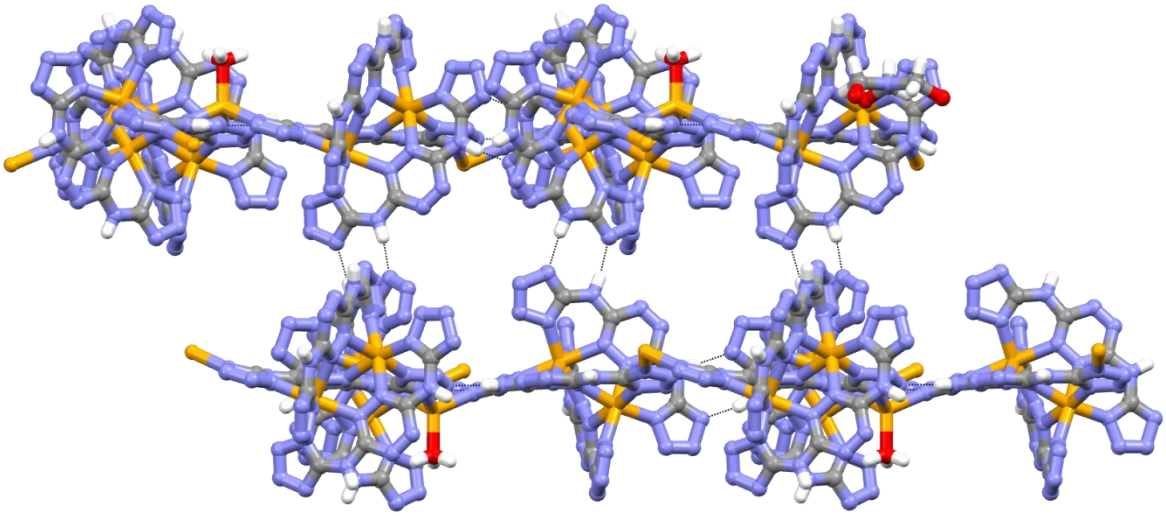

Figure 3.6 Structures and crystallographic data of 1D ZnBTATz (**1**) and 2D ZnBTATz (**2**)

The bulk phase purity of **1** and **2** was characterized by powder X-ray diffraction (PXRD) and the experimental pattern of each CP is consistent with the simulated powder patterns generated from crystallographic data. The structure of **2** remains ordered up to two weeks under ambient conditions as evidenced by PXRD analysis.

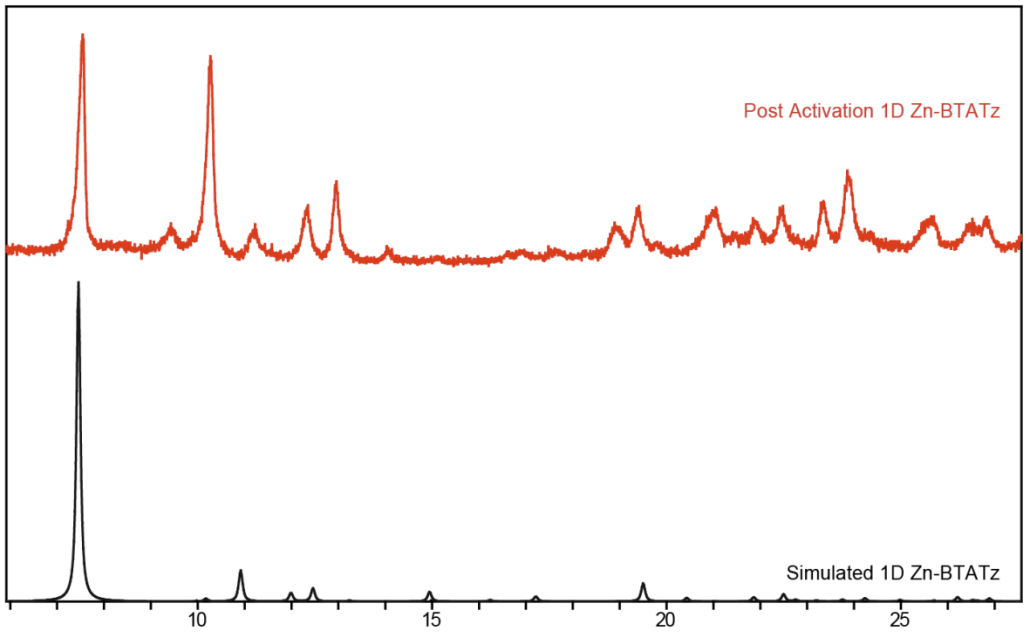
Post Activation 1D Zn-BTATz
Simulated 1D Zn-BTATz
10
15
20
25

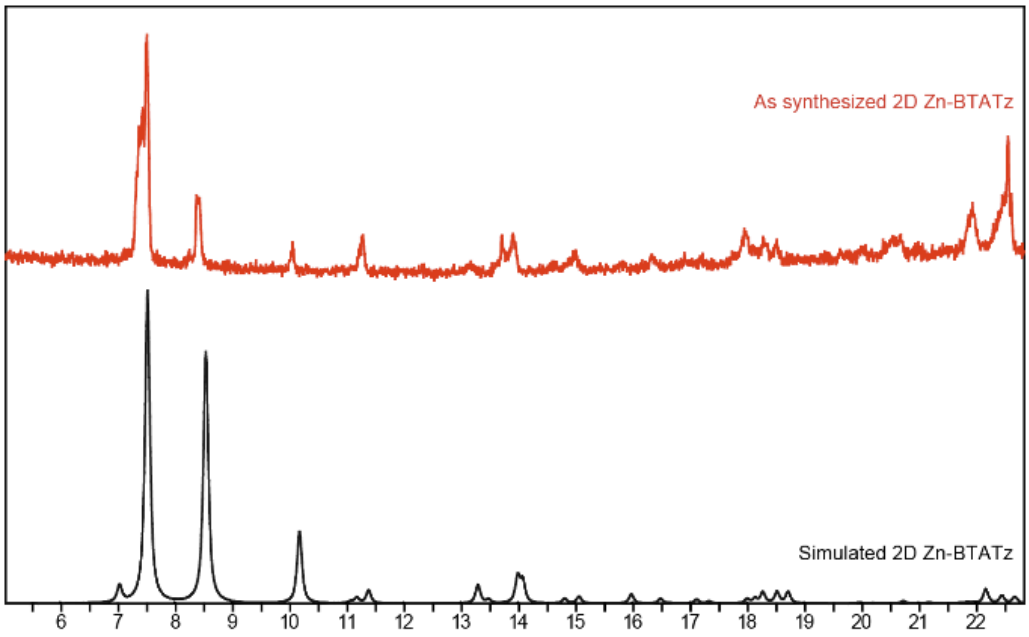
As synthesized 2D Zn-BTATz
Simulated 2D Zn-BTATz
6
7
8
9
10
11
12
13
14
15
16
17
18
19
20
21
22

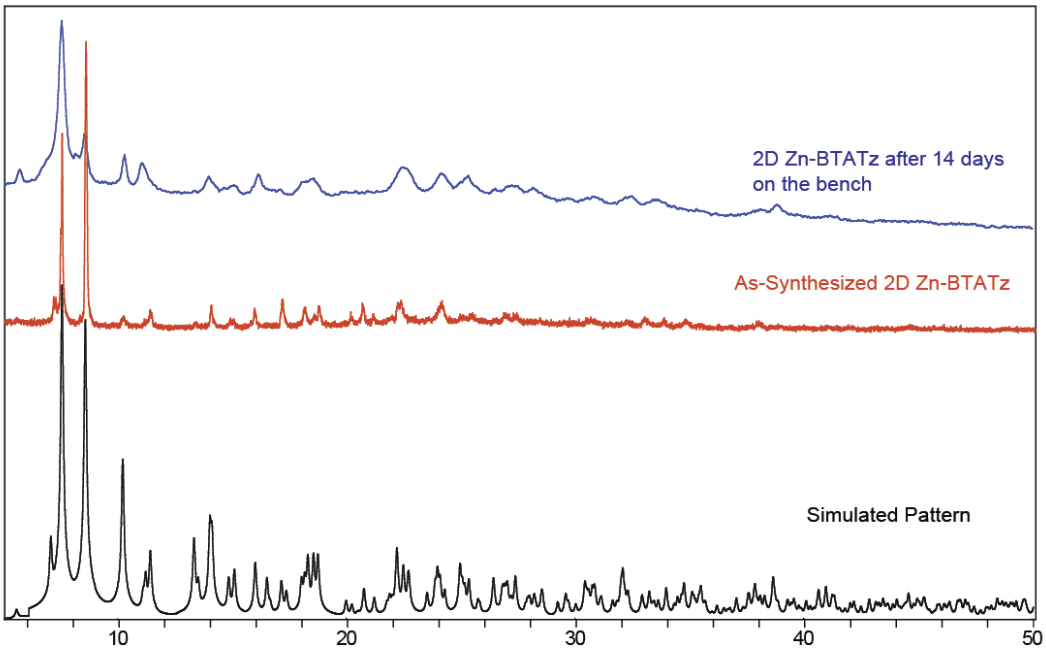

Figure 3.7 Powder patterns collected on bulk samples of as-synthesized **1** and **2**. Each experimental pattern is in good agreement with the simulated patterns confirming the purity of the bulk synthesis products.

The thermal decomposition behavior of **1** and **2** was examined by thermogravimetric analysis (TGA) and differential scanning calorimetry (DSC). In TGA the samples were heated from room temperature to 600 °C at a 10 °C min^{-1} ramp rate. The parent molecule BTATz undergoes an exothermic decomposition at 320 °C. TGA reveals that **1** undergoes ~5.4% weight loss below 200 °C followed by thermal decomposition of the CP. The DSC curve of **1** shows a substantial exothermic transition at onset temperature 240 °C. The thermal sensitivity of **2** is very similar to **1**. The TGA curve of **2** shows ~2.7% weight loss below 100 °C prior to thermal decomposition which likely corresponds to partial loss of water. The DSC curve of **2** shows a broad exothermic transition at 235 °C. Overall these results show that BTATz can be thermally sensitized by coordination to metal ions, and that sensitivity will vary depending on the stabilizing interactions and dimensionality of the CP.

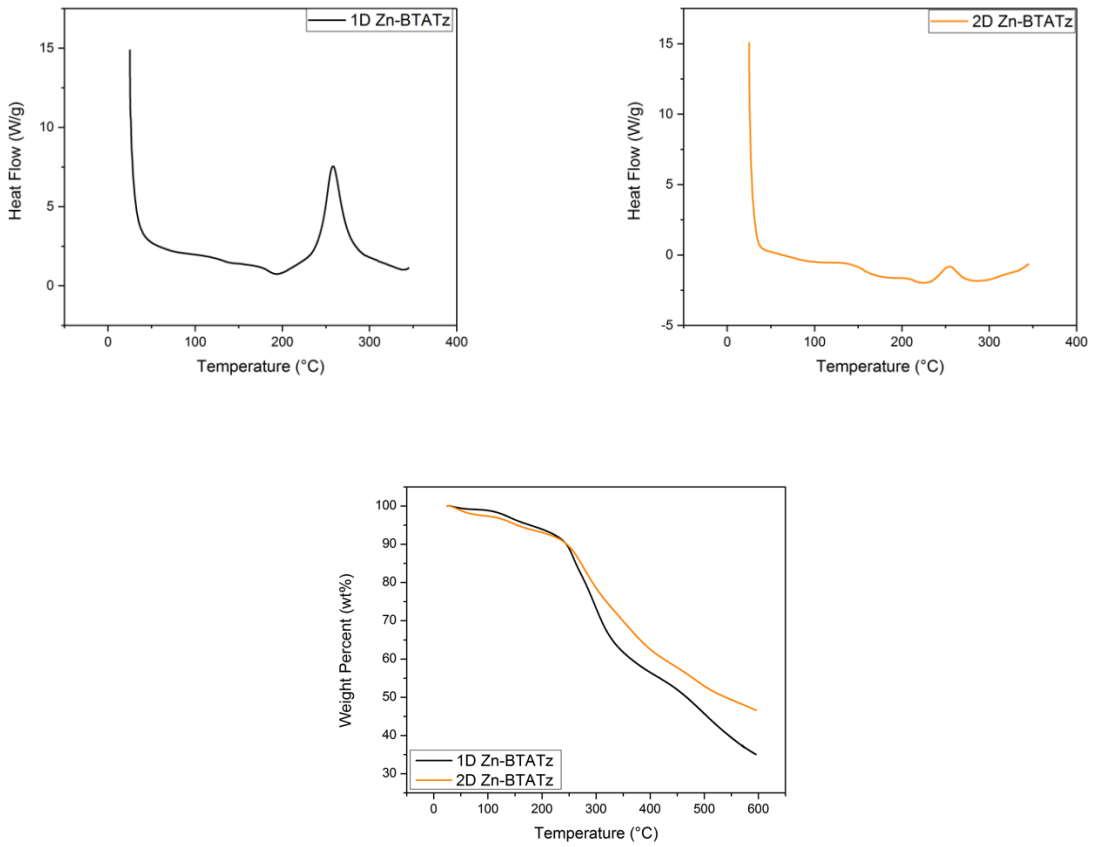

Figure 3.8 Thermal decomposition of **1** and **2** by DSC and TGA

Oxygen balance (OB%) is a calculation used to indicate the degree to which an energetic material may be oxidized by the oxygen present on the structure. If an energetic material contains a sufficient amount of oxygen to convert all carbon atoms to CO_2, water atoms to H_2O and metals to metal oxides upon decomposition then this explosive has an ideal oxygen balance of 0%. If the oxygen content is deficient then the molecule will most likely decompose into gaseous products and solid residue, indicating that some fuel will be wasted. A positive oxygen balance indicates that an excess of oxygen is availble to convert the fuel during combustion.[7, 34] Organic and inorganic energetic materials rarely have a sufficient number of oxidizing groups to achieve the ideal oxygen balance 0%, and therefore the oxygen balances for energetic materials are typically negative.[35] For example, the industry standard TNT has an oxgen balance of -74%

and this results in carbon soot or unburned fuel left over after combustion. Other examples of high explosives with negative OB% include CL-20 (-11.0%), HMX (-21.6%), and NTO (-24.6%). Like these energetic materials, structures **1** and **2** exhibit negative oxygen balances as well. Structure **1** has an oxygen balance of -55.1% and structure **2** has an oxygen balance of -49.4%. In comparison to the parent molecule BTATz which has an oxygen balance -64.5%, both of the ZnBTATz CPs have oxygen balances that are more neutral.

Sensistivity measurements are used to determine how energetic materials should be safely handled by personnel and transported. These measurements evaluate the sensitvity of energetic materials to various stimuli including impact. To determine a materials sensitivity to impact small-scale drop tests are performed. During this experiment a 5 lb. weight is allowed to freefall from varaiable heights onto 1.8-2.2 mg of sample contained in a non-hermetic DSC pan.[36] Drop tests are used to determine the drop height (in centimeters) at which detonation of the energetic is 50% likely, also known as the $Dh_{50\%}$ value. A positive response is accompanied by a loud noise and/or flash. For reference, the drop height of BTATz evaluated on our in-house appartatus is 207 cm. Drop tests with the new energetic CPs did not yield positive responses after impact from 217 cm, the limit of the appartatus. These results indicate that **1** and **2** are both more impact insensitive than BTATz.

3.3 Conclusion

In summary, coordination polymerization was utilized to access new 1D and 2D strucutres with the high-nitrogen energetic BTATz. 1D ZnBTATz (**1**) and 2D ZnBTATz (**2**) both contain octahedral metal geometries with binuclear clusters. These structures exhibit very similar thermal decomposition behavior and compared to the parent molecule BTATz, each structure is more thermally sensitive indicating that metal coordination to zinc can sensitize energetic

materials. More neutral oxygen balances were also observed with **1** and **2**, and this was accomplished through the deprotonated structure of $BTATz^{2-}$. Finally, the impact sensitivity was evaluated by small-scale drop tests and both 1 and 2 exhibit drop heights >217cm making both materials more insensitive than BTATz. Here coordination polymerization has proven to be a successful a design strategy for high-nitrogen energetic materials to access new eco-friendly energetic coordination polymers and improve upon oxygen balance and impact sensitivity.

3.4 Experimental Methods

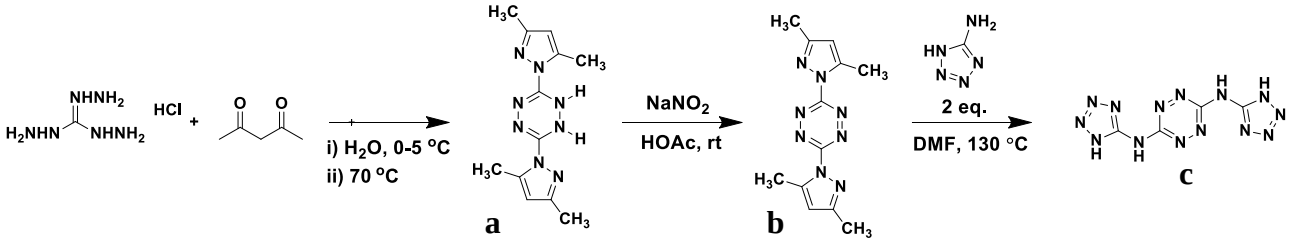

Reaction scheme for the synthesis of BTATz a) 3,6-bis(3,5-dimethylpyrazol-1-yl)-1,2-dihyrdo-1,2,4,5-tetrazine b) 3,6-(3,5-dimethylpyrazol-1-yl)-1,2,4,5-tetrazine c) 3,6-(1H-1,2,3,4-tetrazol-5-ylamino)-1,2,4,5-tetrazine (BTATz)

The synthesis of BTATz was completed following the synthesis published by Saikia et. al. with the following modifications. The first intermediate, **a**, was recrystallized from hot 2-propanol to afford yellow needles. The second intermediate, **b**, was recrystallized from hot ethanol to afford red needles. To synthesize the final product **c**, a 50 mL pressure tube was charged with **b** (0.501 g, 1.85 mmol) and anhydrous 5-aminotetrazole (0.377 g, 4.44 mmol). Dry DMF (6 mL) was added and the tube was capped and immersed in an oil bath. The reaction mixture was heated to 130 °C for 48 hours. A red solution was obtained and an orange solid precipitated. The reaction mixture was allowed to cool over 1 hour to room temperature, and the cap was removed. The orange solid was collected by vacuum filtration, washed with cold isopropanol and dried under

high-vacuum. The obtained solid was identified by its spectral data which correspond to those previously reported.[Ref]

1D ZnBTATz (1). BTATz (0.012 mmol, 3 mg) was added to a glass vial and dissolved in dry *N*,*N*-dimethylformamide (1 mL). The solution was heated at 100 °C for 15 minutes and then cooled to room temperature. $Zn(NO_3)_2 \cdot 6\ H_2O$ (0.024 mmol, 21.5 mg) was added to a separate glass vial and dissolved in methanol (1 mL). The methanol solution containing $Zn(NO_3)_2 \cdot 6\ H_2O$ was layered carefully onto the DMF solution so that two clear layers are visible. Concentrated HCl (40 µL) was dispensed into the layered mixture. The mixture was placed into an oven set at 80 °C, heated for one day, and then slowly cooled to room temperature. Red blocky crystals formed.

2D ZnBTATz (2). BTATz (0.012 mmol, 3 mg) was added to a glass vial and dissolved in dry *N*,*N*-dimethylformamide (1 mL). The solution was heated at 100 °C for 15 minutes and then cooled to room temperature. $Zn(NO_3)_2 \cdot 6\ H_2O$ (0.072 mmol, 7.19 mg) was added to a separate glass vial and dissolved in methanol (1 mL). The methanol solution containing $Zn(NO_3)_2 \cdot 6\ H_2O$ was layered carefully onto the DMF solution containing BTATz so that two layers are visible. Concentrated HCl (40 µL) was dispensed into the layered mixture. The mixture was placed into an oven set at 80 °C, heated for two days, and then slowly cooled to room temperature. Orange prismatic crystals formed.

Powder X-Ray diffraction. Powder patterns of 1D ZnBTATz and 2D ZnBTATz were collected with a Panalytical Empyrean using Cu-Kα radiation (λ = 1.54187 Å) and operating at 45 kV and 40 mA. The instrument is equipped with a Bragg-Brentano HD X-ray optic and an X'Celerator Scientific detector operating in continuous 1D scanning mode. Samples were prepared by pressing them onto a glass slide fitted into a sample holder to minimize height error. The patterns

were collected by scanning 2θ from 5° to 50° with a 0.02° step size and a step speed of 0.125 seconds. The data were processed using Jade 8 XRD Pattern Processing, Identification & Quantification analysis software (Materials Data, Inc.). The powder patterns were compared to respective simulated powder patterns from single crystal XRD structures available from the Cambridge Crystallographic Data Centre and were found to be in good agreement with the predicted patterns.

Thermogravimetric analysis. A TA Instruments Q50 TGA was used to obtain thermogravimetric data in which the analyte was heated from ~25 °C to 600 °C at a rate of 10 °C/min and analyzed in a platinum pan under flowing nitrogen.

Differential scanning calorimetry. Thermograms of each sample were recorded on a TA Instruments Q10 DSC. All experiments were run using a Tzero^{TM} DSC High Pressure Capsule Kit and studied under a nitrogen purge with a heating rate of 10 °C/min, covering the temperature range of ~25 °C to 350 °C. Calibration of the instrument was performed using an indium standard. Thermograms were analyzed using TA Universal Analysis 2000, V 4.5A. Samples were weighed prior to and after heating to ensure that not mass escaped the pan during analysis.

3.5 References:

1. S. Seth and A. J. Matzger, *Crystal Growth & Design*, 2017, **17**, 4043-4048.
2. G. R. Desiraju, J. J. Vittal and A. Ramanan, *Crystal Engineering: A Textbook*, World Scientific, 2011.
3. K. Koh, A. G. Wong-Foy and A. J. Matzger, *Angewandte Chemie International Edition*, 2008, **47**, 677-680.
4. K. Koh, A. G. Wong-Foy and A. J. Matzger, *Journal of the American Chemical Society*, 2009, **131**, 4184-4185.

5. S. Zhang, Q. Yang, X. Liu, X. Qu, Q. Wei, G. Xie, S. Chen and S. Gao, *Coordination Chemistry Reviews*, 2016, **307**, 292-312.
6. K. A. McDonald, S. Seth and A. J. Matzger, *Crystal Growth & Design*, 2015, **15**, 5963-5972.
7. M. Klapötke Thomas, *Chemistry of High-Energy Materials*, 2015.
8. J. Akhavan, *The chemistry of explosives*, Royal Society of Chemistry, 2004.
9. M. H. V. Huynh, M. A. Hiskey, T. J. Meyer and M. Wetzler, *Proceedings of the National Academy of Sciences*, 2006, **103**, 5409-5412.
10. T. M. Klapötke and N. Mehta, *Propellants, Explosives, Pyrotechnics*, 2014, **39**, 7-8.
11. N. Mehta, K. Oyler, G. Cheng, A. Shah, J. Marin and K. Yee, *Zeitschrift für anorganische und allgemeine Chemie*, 2014, **640**, 1309-1313.
12. M. A. S. Laidlaw, G. Filippelli, H. Mielke, B. Gulson and A. S. Ball, *Environmental Health*, 2017, **16**, 34.
13. Q. Zhang and J. n. M. Shreeve, *Angewandte Chemie International Edition*, 2014, **53**, 2540-2542.
14. S. Chen, B. Zhang, L. Yang, L. Wang and T. Zhang, *Dalton Transactions*, 2016, **45**, 16779-16783.
15. Y. Feng, Y. Bi, W. Zhao and T. Zhang, *Journal of Materials Chemistry A*, 2016, **4**, 7596-7600.
16. W. Gao, X. Liu, Z. Su, S. Zhang, Q. Yang, Q. Wei, S. Chen, G. Xie, X. Yang and S. Gao, *Journal of Materials Chemistry A*, 2014, **2**, 11958-11965.
17. X. Qu, S. Zhang, Q. Yang, Z. Su, Q. Wei, G. Xie and S. Chen, *New Journal of Chemistry*, 2015, **39**, 7849-7857.
18. C. Shen, Y. Liu, Z.-q. Zhu, Y.-g. Xu and M. Lu, *Chemical Communications*, 2017, **53**, 7489-7492.
19. M. A. Hiskey, N. Goldman and J. R. Stine, *Journal of Energetic Materials*, 1998, **16**, 119-127.
20. M. A. C. Hiskey, D.E.; Naud, D.L. , *Insensitive High-Nitrogen Compounds* LA-UR-01-1493, Los Alamos National Laboratory, 2001.
21. D. Chavez, M. Hiskey and D. L. Naud, *Tetrazine Explosives*, 2004.
22. D. E. Chavez and M. A. Hiskey, *Journal of Energetic Materials*, 1999, **17**, 357-377.

23. A. Saikia, R. Sivabalan, B. G. Polke, G. M. Gore, A. Singh, A. Subhananda Rao and A. K. Sikder, *Journal of Hazardous Materials*, 2009, **170**, 306-313.
24. L. Sun, S. Wei, Y. Zhang, L. Zhai, Q. Yang, Q. Wei, G. Xie, B. Wang and S. Chen, *ACS Applied Energy Materials*, 2018, **1**, 700-706.
25. J.-S. Qin, J.-C. Zhang, M. Zhang, D.-Y. Du, J. Li, Z.-M. Su, Y.-Y. Wang, S.-P. Pang, S.-H. Li and Y.-Q. Lan, *Advanced Science*, 2015, **2**, 1500150.
26. O. S. Bushuyev, P. Brown, A. Maiti, R. H. Gee, G. R. Peterson, B. L. Weeks and L. J. Hope-Weeks, *Journal of the American Chemical Society*, 2012, **134**, 1422-1425.
27. O. S. Bushuyev, G. R. Peterson, P. Brown, A. Maiti, R. H. Gee, B. L. Weeks and L. J. Hope-Weeks, *Chemistry – A European Journal*, 2012, **19**, 1706-1711.
28. P. Politzer and J. S. Murray, *Journal of Molecular Modeling*, 2015, **21**, 262.
29. S. Seth, K. A. McDonald and A. J. Matzger, *Inorganic Chemistry*, 2017, **56**, 10151-10154.
30. V. P. Sinditskii, V. Y. Egorshev, G. F. Rudakov, A. V. Burzhava, S. A. Filatov and L. D. Sang, *Thermochimica Acta*, 2012, **535**, 48-57.
31. B. Wang, W. Lai, Q. Liu, P. Lian and X. Yongqiang, *Synthesis, characterization and quantum chemistry study of 3,6-bis(1H-1,2,3,4-tetrazol-5-yl-amino)-1,2,4,5-tetrazine*, 2009.
32. X.-B. Zhang, Y.-H. Ren, W. Li, F.-Q. Zhao, J.-H. Yi, B.-Z. Wang and J.-R. Song, *Journal of Coordination Chemistry*, 2013, **66**, 2051-2064.
33. Q. Liu, B. Yang, J. Yang, Y. Ren, X. Zhang, H. Ma, K. Xu, F. Zhao and R. Hu, *Journal of Coordination Chemistry*, 2017, **70**, 2249-2260.
34. G. Steinhauser and T. M. Klapötke, *Angewandte Chemie International Edition*, 2008, **47**, 3330-3347.
35. R. V. Kent, R. A. Wiscons, P. Sharon, D. Grinstein, A. A. Frimer and A. J. Matzger, *Crystal Growth & Design*, 2018, **18**, 219-224.
36. K. B. Landenberger, O. Bolton and A. J. Matzger, *Journal of the American Chemical Society*, 2015, **137**, 5074-5079.

Chapter Four

Adsorption of Oxidant in Zeolitic Imidazolate Frameworks Yields Energetic Materials

4.1 Introduction

Metal−organic frameworks (MOFs) are a class of coordination polymers prepared by metal-mediated self-assembly of multitopic organic ligands, wherein metal-ligand bonds lead to 2-D or 3-D crystalline networks.[1] The porosity and structural stability of MOFs permits a host of applications including gas storage, separations, and catalysis.[2-11] Recently, several research groups have demonstrated the potential for MOFs to perform as explosives.[12-14] Explosives are a class of high-energy materials typically containing fuel and oxidizer that respond rapidly to stimuli by releasing large amounts of energy and gases. While metal-organic species have been used for many years as primary explosives (i.e. lead styphnate, lead azide, mercury fulminate), one of the major goals for the energetics field is to develop more eco-friendly (non-polluting or readily degradable in the environment) materials that exhibit performance comparable to widely used energetic materials.

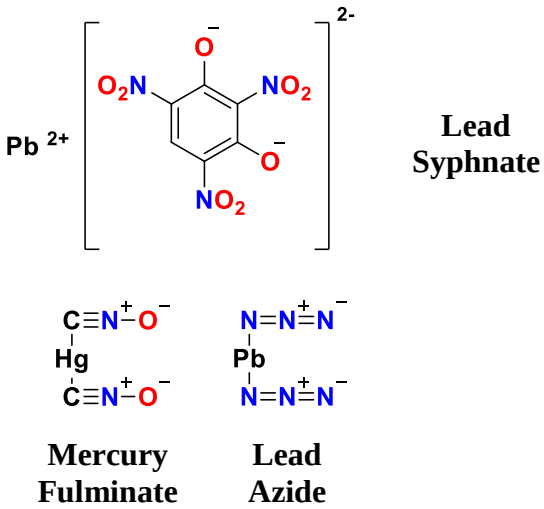

Figure 4.1 Chemical structures of known metal-organic compounds that are used as primary explosives including lead styphnate, lead azide, and mercury fulminate.

Many MOFs are constructed from non-toxic metals, and numerous reported energetic MOFs exhibit good thermal stability and promising performance.[15-23]

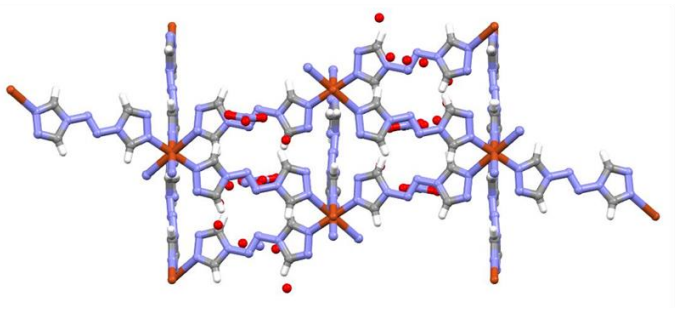

$Cu[(atrz)_3(NO_3)]_n$

Density (g cm^{-3}) = 1.68
Thermal decomposition (°C) = 243
Detonation velocity (km s^{-1})= 9.16
Detonation pressure (GPa)= 35.6

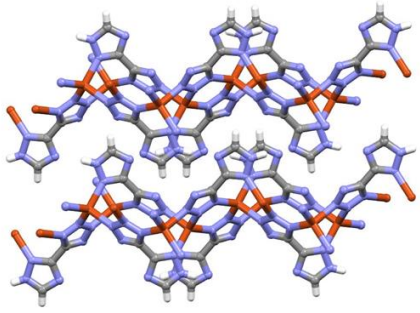

$Cu[(Htztr)]_n$

Density (g cm^{-3}) = 2.43
Thermal decomposition (°C) = 355
Detonation velocity (km s^{-1})= 10.4
Detonation pressure (GPa)= 56.4

Figure 4.2. Crystal structures and energetic performance properties of two representative energetic 3D MOFs consisting of high nitrogen ligands. $Cu[(atrz)_3(NO_3)]$ consists of 4,4'-azo-1,2,4-triazole ligands, copper metal ions and nitrate anions. $Cu[(Htztr)]_n$ consists of 3-(1*H*-tetrazol-5-yl)-1*H*-triazole and copper metal ions. Each structure exhibits promising energetic performance (detonation velocity and detonation pressure) determined by Kamlet-Jacobs equations.[38]

In contrast to many non-energetic MOFs, energetic MOFs generally lack permanent porosity therefore increasing oxygen content requires covalent modification of the ligand and this often impacts the structure making the purposeful design of energetic MOFs challenging. Recently, we demonstrated the utility of porous, 3-D MOFs loaded with over-oxidized guests as explosives.[24] A non-energetic, fuel-rich framework, MOF-5, was loaded with the energetic oxidizers tetranitromethane (TNM) and hexanitroethane (HNE). The fuel and oxidizer composites, MOF-5-TNM and MOF-5-HNE were highly energetic and exhibited high sensitivity to impact leading the materials to be classified as primary explosives. In contrast to secondary

explosives, primary explosives are more sensitive to stimuli and while this material property is desirable in some military and commercial devices such as blasting caps, detonators and primers,[25, 26] the most used energetic materials are relatively insensitive secondary explosives. Here oxidant adsorption into porous materials containing functionalized imidazole ligands was evaluated as a strategy to design a new class of energetic composite materials. To this end, zeolitic imidazolate frameworks (ZIFs) were employed in the adsorption of TNM to develop porous, explosive, composite materials with good impact sensitivity and thermal stability.

MOFs are often synthesized with carboxyl containing ligands wherein the carbonyl carbon is already oxidized and therefore the oxygen provided by this substituent does not add substantially to the overall heat released. The development of frameworks based on linkers with high atomic percentages of nitrogen is of particular interest relative to carboxylate based frameworks because, in addition to their energetic nature, nitrogen-rich ligands tend to exhibit good thermal stability. However, these new high-nitrogen MOFs lack sufficient oxygen content needed to fully convert all of the fuel atoms into neutral gaseous products (CO_2, H_2O, etc.), which indicates that some fuel is wasted during decomposition.

ZIFs are MOFs consisting of imidazolate linkers that bridge tetrahedral metal ions to form topologies similar to zeolites. ZIF-8,[27] also known as [{Zn-$(mim)_2$•$2H_2O$}][28] was chosen for initial studies because its properties are well known and it is commercially available as Basolite Z1200. ZIF-8 is an oxygen-free framework comprised of 2-methylimidazole ligands bridging Zn^{2+} ions to form a crystalline solid with sodalite (**sod**) topology. It has a surface area in excess of 1500 m^2/g and contains large, spherical pores with a diameter of 11.6 Å. Each pore is connected by a narrow (3.4 Å) window, which allows guests to enter the framework.[27]

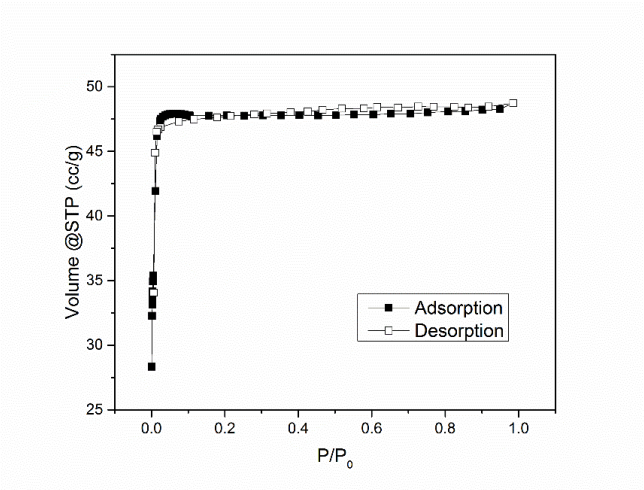

Figure 4.3 Evacuated ZIF-8 displays Type 1 isotherm behavior and has an apparent surface area of 1388 m^2/g (BET model).

Analysis of the solvent accessible volume was performed on guest free crystal structures of ZIF-8 (50%), and this calculation determines the percentage of the pore volume that is accessible to oxidant guests. We predict that the resulting composite material, ZIF-8-TNM, will be a better explosive than neat TNM because the composite will contain more fuel to react with the oxidant and produce a higher heat release than neat TNM.

4.2 ZIF-8-TNM Composite

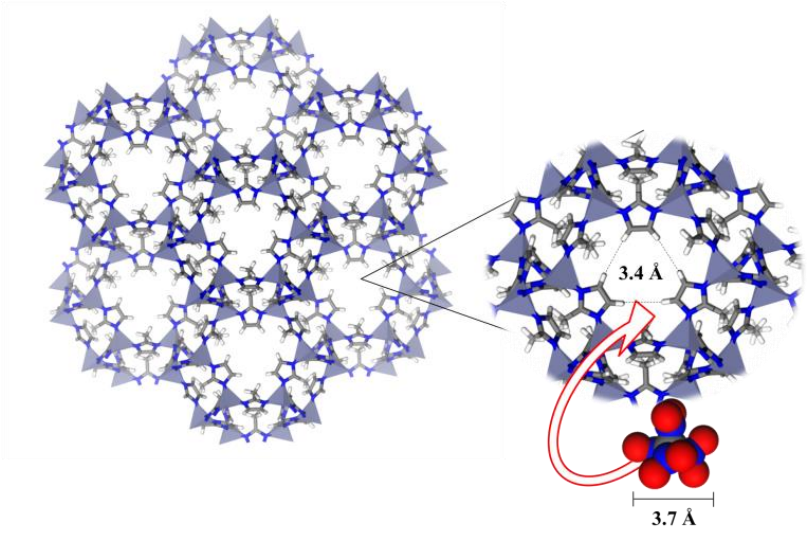

Figure 4.4 Crystal structure of ZIF-8 shown with pore aperture measurements to illustrate the size relative to tetranitromethane.

Oxidant adsorption in ZIF-8 was conducted by soaking crystals in neat TNM in a capped glass vial at 50 °C. Samples were withdrawn from the vial after a period of time and rinsed with cold pentane. The structural integrity of these crystals after oxidant adsorption was confirmed by powder X-ray diffraction (PXRD). Thermogravimetric analysis (TGA) and differential scanning calorimetry (DSC) were used to determine the weight percent of oxidant loading, as well as the thermal stability of the composite material.

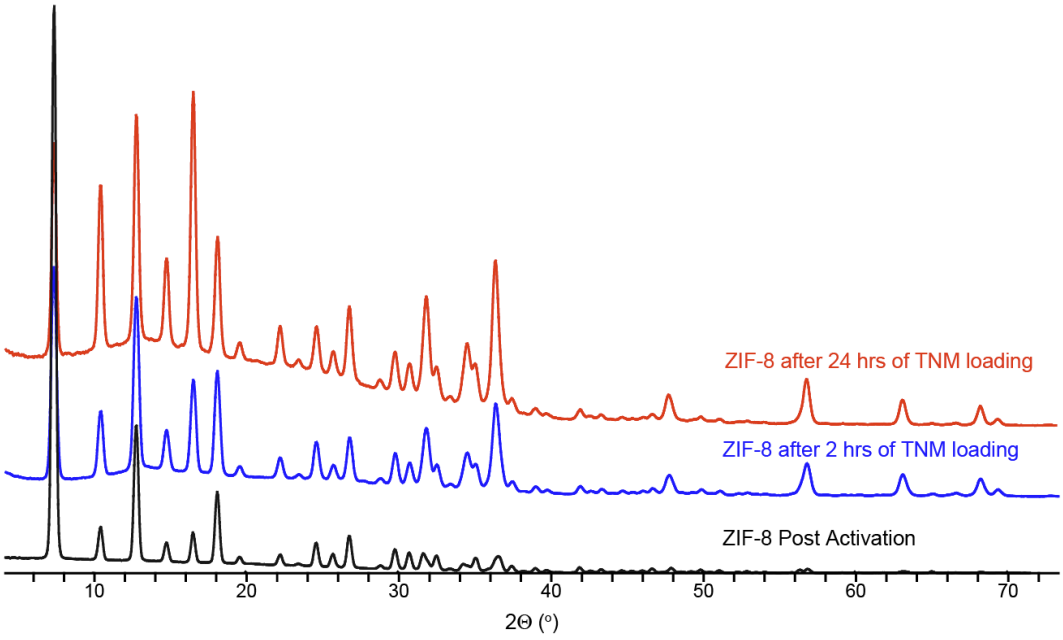

Figure 4.5 Powder X-Ray diffraction patterns collected to monitor the structural integrity of ZIF-8 during TNM loading at elevated temperatures: as synthesized ZIF-8 (black), ZIF-8-TNM after 2 hours (blue), ZIF-8-TNM after 24 hours (red).

TGA was performed with pristine ZIF-8 and this analysis reveals that decomposition of the framework begins around 400 °C. The ZIF-8-TNM composite material was also evaluated by TGA after 2, 4, and 6 hour incubation times. The composite exhibits an initial mass loss before 400 °C, which was not observed in the ZIF-8 thermal signature. Taken together, it can be assumed that the of the mass loss observed prior to 400 °C in the ZIF-8-TNM thermal signature can be attributed to TNM loss, which corresponds to >30 wt% TNM loading. Additionally, if this initial mass loss corresponds to stored TNM escaping the pores of ZIF-8 as temperature increases, then the total loading is somewhat underestimated due to some guest loss under ambient conditions. However, what is needed is a method to accurately quantify the loading of TNM into ZIF-8. This will be accomplished by performing a combined analysis of TGA/IR (infrared spectroscopy) on samples of ZIF-8-TNM, and comparing the thermogram/spectra to

standards of TNM, pristine ZIF-8, and 2-methylimidazole. The goal of this analysis is to confirm that the mass loss prior to 400 °C is TNM escaping the pores of ZIF-8 and to quantify the amount of TNM in the ZIF-8-TNM composite.

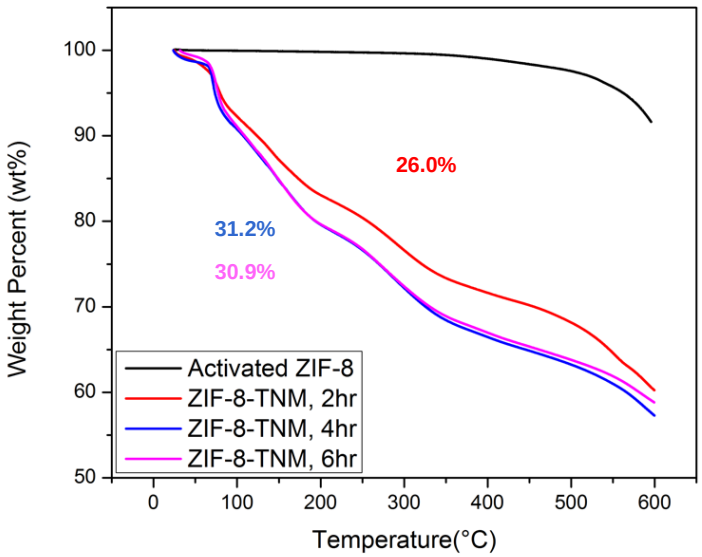

Figure 4.6 Release of TNM from ZIF-8 at different time points reveals that ZIF-8 reaches saturation after adsorbing 31 wt% of oxidant in 4 hours.

DSC measurements were collected at 50 °C/min ramp rate on ZIF-8-TNM crystals and two broad exothermic peaks were observed indicating that separate exothermic transitions occur. The first exothermic event corresponds to composite decomposition, followed by decomposition of the TNM that escapes from the ZIF as temperature increases. Since some TNM escapes from the ZIF-8 pores prior to exothermic reaction, not all of the oxidant is able to fully react with ZIF-8. To circumvent this problem, a portion of neat TNM was added to the DSC pan containing ZIF-8-TNM crystals to suppress escape of oxidant guests from the pores. The resulting DSC thermal curve displays a single exothermic transition occurring at 175 °C indicating that ZIF-8-TNM can be thermally initiated. These measurements were performed in a high-pressure pan to ensure that

no product gases escape so that the experimental heat release (ΔH) during decomposition of ZIF-8-TNM can be quantified. The ΔH for this exothermic event is 5.63 kJ/g, when using a 1:1.1 mass ratio of ZIF-8-TNM to excess TNM, which is more than four times the heat release from neat TNM. To further characterize the ZIF-8-TNM material the overall composite density was calculated based on the weight percent of the absorbed oxidant observed by the initial mass loss prior to ZIF decomposition in TGA, as well as the density of the framework, and after 4 hours (assuming 31.2 wt% loading) the composite material has a density of 1.43 g/cm^3.

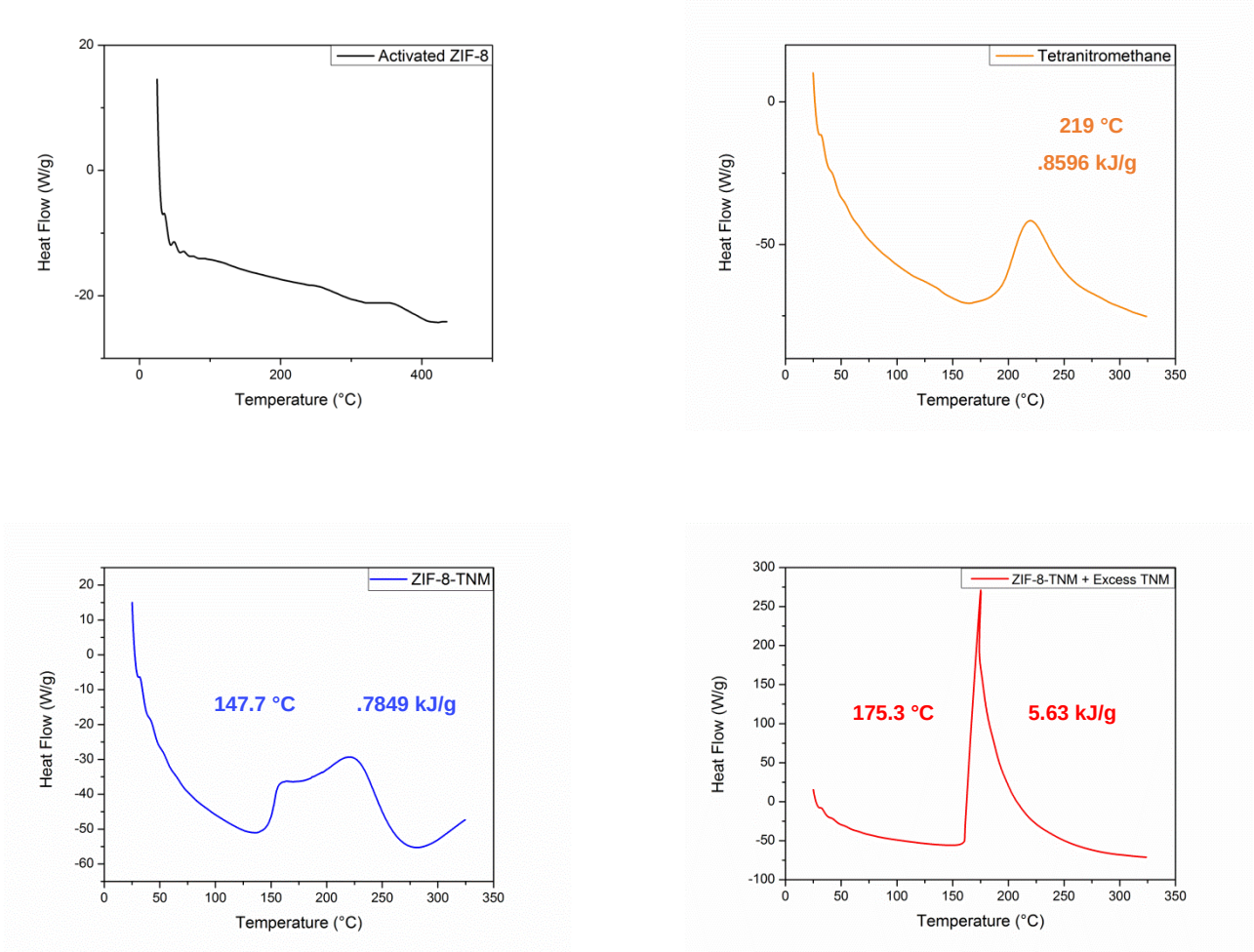

Figure 4.7 DSC thermograms of activated ZIF-8 collected at 50 °C min^{-1} shows no phase changes occurring up to 450 °C, TNM (1.945 mg), ZIF-8-TNM composite (2.889 mg), and ZIF-8-TNM composite (0.802 mg) + excess TNM (0.941) collected at 50 °C min^{-1} in high pressure pans to contain prevent the release of product gases.

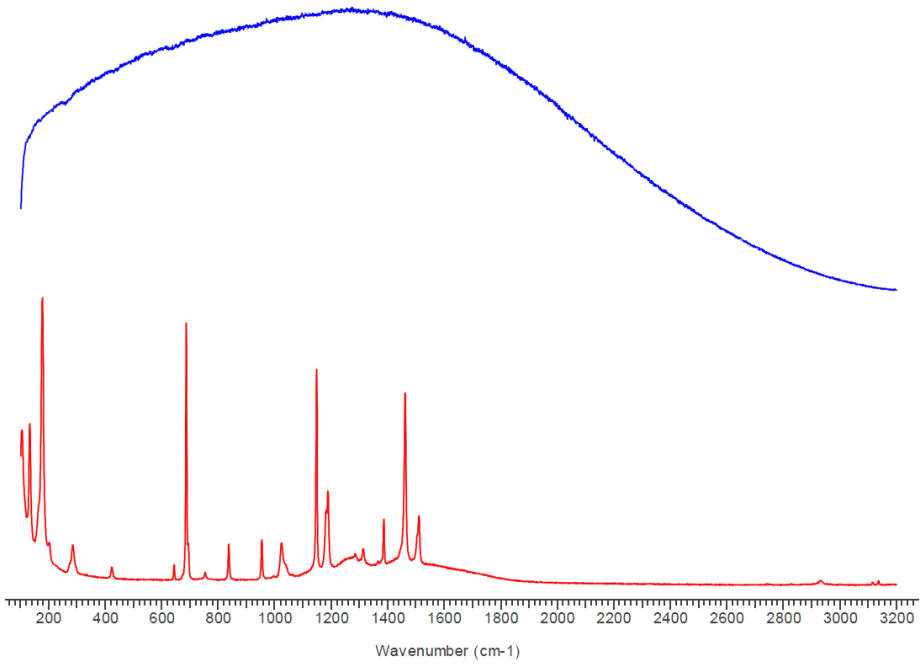

Figure 4.8 Raman spectra of as-synthesized ZIF-8 (red) and the decomposition product of ZIF-8-TNM (blue) after thermal initiation showing the conversion of ZIF-8-TNM to carbon soot.

Oxygen balance is a term used to describe the theoretical amount of oxygen required to completely convert fuel atoms (carbon, hydrogen, sulfur and metals) into neutral, molecular components. The ideal oxygen balance for an energetic material is 0% which means that the material has sufficient oxygen for complete oxidation and no fuel is wasted. Pristine ZIF-8 is non-explosive, contains no oxygen within the framework and has an oxygen balance of -155%. Upon maximum loading with TNM the oxygen balance of the composite becomes more neutral changing to -91%. Although significant improvement in the oxygen balance of ZIF-8-TNM as compared to ZIF-8 was achieved, more neutral oxygen balances are typically characteristic of explosives (vide infra). A solution to this problem would be oxidant adsorption into a ZIF with higher porosity for increased loading and a more neutral oxygen balance for the unloaded

framework. ZIF-70 meets these requirements.

4.3 ZIF-70-TNM Composite

ZIF-70 is a mixed linker[29-32] material comprised of 2-nitroimidazole and imidazole, and has a reported surface area of greater than 1700 m^2/g. This structure has a gmelinite (**gme**) topology and features wide channels with a diameter of 15.9 Å and large pore windows (13.1 $Å^3$).

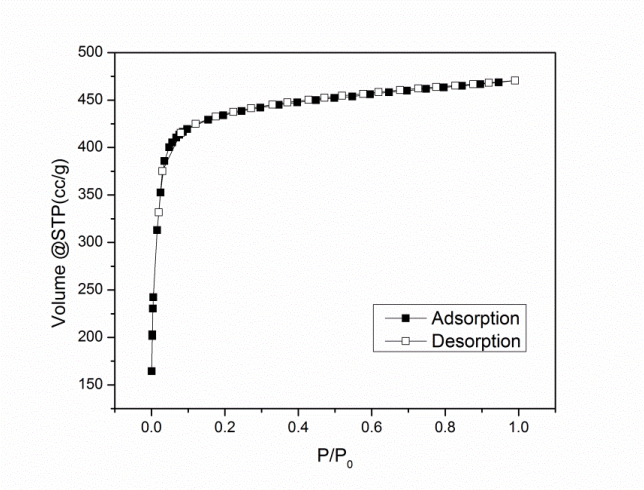

Figure 4.9 Evacuated ZIF-70 displays Type 1 isotherm behavior and has an apparent surface area of 1776 m^2/g (BET model).

In ZIF-70 the nitro substituent is significant because it provides oxidizing power for the fuel rich framework, as opposed to the oxygen free ZIF-8. The resulting oxygen balance of pristine ZIF-70 (-92%) is inherently more neutral than ZIF-8. Analysis of the solvent accessible volume was performed on the guest free crystal structure of ZIF-70 (54%) and given these features we predict that ZIF-70-TNM will possess a more neutral oxygen balance than ZIF-8-TNM.

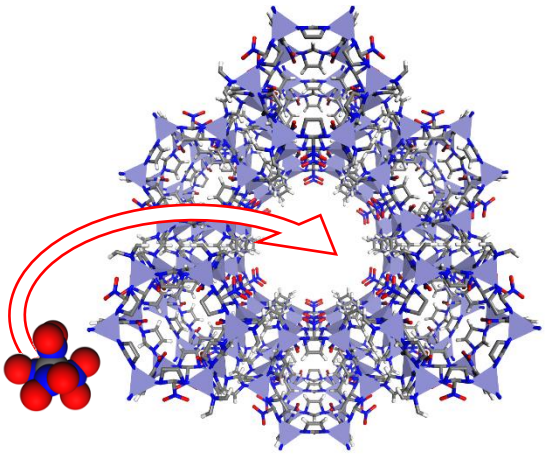

Figure 4.10 Crystal structure of ZIF-70 displaying large channels capable of capture and storage of more oxidant guests than ZIF-8.

To determine maximum achievable oxidant adsorption in ZIF-70, the material was first loaded with TNM using the neat loading method. Unexpectedly, this method resulted in a loss of long range order of the bulk material as evidenced by the emergence of an amorphous phase observed in PXRD. As a more mild alternative approach, TNM was adsorbed into porous ZIF-70 crystals by vapor diffusion at room temperature.

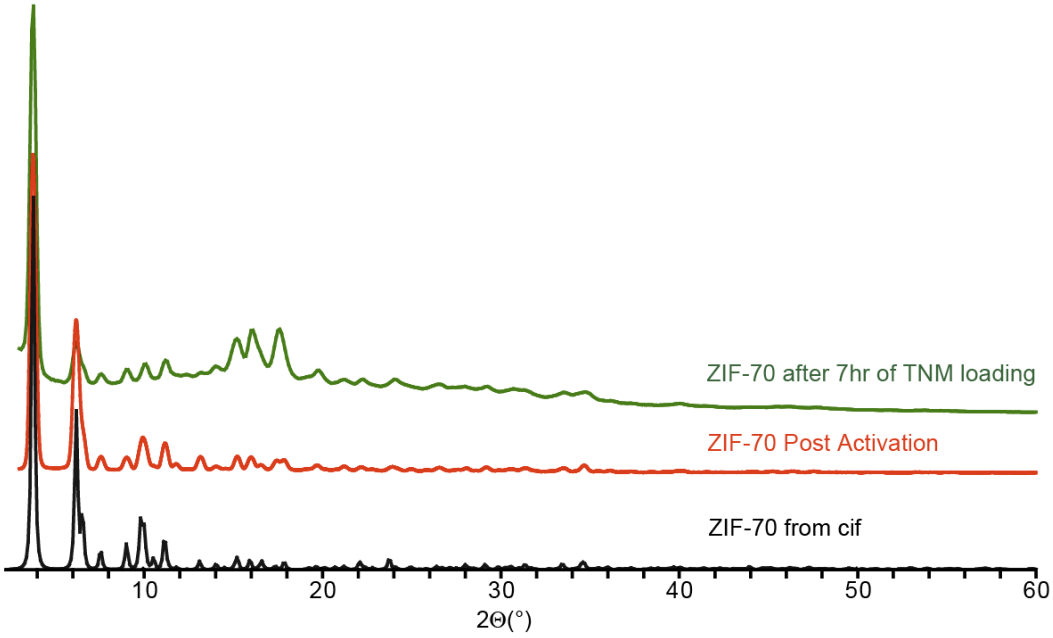

Figure 4.11 Powder X-Ray diffraction patterns collected to monitor the structural integrity of ZIF-70 during TNM loading at room temperature: simulated ZIF-70 pattern (black), as synthesized ZIF-70-TNM (red), ZIF-70-TNM after 7 hours (green).

Adsorption of TNM into ZIF-70 was monitored and quantified by TGA after 30 minutes, 1, 2, and 3 hours until the ZIF-70-TNM composite reached maximum adsorption wherein 46.2 wt% of the composite is TNM adsorbed into ZIF-70 (Figure 3). ZIF-70 has a larger pore volume than ZIF-8 therefore it is capable of storing more oxidant guests within the framework. The loading of TNM into ZIF-70 up to 46.2 wt.% corresponds to a composite material density of 1.53 g/cm^3.

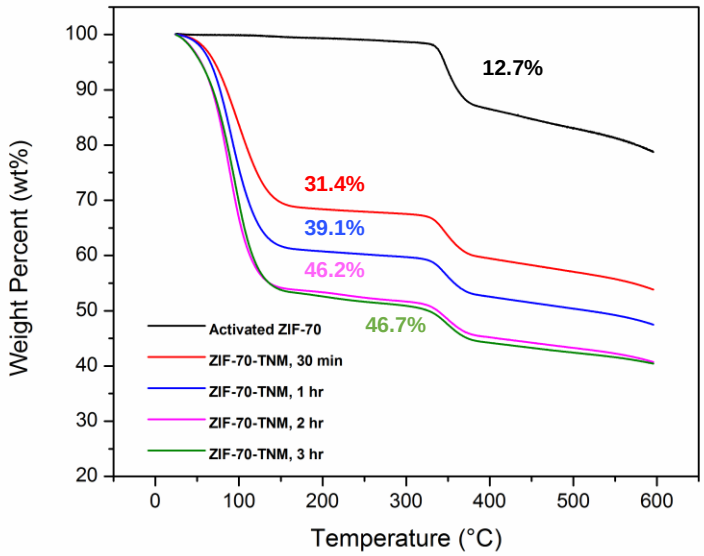

Figure 4.12 Release of TNM from ZIF-70 at different time points shows ZIF-70 reaches saturation after 46.2 wt% of oxidant is adsorbed into the pores.

Thermal analysis of the ZIF-70-TNM composite by DSC reveals two broad exothermic events. This behavior is similar to the ZIF-8-TNM composite. Additional neat TNM was placed into the DSC pan with ZIF-70-TNM, and upon heating the material exhibits a single exothermic transition at 158 °C with 6.00 kJ/g of energy released, when the ratio of ZIF-70-TNM to excess TNM is 1:1. For reference, a DSC measurement of activated ZIF-70 collected at 50 °C/min displays an exothermic event at 371 °C which corresponds to 1.40 kJ/g of energy released; this confirms that the nitro substituents provide some of the oxygen needed for oxidation of the framework. Collectively these results demonstrate that not only is the energy release improved by incorporation of nitrated linkers, but also the nitro group can lead to more thermally sensitive composite materials as well. The saturation of ZIF-70 with TNM at 46.2 wt.% corresponds to an oxygen balance of -27.2% for the composite, which is significantly more neutral than the industry standard TNT (-73.9%) and approaching HMX (-21.6%).

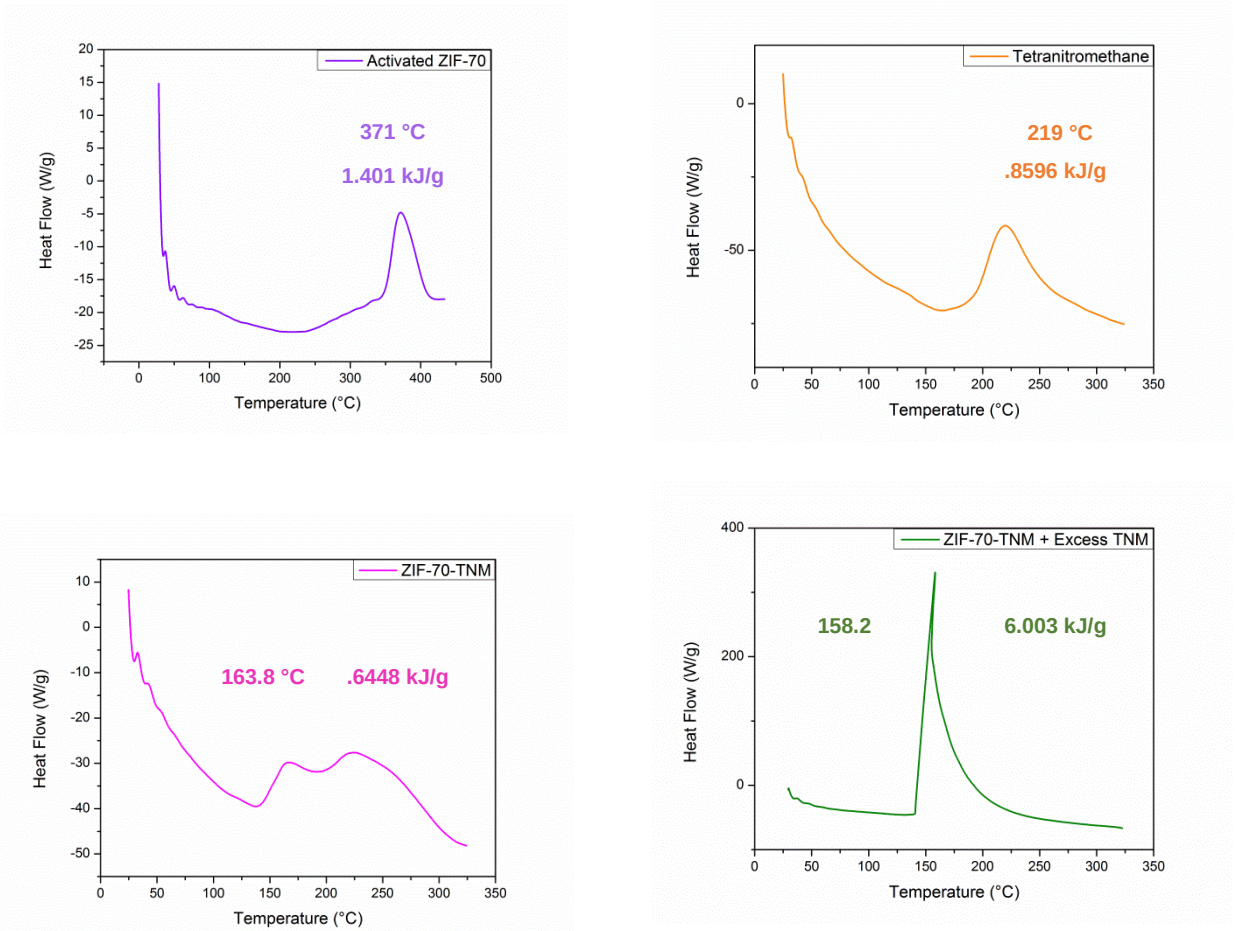

Figure 4.13 DSC thermogram of ZIF-70 collected at 50 °C min^{-1}in a aluminum hermetic pan displays an exothermic event at 371 °C with energy release that equals 1401 J/g. TNM (1.945 mg), ZIF-70-TNM (1.373 mg), and ZIF-70-TNM (0.814mg) + excess TNM (0.812mg) were collected at 50 °C min^{-1} in high pressure pans to contain prevent the release of product gases.

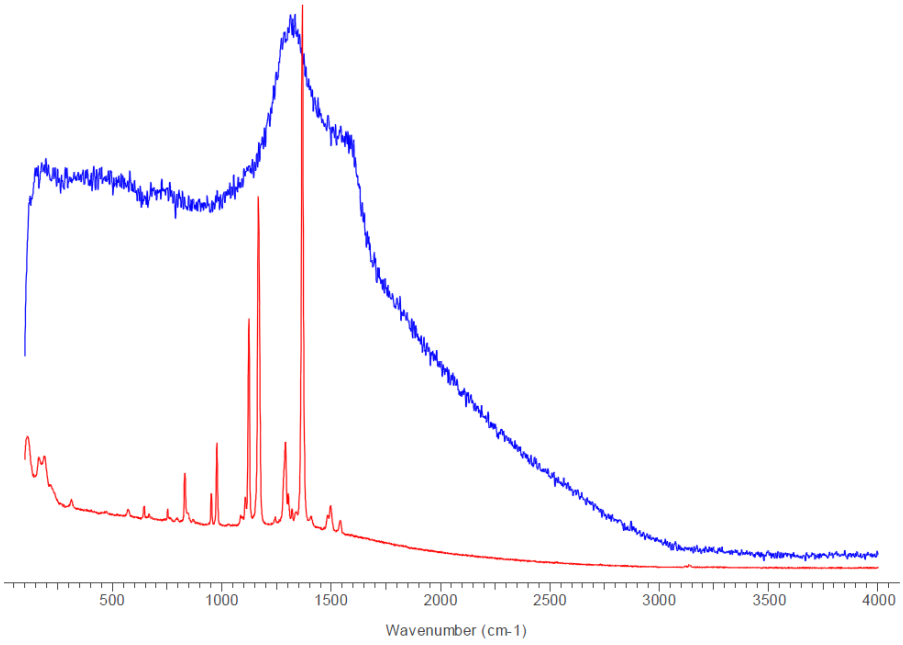

Figure 4.14 Raman spectra of as-synthesized ZIF-70 (red) and the decomposition product of ZIF-70-TNM (blue) after thermal initiation showing conversion of ZIF-70-TNM to carbon soot.

Table 4.1 Thermal and physical properties of the oxidant, non-energetic frameworks, energetic composites and reference secondary energetic materials.

	Oxygen Balance (%)	**Density (g/cm^3)**	**DSC $_{decomp.}$ (°c)**	**ΔH (kJ/g)**
TNM	48.9	1.62	219	0.859
ZIF-8	-155	0.925	>500	-
ZIF-8-TNM	-91.1	1.43	175	5.63
ZIF-70	-92.7	0.777	371	1.40
ZIF-70-TNM	-27.2	1.53	158	6.00
MONOCLINIC TNT[33]	-74.0	1.65	298	1.70
PETN[34]	-10.0	1.85	207	-
δ-HMX[35]	-21.6	1.76	279	-

Energy and sensitivity are two important parameters of energetic materials and often these two properties are in direct conflict with each other because high energy materials tend to be more sensitive to stimuli.[36] Sensitivity tests are used to evaluate the safe handling requirements for energetic materials and to determine their probability of initiation under a given set of conditions. Small scale impact sensitivity tests were performed to determine the drop height required to attain a 50% probability of a positive response (dH_{50}). These measurements help to determine the conditions under which ZIF-8-TNM and ZIF-70-TNM may be safely handled and to demonstrate how the adsorption of oxidant guests influence the impact sensitivity of ZIF-8 and ZIF-70. The dH_{50} values of ZIF-8-TNM and ZIF-70-TNM were determined using the Bruceton up-down technique wherein a 5 lb. weight is allowed to freefall from pre-measured distances onto a non-hermetic DSC pan. On this particular apparatus,[37] TNM exhibits a dH_{50} of 34 cm, whereas ZIF-8-TNM and ZIF-70-TNM exhibit dH_{50} values of 36 cm and 17 cm, respectively. This would classify these materials as secondary explosives which typically require a primary explosive for initiation based on the impact sensitivity greater than the reported PETN drop height. [34]

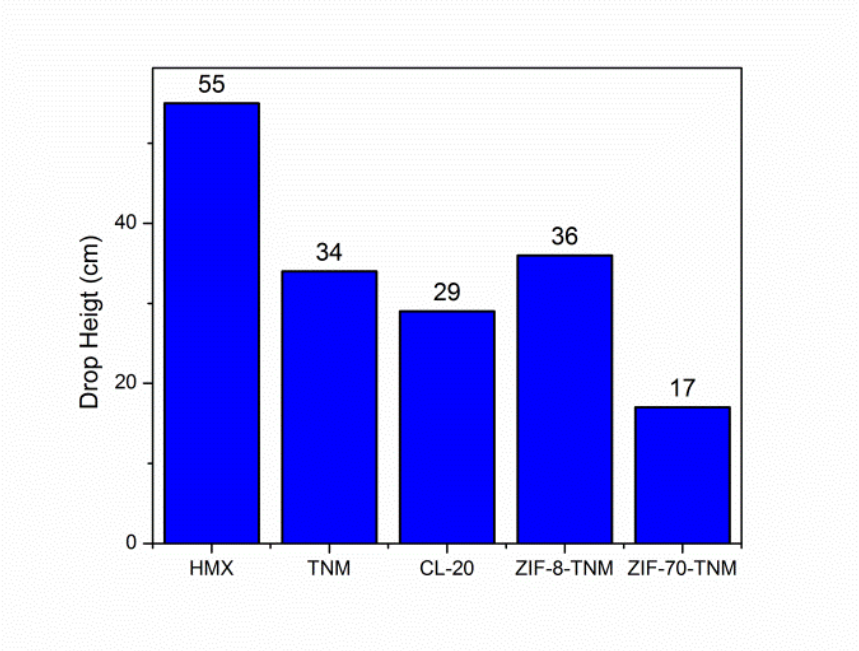

Figure 4.15 The dH_{50} values of known explosive materials with the explosive ZIF composites.

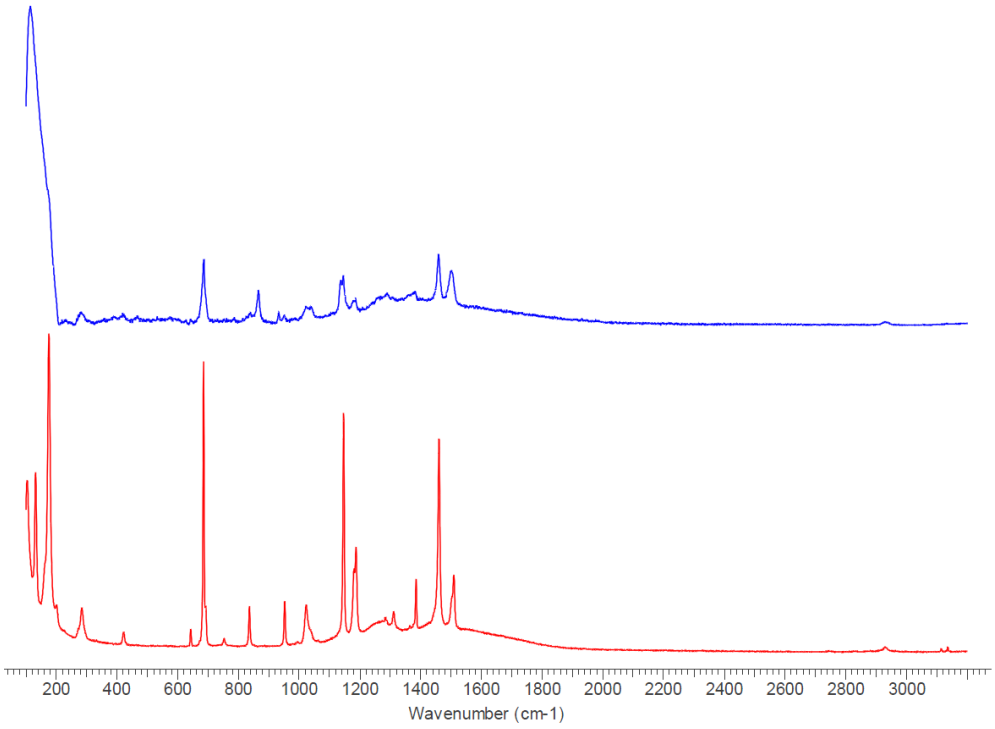

Figure 4.16 Raman spectra of as synthesized ZIF-8 (red) and the decomposition product of ZIF-8-TNM (blue) after impact initiation.

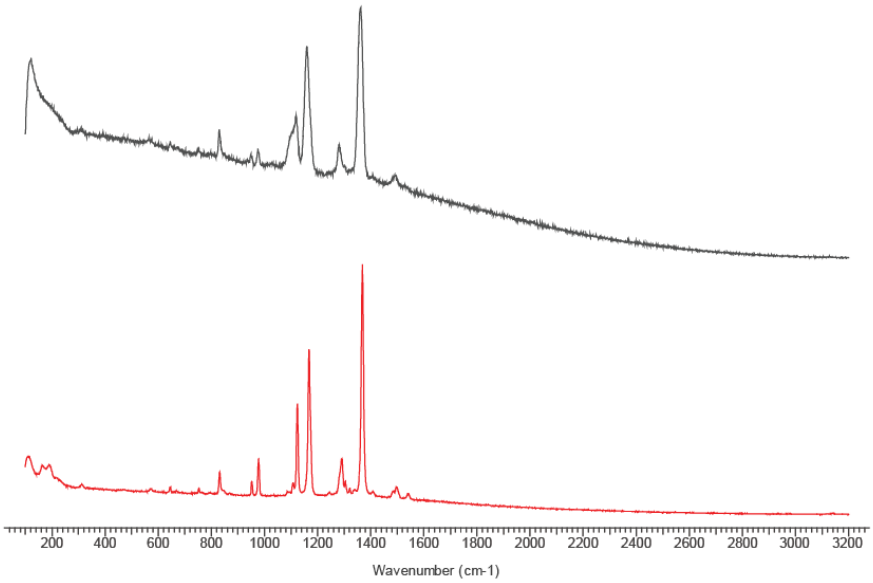

Figure 4.17 Raman spectra of as-synthesized ZIF-70 (red) and the decomposition product of ZIF-70-TNM (black) after impact initiation.

The development of new energetic materials is ultimately motivated by the drive for improved performance at a given cost and sensitivity; prediction of energetic performance including detonation velocity and detonation pressure is most typically carried out through computation. There are established methods for the prediction of energetic performance including the Kamlett-Jacobs (K-J) equations[38] and modern thermochemical software typified by Cheetah[39] However, each method has restrictions. For example, K-J equations were developed in 1968 for high-energy density compounds containing only hydrogen, carbon, nitrogen and oxygen and these equations are difficult to apply to modern explosives that contain metal ions. On the other hand, Cheetah thermochemical code can predict the performance of metal containing explosives, but only if the standard molar enthalpy of formation (ΔHf) of the material has been determined. The energetic performance parameters for ZIF-8-TNM were predicted using Cheetah because the heat of formation of both the framework and oxidant (TNM) is known. ZIF-

8-TNM has a predicted detonation velocity (Vd) of 4.40 km/s and a detonation pressure (P) of 6.56 GPa.

The standard molar enthalpy of formation of porous ZIF-70 was determined by oxygen bomb combustion calorimetry. Because the composition of ZIF-70 is somewhat variable (in the ratio of imidazole to 2-nitroimidazole), the composition of ZIF-70 was determined by 1H-NMR analysis wherein the metal organic framework was digested in a solution of DCl/D2O. The ratio of imidazole to nitroimidazole in as-synthesized ZIF-70 was determined as 2.05:1, in comparison to the literature reported ratio of 1.29:1 imidazole to nitroimidazole. That indicates an empirical formula of $ZnC_9H_{11}N_7O_2$ for our ZIF-70. The combustion reaction of ZIF-70 is presented in equation 1.

$$ZnC_6H_{5.344}N_{4.656}O_{1.312}(s) + 7.18\ O_2(g) \longrightarrow ZnO(s) + 6\ CO_2(g) + 2.672\ H_2O(l) + 2.328\ N_2(g) \quad \text{(eq. 1)}$$

$$\frac{\Delta T(^{\circ}C)\text{- } C_{cal}(\frac{J}{^{\circ}C}) - \text{Resisitive Heating(J)-NiCr burned } \left(\frac{J}{mg}\right) * \text{Mass burned wire(mg)}}{\text{Mass of sample(mg)} * \text{MW } (\frac{g}{mol})} \quad \text{(eq. 2)}$$

The average experimental value of three single measurements for the molar internal energy change of combustion $(\Delta U_{m,comb})$ was calculated with equation 2 and this value is $3.55*10^3$ kJ•mol^{-1} for ZIF-70.

$$\Delta H_{m,comb} = \Delta U_{m,comb} + \Delta n_g RT \quad \text{(eq. 3)}$$

Where Δn_g is the number of moles of product gas - number of moles of reactant gas, R=8.314 J•mol^{-1}•K^{-1}, T=298.15 K.[40]

The molar enthalpy of combustion is obtained by equation 3 which was calculated to be -3551.2 kJ•mol^{-1} for ZIF-70. Finally, the standard enthalpy of formation is calculated on the basis of

Hess law and the known enthalpies of formation of products ZnO(s), CO2(l), and H2O(l) by equation 4; the standard enthalpy of formation of ZIF-70 is +76.0 kJ•mol^{-1}.

$$\Delta H_f^\circ(\text{ZIF-70}) = \Sigma \Delta H_f^\circ(\text{products}) - \Delta H_{m,comb}(\text{ZIF-70}) \quad \text{(eq.4)}$$

$$\Delta H_f^\circ(ZnC_6H_{5.344}N_{4.656}O_{1.312}(s)) = \Delta H_f^\circ(ZnO(s)) + 6\Delta H_f^\circ(CO_2(g)) + 2.762\Delta H_f^\circ(H_2O(l)) - \Delta H_{m,comb}(ZnC_6H_{5.344}N_{4.656}O_{1.312}(s)) \quad \text{(eq.5)}$$

Accompanied by the standard molar enthalpy of formation, detonation parameters of ZIF-70-TNM including detonation velocity and detonation pressure can be extracted via Cheetah calculation.

4.4 Conclusions

The development of eco-friendly energetic materials that strike a balance between good performance and sensitivity is currently one of the main goals of the energetics field. Oxidant adsorption is a straightforward and facile strategy to produce energetic materials by leveraging porous metal-organic structures, ZIF-8 and ZIF-70, as fuel in an intimate mixture with oxygen rich TNM guests. The resultant composite structures, ZIF-8-TNM and ZIF-70-TNM, exhibit low impact sensitivity and large heat release upon decomposition which leads to their classification as secondary explosive materials. These energetic properties are the result of the inclusion of nitrogen containing imidazolate ligands in the framework and the replacement of the metal carboxylate coordination with metal nitrogen coordination. Structural features within ZIF-70 including large pores and nitroimidazole ligands led to a promising composite material that exhibits a desirable oxygen balance (-27.2%) approaching that of commercially relevant octogen (HMX). This work can be extended to other porous metal-organic structures with the uptake and storage of solid explosive guests like secondary explosive TNT for example. Uptake of solid explosives would circumvent the loss of volatile guests and yield high-performing composites.

4.5 Experimental Methods

Synthesis of ZIF-8. ZIF-8 was synthesized and activated using methods previously reported in literature[1] and stored in a nitrogen glovebox. The surface area of the material was confirmed by N_2 adsorption.

Synthesis of ZIF-70. ZIF-70 was synthesized and activated using methods previously reported in literature[2] and stored in a nitrogen glovebox. The surface area of the material was confirmed by N_2 adsorption.

ZIF-8-TNM. To absorb TNM, 10.0 mg of ZIF-8 was weighed into a 4 mL vial in an N_2 filled glove box. The sample was then removed from the glove box and 0.2 mL of TNM was added directly to the vial containing ZIF-8 crystals at room temperature. The 4 mL vial containing ZIF-8 and TNM was placed on a heat block set at 50 °C. TNM was allowed to absorb into ZIF-8. To stop the adsorption, the 4 mL vial containing ZIF-8-TNM was removed from the heat block, the crystals were vacuum filtered and rinsed with cold pentane.

ZIF-70-TNM. To absorb TNM, 10.0 mg of ZIF-70 was weighed into a 4 mL vial in an N_2 filled glove box. The sample was then removed from the glove box and 0.2 mL of TNM was added to a 20 mL glass vial. The 4 mL vial containing ZIF-70 was then inserted into the 20 mL glass vial containing ZIF-70 and capped. TNM was allowed to vaporize, come to equilibrium and absorb into ZIF-70. To stop the adsorption, the 4 mL vial containing ZIF-70-TNM was removed from the system and capped.

Powder X-Ray diffraction. Powder patterns of ZIF-8, ZIF-70, ZIF-8-TNM and ZIF-70-TNM were collected with a Panalytical Empyrean using Cu-Kα radiation (λ = 1.54187 Å) and operating at 45 kV and 40 mA. The instrument is equipped with a Bragg-Brentano HD X-ray

optic and an X'Celerator Scientific detector operating in continuous 1D scanning mode. Samples were prepared by pressing them onto a glass slide fitted into a sample holder to minimize height error. The patterns were collected by scanning 2θ from 5° to 50° with a 0.02° step size and a step speed of 0.125 seconds. The data were processed using Jade 8 XRD Pattern Processing, Identification & Quantification analysis software (Materials Data, Inc.). The powder patterns were compared to respective simulated powder patterns from single crystal XRD structures available from the Cambridge Crystallographic Data Centre and were found to be in good agreement with the predicted patterns.

Gas sorption measurements. Sorption experiments were carried out using a NOVA - series 4200 surface area analyzer (Quantachrome Instruments, Boynton Beach, Florida, USA). N_2 (99.999%) was purchased from Cryogenic Gases and used as received. For N_2 measurements, a glass sample cell was charged with ~50 to 100 mg of sample and analyzed at 77 K. Sorption isotherms were collected in the NOVAwin software.

Thermogravimetric analysis. A TA Instruments Q50 TGA was used to obtain thermogravimetric data in which the analyte was heated from ~25 °C to 600 °C at a rate of 10 °C/min and analyzed in a platinum pan under flowing nitrogen.

Differential scanning calorimetry. Thermograms of each sample were recorded on a TA Instruments Q10 DSC. All experiments were run using a Tzero^{TM} DSC High Pressure Capsule Kit and studied under a nitrogen purge with a heating rate of 50 °C/min, covering the temperature range of ~25 °C to 350 °C. Calibration of the instrument was performed using an indium standard. Thermograms were analyzed using TA Universal Analysis 2000, V 4.5A.

Samples were weighed prior to and after heating to ensure that no mass escaped the pan during analysis.

Raman spectroscopy. Raman spectra were obtained using a Renishaw inVia Raman microscope equipped with a CCD detector, 785 nm laser, 1200 lines/mm grating, and 65 μm slit used for collecting data. Spectra were collected using static scan mode and analyzed using the Wire 4.2 software package. Calibration of the instrument was performed using a silicon standard for all experiments.

Oxygen bomb calorimetry. The combustion energy of ZIF-70 was determined with a constant volume Parr 6200 isoperibol calorimeter fitted with a 1109X high strength semimicro oxygen combustion vessel. This vessel is suitable for testing energetic materials and is optimized for the measurement of small energy releases. Distilled water was used to fill the bucket and NiCr wire was used to ignite each sample, approximately 10 cm per test. Calibration of the instrument was performed by combustion of certified calorific grade benzoic acid pellets in an oxygen atmosphere at a pressure of 29 bar. Approximately 100 mg of as-synthesized ZIF-70 was ground into a powder in an N_2 filled glovebox. The samples were removed from the glovebox and pressed using a Parr pellet press to form a pellet. The reported data are the average of 3 single measurements.

4.6 References

1. S. Seth and A. J. Matzger, *Crystal Growth & Design*, 2017, **17**, 4043-4048.
2. Y.-S. Bae and R. Q. Snurr, *Angewandte Chemie International Edition*, 2011, **50**, 11586-11596.
3. L. E. Kreno, K. Leong, O. K. Farha, M. Allendorf, R. P. Van Duyne and J. T. Hupp, *Chemical Reviews*, 2012, **112**, 1105-1125.

4. S. S. Nagarkar, B. Joarder, A. K. Chaudhari, S. Mukherjee and S. K. Ghosh, *Angewandte Chemie International Edition*, 2013, **52**, 2881-2885.

5. A. Phan, C. J. Doonan, F. J. Uribe-Romo, C. B. Knobler, M. O'Keeffe and O. M. Yaghi, *Accounts of Chemical Research*, 2010, **43**, 58-67.

6. B. R. Pimentel, A. Parulkar, E. k. Zhou, N. A. Brunelli and R. P. Lively, *ChemSusChem*, 2014, **7**, 3202-3240.

7. P. B. R., P. Aamena, Z. Er-kang, B. N. A. and L. R. P., *ChemSusChem*, 2014, **7**, 3202-3240.

8. K. Shen, X. Chen, J. Chen and Y. Li, *ACS Catalysis*, 2016, **6**, 5887-5903.

9. U. P. N. Tran, K. K. A. Le and N. T. S. Phan, *ACS Catalysis*, 2011, **1**, 120-127.

10. C. Wang, D. Liu and W. Lin, *Journal of the American Chemical Society*, 2013, **135**, 13222-13234.

11. K. Zhang, R. P. Lively, C. Zhang, R. R. Chance, W. J. Koros, D. S. Sholl and S. Nair, *The Journal of Physical Chemistry Letters*, 2013, **4**, 3618-3622.

12. O. S. Bushuyev, G. R. Peterson, P. Brown, A. Maiti, R. H. Gee, B. L. Weeks and L. J. Hope- Weeks, *Chemistry – A European Journal*, 2013, **19**, 1706-1711.

13. K. A. McDonald, S. Seth and A. J. Matzger, *Crystal Growth & Design*, 2015, **15**, 5963-5972.

14. S. Zhang, Q. Yang, X. Liu, X. Qu, Q. Wei, G. Xie, S. Chen and S. Gao, *Coordination Chemistry Reviews*, 2016, **307**, 292-312.

15. Y. Feng, Y. Bi, W. Zhao and T. Zhang, *Journal of Materials Chemistry A*, 2016, **4**, 7596-7600.

16. W. Gao, X. Liu, Z. Su, S. Zhang, Q. Yang, Q. Wei, S. Chen, G. Xie, X. Yang and S. Gao, *Journal of Materials Chemistry A*, 2014, **2**, 11958-11965.

17. S. Li, Y. Wang, C. Qi, X. Zhao, J. Zhang, S. Zhang and S. Pang, *Angewandte Chemie International Edition*, 2013, **52**, 14031-14035.

18. X. Liu, W. Gao, P. Sun, Z. Su, S. Chen, Q. Wei, G. Xie and S. Gao, *Green Chemistry*, 2015, **17**, 831-836.

19. J.-S. Qin, J.-C. Zhang, M. Zhang, D.-Y. Du, J. Li, Z.-M. Su, Y.-Y. Wang, S.-P. Pang, S.-H. Li and Y.-Q. Lan, *Advanced Science*, 2015, **2**, 1500150.

20. X. Qu, L. Zhai, B. Wang, Q. Wei, G. Xie, S. Chen and S. Gao, *Dalton Transactions*, 2016, **45**, 17304-17311.

21. S. Seth, K. A. McDonald and A. J. Matzger, *Inorganic Chemistry*, 2017, **56**, 10151-10154.

22. C. Shen, Y. Liu, Z.-q. Zhu, Y.-g. Xu and M. Lu, *Chemical Communications*, 2017, **53**, 7489-7492.

23. Y. Zhang, S. Zhang, L. Sun, Q. Yang, J. Han, Q. Wei, G. Xie, S. Chen and S. Gao, *Chemical Communications*, 2017, **53**, 3034-3037.

24. K. A. McDonald, J. C. Bennion, A. K. Leone and A. J. Matzger, *Chemical Communications*, 2016, **52**, 10862-10865.

25. T. M. Klapötke and N. Mehta, *Propellants, Explosives, Pyrotechnics*, 2014, **39**, 7-8.

26. N. Mehta, K. Oyler, G. Cheng, A. Shah, J. Marin and K. Yee, *Zeitschrift für anorganische und allgemeine Chemie*, 2014, **640**, 1309-1313.

27. K. S. Park, Z. Ni, A. P. Côté, J. Y. Choi, R. Huang, F. J. Uribe-Romo, H. K. Chae, M. O'Keeffe and O. M. Yaghi, *Proceedings of the National Academy of Sciences*, 2006, **103**, 10186-10191.

28. X. C. Huang, Y. Y. Lin, J. P. Zhang and X. M. Chen, *Angewandte Chemie International Edition*, 2006, **45**, 1557-1559.

29. R. Banerjee, H. Furukawa, D. Britt, C. Knobler, M. O'Keeffe and O. M. Yaghi, *Journal of the American Chemical Society*, 2009, **131**, 3875-3877.

30. R. Banerjee, A. Phan, B. Wang, C. Knobler, H. Furukawa, M. O'Keeffe and O. M. Yaghi, *Science*, 2008, **319**, 939-943.

31. K. Koh, A. G. Wong-Foy and A. J. Matzger, *Angewandte Chemie International Edition*, 2008, **47**, 677-680.

32. K. Koh, A. G. Wong-Foy and A. J. Matzger, *Journal of the American Chemical Society*, 2009, **131**, 4184-4185.

33. K. B. Landenberger and A. J. Matzger, *Crystal Growth & Design*, 2010, **10**, 5341-5347.

34. V. W. Manner, B. C. Tappan, B. L. Scott, D. N. Preston and G. W. Brown, *Crystal Growth & Design*, 2014, **14**, 6154-6160.

35. K. B. Landenberger and A. J. Matzger, *Crystal Growth & Design*, 2012, **12**, 3603-3609.

36. D. Mathieu, *Industrial & Engineering Chemistry Research*, 2017, **56**, 8191-8201.

37. K. B. Landenberger, O. Bolton and A. J. Matzger, *Journal of the American Chemical Society*, 2015, **137**, 5074-5079.
38. M. J. Kamlet and S. J. Jacobs, *The Journal of Chemical Physics*, 1968, **48**, 23-35.
39. Cheetah 7.0 calculations were performed with the Sandia JCZS product library revision 32.
40. Sun, L.; Wei, S.; Zhang, Y.; Zhai, L.; Yang, Q.; Wei, Q.; Xie, G.; Wang, B.; Chen, S. ACS Applied Energy Materials 2018, **1**, 700–706.

Chapter 5

Conclusion and Future Directions

5.1 Summary

The history of energetic materials dates back to ~220 B.C. in ancient China with the discovery of black powder, a physical mixture consisting of charcoal, sulfur and potassium nitrate.[1, 2] Since then, many energetic materials (propellants, pyrotechnics, and explosives) have been developed military and commercial purposes.[3, 4] One conventional method used to develop new energetic materials is covalent synthesis of brand-new energetic molecules. Traditionally, this synthesis involved the installation of multiple nitro groups onto a carbon rich back bone. [5] Energetic molecules that are carbon rich require adequate oxygen content for the complete combustion of the carbon to CO_2, hydrogen to H_2O, and metal (if present) to metal oxides. This is rarely the case for organic molecules. Therefore, typical combustion of organic energetic materials yields toxic gases like carbon monoxide (CO) and solid residue (i.e. carbon soot and unburned fuel). [6]

A modern strategy, cocrystallization, has been shown to modulate energetic material properties by leveraging existing materials and through careful selection of coformers.[7-12] In Chapter 2 of this dissertation the cocrystallization the high-nitrogen energetic material, BTATz, was investigated. A class of molecules capable of interrupting strong intermolecular interactions in BTATz was identified and six new single and multi-component crystal structures were discovered. It was also discovered that the 1:1 BTATz:pyrazine cocrystal exhibits energetic performance (detonation velocity and detonation pressure) approaching industry standard TNT. Finally, it was shown that cocrystallization of BTATz with non-energetic coformers yielded cocrystals that are more impact insensitive than the parent energetic, revealing that

cocrystallization could be used as a strategy to improve the impact sensitivity of high-nitrogen energetic materials.[13]

Another traditional method to develop energetic materials is the synthesis of metal-based materials. Some currently used metal-based energetic materials consists of heavy, toxic metals including mercury and lead. There is a strong need to design new metal-based EMs that avoid the use of these heavy toxic metals. This is because the decomposition of materials containing lead and mercury can cause considerable contamination to surrounding areas and adverse health effects to human personnel.[14-16] Coordination polymerization is one modern strategy that could be used to access new high-energy materials with non-toxic metals and energetic ligands. In chapter 2 of this dissertation, the design of energetic coordination polymers with the high-nitrogen energetic material BTATz was highlighted. Two new energetic coordination polymers, 1D ZnBTATz and 2D ZnBTATz, were discovered by the solvothermal synthesis of BTATz and $Zn(NO_3)_2 \cdot 6H_2O$. These new structures feature dinuclear clusters with three $BTATz^{2-}$ ligands coordinated in octahedral geometries around two zinc ions. Both structures are more thermally sensitive than the parent molecule and exhibit more neutral oxygen balances. Further, both structures are more impact insensitive than BTATz indicating that coordination polymerization of energetic ligands can also be used to improve impact sensitivity through careful selection of metal ions.

Another modern strategy to design energetic materials with environmentally benign decomposition products is the synthesis of metal-organic frameworks (MOFs)-oxidant composites. These porous, composite materials have been previously shown to yield high-performing energetics through adsorption of over-oxidized guests into the fuel rich (carbon and hydrogen) frameworks.[17] However, many MOFs are synthesized with carboxylate substituted

ligands. This substituent forms latent CO_2 upon decomposition and does not increase the overall heat release. In chapter 4 of this dissertation, the adsorption of tetranitromethane (TNM) guests into zeolitic imidazolate frameworks (ZIFs) was investigated as a facile strategy to access high-energy composite materials. Two frameworks, ZIF-8 and ZIF-70 were loaded with TNM guests and the energetic properties of the new composites, ZIF-8-TNM and ZIF-70-TNM were examined. Overall, both structures exhibit reasonable sensitivity to impact which influences their classification as secondary explosive materials. Structural features of ZIF-70 including large pore windows permit the uptake of more oxidant guests than ZIF-8. This feature along with the inclusion of nitroimidazole ligands led to a much more neutral oxygen balance of the ZIF-70-TNM composite (-27.2%) which is approaching the industry standard HMX (-21.6%).[1]

5.2 Future Work: Coordination Polymerization with BTATz

As previously discussed, 1D ZnBTATz and 2D ZnBTATz exhibit energetic properties that are improved in comparison to the parent molecule including oxygen balance and sensitivity to stimuli. The next logical direction of further study of these new materials is the theoretical determination of energetic performance, in order to compare the performance of the new materials to existing materials. To achieve this, the synthesis of 1D and 2D ZnBTATz must first be scaled-up to hundred milligram (mg) quantities. Then, samples of about 50-100 millgrams should be pressed into pellets and evaluated using oxygen bomb calorimetry. From these experiments, an average temperature rise (ΔT) can be extracted, and ΔH_f can be determined using the equations 1-3 below. Finally, the thermochemical software Cheetah can be employed to predict the theoretical detonation velocity and detonation pressure of 1D ZnBTATz and 2D ZnBTATz based on ΔH_f, density, molecular formula inputs.

$$\Delta U_{m,comb} = \frac{\Delta T(°C) - C_{cal}\left(\frac{J}{°C}\right)\text{-Resisitive Heating(J)-NiCr burned}\left(\frac{J}{mg}\right)*\text{Mass burned wire(mg)}}{\text{Mass of sample(mg)}*\text{MW}\left(\frac{g}{mol}\right)} \quad \text{(eq.1)}$$

$$\Delta H_{m,comb} = \Delta U_{m,comb} + \Delta n_g RT \quad \text{(eq. 2)}$$

$$\Delta H_f^{\circ}(\text{ZnBTATz}) = \Sigma \Delta H_f^{\circ}(\text{products}) - \Delta H_{m,comb}(\text{ZnBTATz}) \quad \text{(eq.3)}$$

5.3 Future Work: Adsorption of Energetic Guests into MOFs

In chapter 4 of this dissertation, the adsorption of TNM guests into zeolitic imidazolate frameworks was investigated. Some challenges were experienced in the quantification of volatile guests leading to probable underestimation of oxidant loading. This is due to the volatile nature of the oxidant guests that could readily escape from the pores of the ZIFs prior to analysis by TGA. To circumvent this problem, the next direction of further study should focus on the uptake of solid energetic guests into porous frameworks. This could be achieved by melt loading of energetic guests like TNT in to the pores or by solvent-assisted grinding.

In a recent study by Matzger and co-workers, an energetic MOF was synthesized by the coordination of copper ions to highly nitrated biphenyl ligands, to form a 3D structure known as CuNbO-1. It was observed that thermal decomposition of this high-energy structure around ~250 °C resulted in the unfolding of fibrous carbon products that exhibit high copper metal dispersion on the surface. [18]

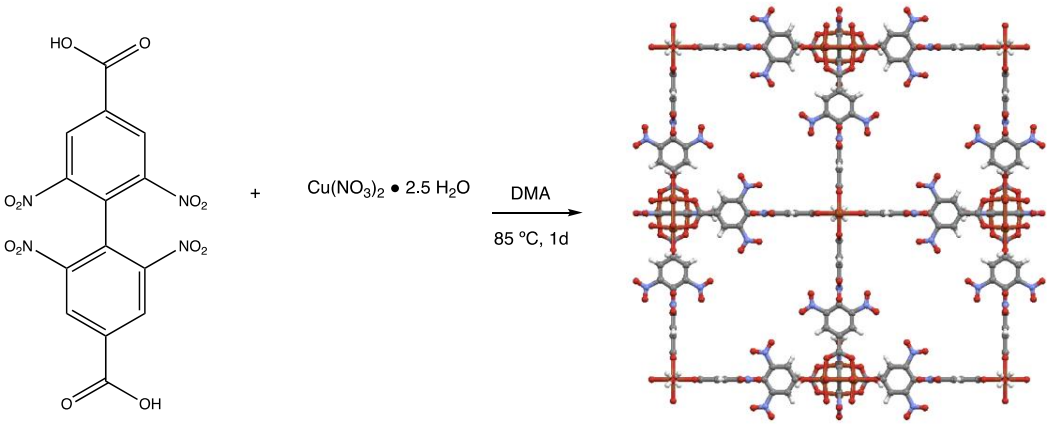

Properties
Cubic crystals
Contains copper paddlewheels
Non-interpenetrated 3-D framework
nbo topology
Under-oxidized, -OB%

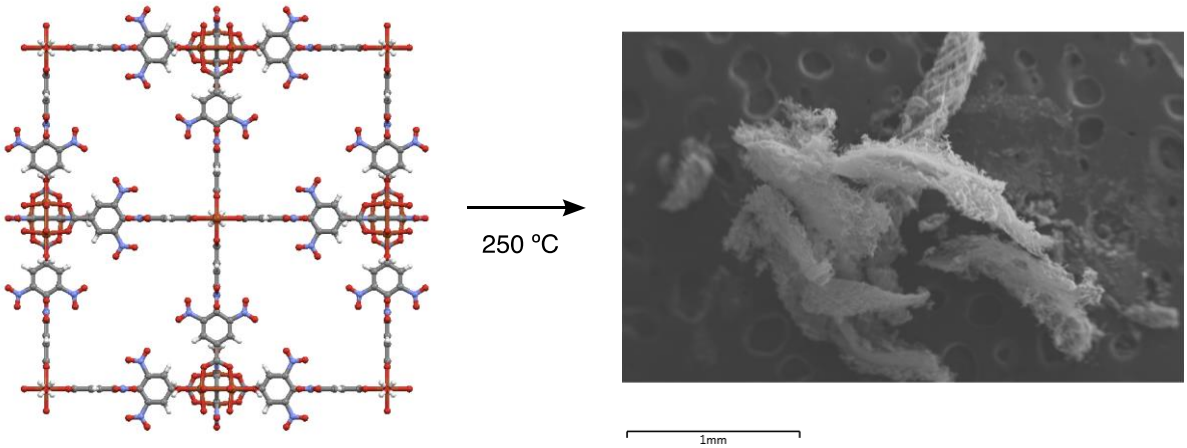

Properties
Long anisotropic carbon structures
Amorphous carbon, no long range order
Carbon thickness: 12Å
Thickness corresponds to stacking of 3 carbon layers
High level of metal dispersion

Figure 5.1 Synthesis conditions of CuNbO-1 crystals and non-interpenetrated crystal structure. Scanning electron microscope image of the thermal decomposition product of CuNbO-1, showing amorphous carbon products.

Given the high dispersity of metal on the surface of the carbon fibers, one potential application of this material is in heterogeneous catalysis. However, 2,2',6,6'-tetranitrobiphenyl-4,4'-dicarboxylic acid (H_2BPDC-(NO_2)$_4$) was utilized as the ligand in CuNbO-1, and the synthesis of this ligand requires very harsh reaction conditions and a seven-step synthesis starting from commercially available 4-iodobenzoic acid. For example, the nitration of starting material 4-iodobenzoic acid requires a mixture of fuming H_2SO_4 and fuming HNO_3. The same harsh conditions are used again in the final step of the synthesis to produce the final product, (H_2BPDC-(NO_2)$_4$). To avoid these types of synthesis conditions, uptake of solid energetic guests into frameworks containing copper metal clusters represents a plausible design strategy. This strategy would leverage existing synthesis conditions and MOF structures to easily produce carbon supports with highly dispersed metal that then can be utilized in heterogeneous catalysis.

5.4 References

1. M. Klapötke Thomas, *Chemistry of High-Energy Materials*, 2015.
2. J. Akhavan, *The chemistry of explosives*, Royal Society of Chemistry, 2004.
3. A. K. Sikder and N. Sikder, *Journal of Hazardous Materials*, 2004, **112**, 1-15.
4. M. Brinsden, A. Boock and D. Baum, *Propellants, Explosives, Pyrotechnics*, 2015, **40**, 453-454.
5. M. A. C. Hiskey, D.E.; Naud, D.L., *Insensitive High-Nitrogen Compounds* LA-UR-01-1493, Los Alamos National Laboratory, 2001.
6. G. Steinhauser and T. M. Klapötke, *Angewandte Chemie International Edition*, 2008, **47**, 3330-3347.
7. C. B. Aakeröy, T. K. Wijethunga and J. Desper, *Chemistry – A European Journal*, 2015, **21**, 11029-11037.
8. J. C. Bennion, A. McBain, S. F. Son and A. J. Matzger, *Crystal Growth & Design*, 2015, **15**, 2545-2549.
9. O. Bolton, L. R. Simke, P. F. Pagoria and A. J. Matzger, *Crystal Growth & Design*, 2012, **12**, 4311-4314.

10. K. B. Landenberger, O. Bolton and A. J. Matzger, *Journal of the American Chemical Society*, 2015, **137**, 5074-5079.
11. K. B. Landenberger and A. J. Matzger, *Crystal Growth & Design*, 2010, **10**, 5341-5347.
12. K. B. Landenberger and A. J. Matzger, *Crystal Growth & Design*, 2012, **12**, 3603-3609.
13. R. V. Kent, R. A. Wiscons, P. Sharon, D. Grinstein, A. A. Frimer and A. J. Matzger, *Crystal Growth & Design*, 2018, **18**, 219-224.
14. M. H. V. Huynh, M. A. Hiskey, T. J. Meyer and M. Wetzler, *Proceedings of the National Academy of Sciences*, 2006, **103**, 5409-5412.
15. T. M. Klapötke and N. Mehta, *Propellants, Explosives, Pyrotechnics*, 2014, **39**, 7-8.
16. M. A. S. Laidlaw, G. Filippelli, H. Mielke, B. Gulson and A. S. Ball, *Environmental Health*, 2017, **16**, 34.
17. K. A. McDonald, J. C. Bennion, A. K. Leone and A. J. Matzger, *Chemical Communications*, 2016, **52**, 10862-10865.
18. K. A. McDonald, N. Ko, K. Noh, J. C. Bennion, J. Kim and A. J. Matzger, *Chemical Communications*, 2017, **53**, 7808-7811.